The influence of hydrogen, deformation geometry, and grain size on the rheological properties of olivine at upper mantle conditions

A THESIS

SUBMITTED TO THE FACULTY OF THE GRADUATE SCHOOL

OF THE UNIVERSITY OF MINNESOTA

BY

Jacob A. Tielke

IN PARTIAL FULFILLMENT OF THE REQUIREMENTS

FOR THE DEGREE OF

DOCTOR OF PHILOSOPHY

David L. Kohlstedt, Adviser

September, 2015

Acknowledgements

I have many people to thank for their assistance and generosity during the past 5 years. First and foremost, I would like to sincerely thank my advisor, David Kohlstedt. The knowledge and guidance he patiently afforded me were central to my ability to complete this project. His unique combination of integrity and humility make him the perfect role model for every graduate student. I am very thankful for the guidance and support of Mark Zimmerman. The many productive discussions I had with Mark greatly contributed to many aspects of this thesis. Mark is an invaluable component of the Rock and Mineral Physics laboratory and is also an excellent teacher and collaborator. I am especially thankful to Christian Teyssier and Justin Revenaugh for providing guidance and perspective throughout many phases of this project. I am grateful for the time, patience, and flexibility of my graduate committee when scheduling and administrating exams.

I am thankful to many active and past researchers in the Rock and Mineral Physics laboratory. Lars Hansen's expertise with laboratory and analytical methods is greatly appreciated. The many conversations I had with Lars were both stimulating and often led to interesting and productive results. Amanda Dillman's assistance in the lab, including her expertise with Paterson vessels, fixing and calibrating Paterson furnaces, and maintaining the one-atmosphere furnaces, is extremely appreciated. Amanda was often the first person I went to when I had a new idea for an experiment or analysis or when I needed someone to double check my calculations. I am grateful for the assistance and lucrative conversations of Chao Qi, Yang Li, Miki Tasaka, Shenghua Mei, Matej Pec, Alejandra Terminel, Dan King, Marshall Sundberg, Lili Xu, and

Cameron Meyers. Furthermore, I had the privilege of working with many talented undergraduate researchers in the Rock and Mineral Physics lab, including Chris Novitsky, Jennifer Gorce, Elizabeth Thompson, Matt Pendleton, Carolyne Bocovich, Aaron Steelquist, Dylan Stover, and Sean Linden.

The assistance and conversations with researchers in the Department of Earth Sciences has also been very helpful. Paul Weiblen's generosity in sharing his wealth of knowledge, wisdom, and historical perspective on many aspects of science and life in general is greatly appreciated. I will strive to achieve Chris Paola's depth of knowledge on fluid dynamics and his effective teaching style. The expertise of Tony Withers, Ellery Fraum, Anette von der Handt, Nick Seaton, Brian Bagley, and Jed Mosenfelder was crucial to the quality of many of the analyses carried out during this project. Many conversations with other graduate students in the Earth Sciences department helped this project, notably those with Will Nachlas and Johnny Zhang. Many insightful conversations with researchers outside of the University of Minnesota were important for molding the direction of the research presented in this document. Conversations with Holger Stunitz, Hans de Bresser, Takehiro Hiraga, Greg Hirth, and Steve Mackwell were especially lucrative.

The assistance of the staff at the Earth Sciences department has been amazing. Doug Johnson and Gregg Gambeski made issues of payroll and travel logistics very straightforward. I am very grateful for the support of Sharon Kressler and Kathy Ohler in department issues. Jennifer Petrie did most of the work scheduling the department seminars for the 2014-2015 academic year, even though I received most of the credit. Jennifer was also very helpful in navigating the university bureaucracy when complications occurred.

I am also grateful for the various funding sources that have supported me during the last five years. These include NASA and NSF awards to David Kohlstedt and Mark Zimmerman, and Fellowships from the Earth Sciences department.

I would also like to thank my Bachelor's and Master's advisers, Brennan Jordan and Michael Terry, for providing a foundation in research in the Earth Sciences.

My largest thanks goes to my family. My wife, Kate, has been extremely supportive

throughout the last 13 years. She is the reason I have been able to get this far in my academic career and deserves credit for many of my achievements. My parents, Jerry and Courtney, have been supportive throughout my life and very much responsible for my interest in and pursuit of science. I am also grateful for my parents-in-law, Mark and Kathy, for their encouragement and support.

Dedication

To my mother and father, for their support and inspiration.

Abstract

Many important geophysical processes, including mantle convection and the associated movement of Earth's tectonic plates, are strongly dependent upon the rheological properties of Earth's upper mantle. Olivine is the most abundant mineral in the upper mantle and therefore largely controls the mechanical behavior of this region of Earth's interior. Many experimental investigations have been carried out to study the rheological properties of olivine single crystals, synthetically produced aggregates, and naturally occurring mantle rocks at asthenospheric temperatures. In contrast, relatively few studies have focused on measuring the rheological properties of olivine deforming at lithospheric temperatures. Furthermore, there are several unanswered questions about the microphysical processes that control deformation of olivine at upper mantle conditions.

One outstanding question in the field of rock and mineral physics is *Do different microphysical processes control the rate of deformation of olivine at asthenospheric compared to lithospheric mantle conditions?* To address this question we carried out direct shear experiments on olivine single crystals at temperatures that span the transition from lithospheric to asthenospheric mantle conditions. The results of these experiments, which are presented in Chapter 2, demonstrate that the dependence of strain rate upon stress transitions from a power-law relationship at high temperatures to an exponential dependence at lower temperatures. This transition in rheological behavior is consistent with deformation that is controlled by the climb of dislocations at high-temperature conditions and deformation that is controlled by the glide of dislocations at low-temperature conditions. Furthermore, the direct shear geometry allows for isolation of the (001)[100] and (100)[001] dislocation slip systems, which cannot be individually activated in triaxial compression. At high-temperature conditions, crystals oriented for shear on the (001)[100] slip system are observed to be weaker than crystals oriented for shear on the (100)[001] slip system. At low-temperature conditions the opposite relationship is observed: crystals oriented for shear on the (100)[001] slip system are weakest.

Another important outstanding question is *Do the mechanisms of hydrolytic weakening in olivine differ at asthenospheric compared to lithospheric mantle conditions?* In Chapter 3 we report the results of experiments carried out on olivine single crystals under hydrous conditions at both asthenospheric and lithospheric temperatures. For crystals deformed at high-temperatures and under hydrous conditions, the dependence of strain rate on stress follows a power-law relationship with a stress exponent (n) of $\sim$2.5, consistent with deformation that is rate limited by diffusion of silicon through the olivine lattice. In contrast, crystals deformed at high-temperatures and under anhydrous conditions yield $n \approx 3.5$, consistent with deformation that is rate limited by diffusion of silicon through the cores of dislocations. At low temperature conditions, the strain rate of both hydrous and anhydrous crystals are equally well described by the same exponential dependence of stress. These observations demonstrate significant hydrolytic weakening occurs at asthenospheric temperatures, but hydrolytic weakening cannot be resolved at lithospheric temperatures for our experimental conditions.

Lastly, we address a question about polycrystalline deformation: *what deformation mechanism is responsible for grain-size sensitive (GSS) power-law creep of olivine aggregates?* In Chapter 4 we compare strain rates measured during deformation experiments on olivine aggregates to strain rates calculated from a micromechanical model of intragranular slip. The micromechanical model uses the measured stress from deformation experiments and grain orientations determined from post-deformation electron backscatter diffraction measurements to approximate the contribution of dislocation creep to the strain rate. Olivine aggregates deform up to a factor of 4.6 times faster than the maximum possible rates determined from the micromechanical model of intragranular slip. The ratio of experimentally determined strain rates to those from the micromechanical model is strongly dependent upon grain size, but is independent of stress and strength of lattice-preferred orientation. These observations indicate that GSS power-law creep occurs in both weakly and strongly textured olivine aggregates at the studied conditions. We consider three explanations for the observed rheological behavior, (1) a combination of diffusion and dislocation creep, (2) the operation of dynamic recrystallization

creep, and (3) the operation of dislocation-accommodated grain-boundary sliding. Our analyses indicate that the microstructural and mechanical behavior of olivine aggregates deforming in the grain-size sensitive power-law regime are most consistent with the operation of dislocation-accommodated grain-boundary sliding at the studied experimental conditions.

Contents

List of Tables

List of Figures

Chapter 1

Introduction

1.1 Background

Many important geophysical processes that operate in Earth's upper mantle, including large-scale convection and the associated movement of tectonic plates, are controlled by the rheological properties of mantle rocks. The rheological properties of mantle rocks are highly dependent upon olivine, as it is the most abundant and generally considered the weakest mineral in Earth's upper mantle. This observation has led to the development of an extensive literature describing high-temperature deformation of olivine single crystals, synthetically produced fine-grained aggregates, and natural rocks. However, there are many outstanding questions that are central to understanding the rheological properties of olivine-rich rocks, including (1) *does the flow behavior of olivine differ at lithospheric compared to asthenopheric temperatures?* (2) *do the mechanisms of hydrolytic weakening differ at lithospheric compared to asthenospheric temperatures?* and (3) *at what conditions does grain-size sensitive power-law creep occur in olivine?* In this thesis, results from laboratory deformation experiments on olivine single crystals and micromechanical models of polycrystalline deformation are reported to address these questions.

1.2 Rheological Regimes and Deformation Mechanisms of Mantle Rocks

Rheological regimes that are both grain-size sensitive (GSS) and grain-size insensitive (GSI) have been identified during high-temperature steady-state deformation of mantle rocks. These regimes include GSS linear creep, GSS power-law creep, and GSI power-law creep. Each regime is defined by flow laws of the form

$$\dot{\varepsilon} = A\frac{\sigma^n}{d^p} f_{\mathrm{O}_2}^{\ m} f_{\mathrm{H_2O}}^{r} \exp\left(\frac{-Q}{\mathrm{R}T}\right), \tag{1.1}$$

where $\dot{\varepsilon}$ is strain rate, A is a material specific parameter, σ is differential stress, n is the stress exponent, d is grain size, p is the grain size exponent, f_{O_2} is oxygen fugacity, m is the oxygen fugacity exponent, $f_{\mathrm{H_2O}}$ is water fugacity, r is the water fugacity exponent, Q is activation enthalpy, R is the gas constant, and T is temperature.

The rheological regimes are usually interpreted to reflect the operation of individual deformation mechanisms: GSS linear creep is associated with diffusion creep, GSS power-law creep is associated with dislocation-accommodated grain-boundary sliding, and GSI power-law creep is associated dislocation creep (*Hirth and Kohlstedt*, 2003). If the rheological regimes represent deformation mechanisms that operate independently of one another, the total strain rate ($\dot{\varepsilon}_{\mathrm{total}}$) of a deforming rock, can be expressed as

$$\dot{\varepsilon}_{\mathrm{total}} = \dot{\varepsilon}_{\mathrm{diff}} + \dot{\varepsilon}_{\mathrm{disGBS}} + \dot{\varepsilon}_{\mathrm{disl}}, \tag{1.2}$$

where the subscripts diff, disGBS, and disl refer to the strain rates from diffusion creep, dislocation-accommodated grain-boundary sliding, and dislocation creep, respectively. The conditions at which each deformation mechanism is dominant (i.e. rate controlling) can be clearly observed on deformation mechanism maps, as exemplified in Figure 1.1.

The flow laws that were used to construct the boundaries between the different fields in Figure 1.1 are mostly derived from laboratory deformation experiments carried out on olivine

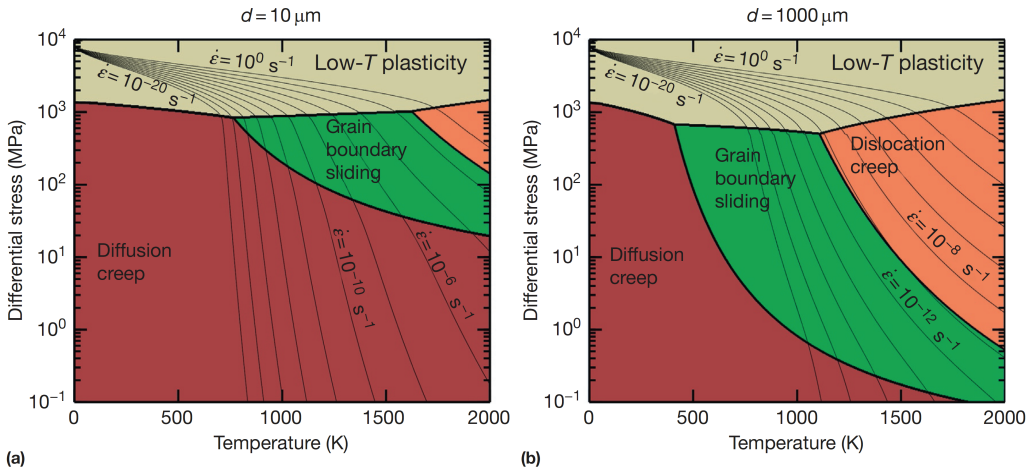

Figure 1.1: Deformation mechanism maps, from *Kohlstedt and Hansen* (2015), demonstrating the conditions of temperature, stress, and strain rate that deformation mechanism for anhydrous olivine aggregates operate at (a) a typical laboratory grain size of 10 μm and (b) a typical upper mantle grain size of 1000 μm. In these maps the grain boundary sliding field refers to disGBS.

aggregates. The use of olivine aggregates has many advantages over using natural rocks and single crystals. The grain size of olivine aggregates can be precisely controlled, allowing for determination of flow law parameters for GSS deformation mechanisms. However, a consequence of using olivine aggregates is that deformation often occurs near the transition between mechanisms, such as the transition between diffusion creep and dislocation-accommodated grain-boundary sliding. Therefore, at certain conditions of stress and grain size, the strain rate of olivine aggregates is the result of the operation of multiple deformation mechanisms (e.g., *Hirth and Kohlstedt*, 2003, Fig. 2). This situation increases the difficulty of precisely determining flow law parameters, specifically n, for individual mechanisms.

1.3 Importance of Single Crystal Experiments

Single crystal deformation experiments provide the most direct means of determining the flow law parameters for olivine deforming by dislocation creep. During deformation of a single crystal, the strain rate from the motion of dislocations can be precisely measured, without the

added complications arising from the operation of GSS deformation mechanisms. Importantly, the value of n for dislocation creep can be precisely determined from single crystal deformation experiments.

The value of n for dislocation creep has very important implications for understanding the strength of the upper mantle. Models of dislocation creep at asthenospheric mantle conditions predict either $n \approx 2.4$ when deformation is rate limited by silicon diffusion through the lattice or $n \approx 3.8$ when deformation is rate limited by diffusion of silicon along the cores of dislocations (*Hirth and Kohlstedt*, 2015). Extrapolation of data from laboratory deformation experiments to values of stress typical of Earth's upper mantle using $n \approx 2.4$ or $n \approx 3.8$ yield significantly different predictions of strain rate, as presented in Figure 1.2. This observation highlights the need for precise determination of the value of n for olivine during dislocation creep, which can best be carried out by analyzing results from single crystal deformation experiments.

Another important aspect of deformation that can be most directly measured from single crystal deformation experiments is the relative strength of the individual dislocation slip systems. However, during triaxial compression of olivine single crystals, only two of the four dominate slip systems can be isolated. In contrast, the direct shear geometry utilized in the experiments reported in Chapter 2 allows for isolation of the two remaining slip systems. Precise knowledge of the strength of the individual slip systems has important implications for understanding the development and rheological impact of lattice-preferred orientation (LPO) in mantle rocks.

1.4 Applications to LPO Development in Mantle Rocks

Micromechanical models of polycrystalline deformation have become increasingly complex over the past 15 years (e.g., *Tommasi et al.*, 2000; *Kaminski and Ribe*, 2001; *Castelnau et al.*, 2008, 2009). One of the primary goals of these models is to describe the development of LPO in deforming mantle rocks. The input for most micromechanical models of LPO development is a ranking of the relative strength of individual slip systems. At conditions of high-temperature

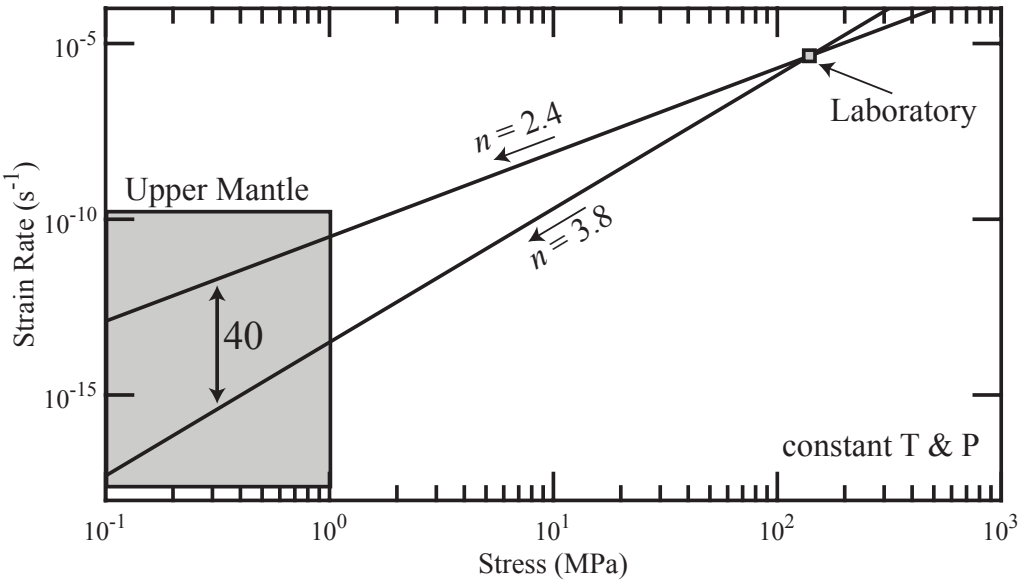

Figure 1.2: Plot of strain rate as a function of stress illustrating the importance of the value of n when extrapolating from laboratory to upper mantle conditions. A typical laboratory stress of 130 MPa and strain rate of 5 x 10^{-5} s^{-1} is indicated by the small square in the top right. The two black lines represent extrapolation of these laboratory conditions to lower stress conditions more typical of the upper mantle using an n value of either 2.4 (top) or 3.8 (bottom). Consideration of the strain rate predicted by these two values of n results in a difference of $\sim$40 in strain rate for a stress between 0.1 and 1.0 MPa typical of upper mantle conditions.

($> 1150°$C), these models are able to reproduce the general geometry of LPO observed in experimentally deformed olivine aggregates, as presented in Figure 1.3.

More recent work has implemented micromechanical models of LPO evolution into numerical simulations of flow in the asthenospheric mantle (e.g., *Becker et al.*, 2006; *Castelnau et al.*, 2009; *Becker and Kawakatsu*, 2011). Many of these models predict the development of an LPO with olivine [100] axis aligning near the direction of mantle flow as presented in Figure 1.4. This relationship between olivine LPO and the direction of flow is consistent with observations of LPO in olivine aggregates deformed at asthenospheric mantle conditions (e.g., *Bystricky et al.*, 2000; *Zhang et al.*, 2000; *Hansen et al.*, 2012, 2014). Additional knowledge of the relative strength of individual slip systems, which can be most directly gained from analyses of single crystal deformation experiments carried out in direct shear, would improve the

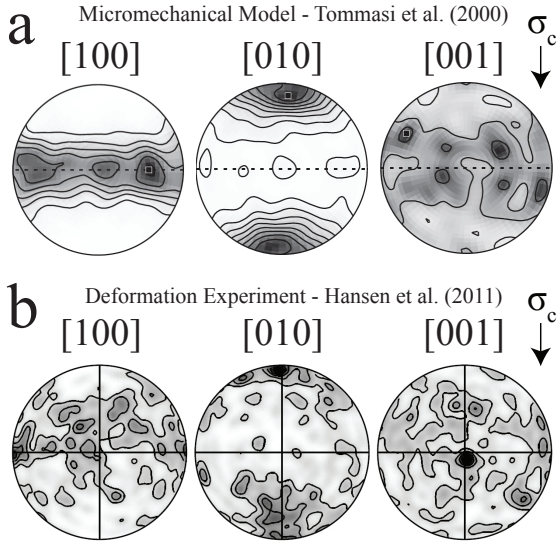

Figure 1.3: Comparison of LPO predicted for (a) olivine from a micromechanical model (*Tommasi et al.*, 2000) to those from (b) a deformation experiment carried out on olivine aggregates (*Hansen et al.*, 2011). The orientation of maximum compression stress (σ_c)is to the north in both sets of pole figures.

accuracy of these models.

Micromechanical models have also been applied to exploring the connection between LPO and mechanical properties of olivine-rich rocks at lithospheric mantle conditions (e.g., *Tommasi et al.*, 2009; *Knoll et al.*, 2009). These models rely on the relative strength of slip systems interpreted from data for experiments carried out at asthenospheric mantle conditions. However, it is becoming increasingly clear that the flow behavior of olivine single crystals and aggregates is significantly different at lithospheric compared to asthenospheric temperatures (*Mei et al.*, 2010; *Druiventak et al.*, 2011; *Demouchy et al.*, 2013). As micromechanical models and numerical simulations of mantle flow become more complex, and especially when lithospheric mantle conditions are considered, precise knowledge of the strength of the individual slip systems of olivine over large ranges of temperature and stress is paramount.

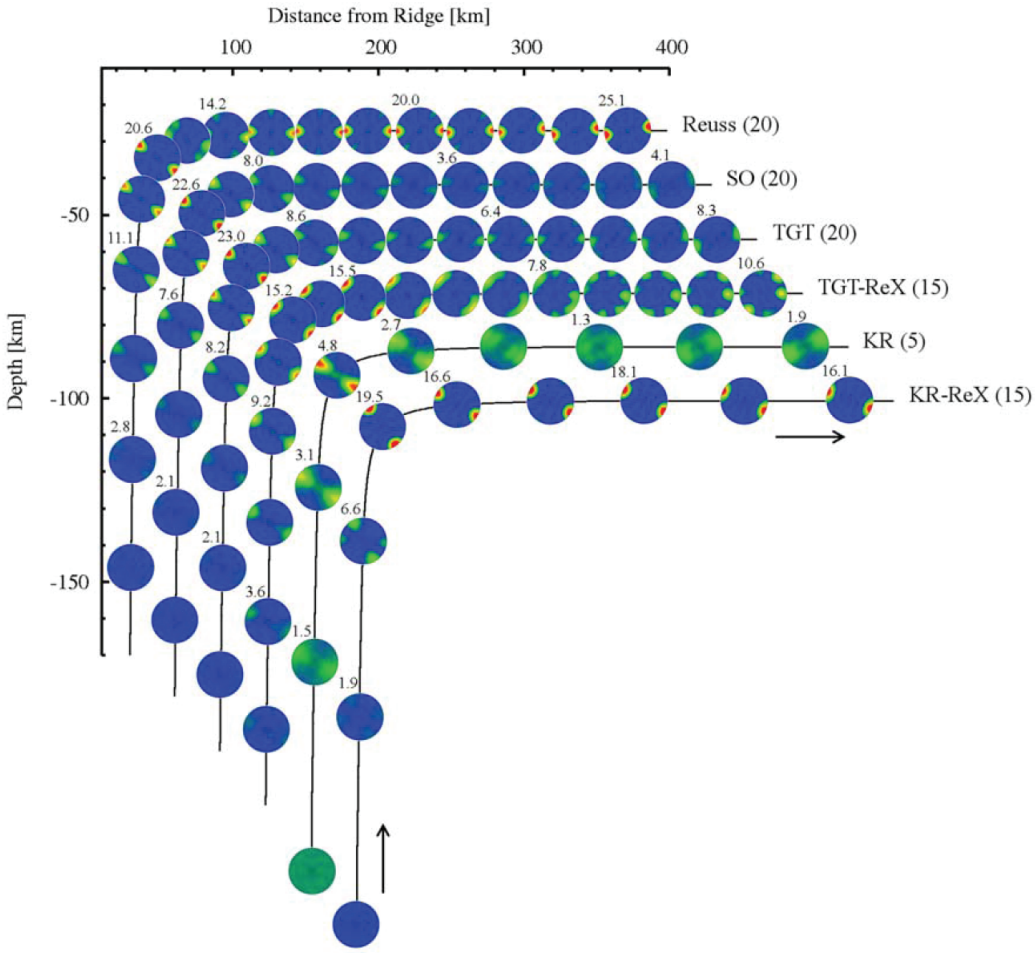

Figure 1.4: Evolution of LPO development beneath an oceanic spreading center predicted from six micromechanicl models from *Castelnau et al.* (2009). The pole figures represented olivine [100] axes. A uniform fabric is used for the begining of the simulations starting at a depth of 150 km. The sense of shear transitions from vertical beneath the spreading center to horizontal away from the spreading center.

1.5 Questions of Hydrolytic Weakening in Olivine

Single crystal deformation experiments are vital to understanding the microphysical processes responsible for hydrolytic weakening in olivine. Numerous studies from experimentally deformed natural rocks (e.g., *Carter and Ave'Lallemant*, 1970; *Chopra and Paterson*, 1984) and synthetically produced aggregates (e.g., *Karato et al.*, 1986; *Mei and Kohlstedt*, 2000a,b) have documented hydrolytic weakening. Relatively few studies have focused on hydrolytic weakening in olivine single crystal experiments (e.g., *Mackwell et al.*, 1985; *Girard et al.*, 2013). However, interpretations of results from diffusion experiments carried out on forsterite single crystals suggest only a small degree of weakening occurs under hydrous conditions (*Fei et al.*, 2013). Furthermore, the authors of this diffusion study suggest that experiments from olivine aggregates under hydrous conditions are anomalously weak due to the presence of water along grain boundaries. In Chapter 3 we present results from experiments carried out under hydrous conditions and over a large range of conditions of stress and temperature to quantify hydrolytic weakening of olivine in the climb-controlled and glide-controlled dislocation creep regimes.

1.6 Investigations of Grain-Size Sensitive Power-Law Creep

An important aspect of experimental deformation is relating flow laws, which describe rheological regimes, to deformation mechanisms that describe the atomistic processes that give rise to flow. The correlation of the GSS linear creep regime to diffusion creep and the GSI power-law creep regime to dislocation creep is well established. However, the deformation mechanism operating during GSS power-law creep has been attributed to either dislocation-accommodated grain-boundary sliding, dynamic recrystallization-controlled dislocation creep, or a combination of diffusion creep and dislocation creep.

In Chapter 4 we present results from a micromechanical model that is used to determine the fraction of strain rate that can be accommodated by the motion of intragranular dislocations (i.e. dislocation creep). This model uses measurements of stress, strain rate, and grain orientations from polycrystalline deformation experiments combined with flow laws for single crystals to

determine the contribution of dislocation creep to the strain rate in several experiments. These data are used to evaluate the different mechanisms proposed for GSS power-law creep.

Chapter 2

Direct shear of olivine single crystals

Knowledge of the strength of individual dislocation slip systems in olivine is crucial to understanding the flow behavior and the development of lattice-preferred orientation in olivine-rich rocks. The most direct measurements of the strengths of individual slip systems are from triaxial compression experiments on olivine single crystals. However, such experiments only allow for determination of flow laws for two of the four dominate slip systems in olivine. In order to measure the strengths of the (001)[100] and (100)[001] slip systems independently, we performed deformation experiments on single crystals of San Carlos olivine in a direct shear geometry. Experiments were carried out at temperatures of 1000° to 1300°C, a confining pressure of 300 MPa, shear stresses of 60 to 334 MPa, and resultant shear strain rates of 7.4 x 10^{-6} to 6.7 x 10^{-4} s^{-1}. At high-temperature ($\geq$1200°C) and low-stress ($\leq$200 MPa) conditions, the strain rate of crystals oriented for direct shear on either the (001)[100] or the (100)[001] slip system follows a power law relationship with stress, whereas at lower temperatures and higher stresses, strain rate depends exponentially on stress. The flow laws derived from the mechanical data in this study are consistent with a transition from the operation of a climb-controlled dislocation mechanism during power-law creep to the operation of a glide-controlled dislocation mechanism during exponential creep. In the climb-controlled regime, crystals oriented for shear on the (001)[100] slip system are weaker than crystals orientated for shear on the (100)[001] slip system. In

contrast, in the glide-controlled regime the opposite is observed. Extrapolation of flow laws determined for crystals sheared in orientations favorable for slip on these two slip systems to upper mantle conditions reveals that the (001)[100] slip system is weaker at temperatures and stresses that are typical of the asthenospheric mantle, whereas the (100)[001] slip system is weaker at conditions typical of the lithospheric mantle. These observations demonstrate that the relative strength of the dislocation slip systems in olivine, and thus the development of lattice-preferred orientation in olivine-rich rocks, is strongly dependent upon temperature and stress.

2.1 Introduction

The rheological and microstructural properties of olivine-rich rocks reflect the strength of dislocation slip systems. One means of measuring the strength of dislocation slip systems is by carrying out deformation experiments on single crystals that are oriented to promote the motion of dislocations on specific slip systems. Many experiments have been performed on olivine single crystals in triaxial compression (e.g., *Young*, 1969; *Kohlstedt and Goetze*, 1974; *Durham and Goetze*, 1977; *Darot and Gueguen*, 1981; *Kohlstedt and Hornack*, 1981; *Poumellec and Jaoul*, 1984; *Ricoult and Kohlstedt*, 1985b; *Mackwell et al.*, 1985; *Bai et al.*, 1991; *Raterron et al.*, 2007, 2009; *Demouchy et al.*, 2009, 2013; *Girard et al.*, 2013). These experiments are usually carried out in three orientations, referred to as $[110]_c$, $[101]_c$, and $[011]_c$, where a compressive stress (σ_1) is applied at 45° to specific crystallographic axes in olivine. These orientations allow for activation of the four dominate dislocation slip systems in olivine, which operate on the (100), (010), and (001) planes and have either [100] or [001] Burgers vectors. For the $[110]_c$ orientation, σ_1 is orientated at 45° to both the [100] and [010] axes, activating the (010)[100] slip system. In a similar manner, the $[011]_c$ orientation has σ_1 at 45° to the [010] and [001] axes, activating the (010)[001] slip system. However, the $[101]_c$ orientation has σ_1 at 45° to the [100] and [001] axes, which simultaneously activates both the (001)[100] and (100)[001] slip systems.

To activate the (001)[100] and (100)[001] slip systems independently, we performed deformation experiments on single crystals of San Carlos olivine in a direct shear geometry, as illustrated in Figure 2.1. The direct shear geometry allows for isolation of one of these slip systems at a time, providing information essential to understanding the development of lattice-preferred orientation (LPO) in upper mantle rocks.

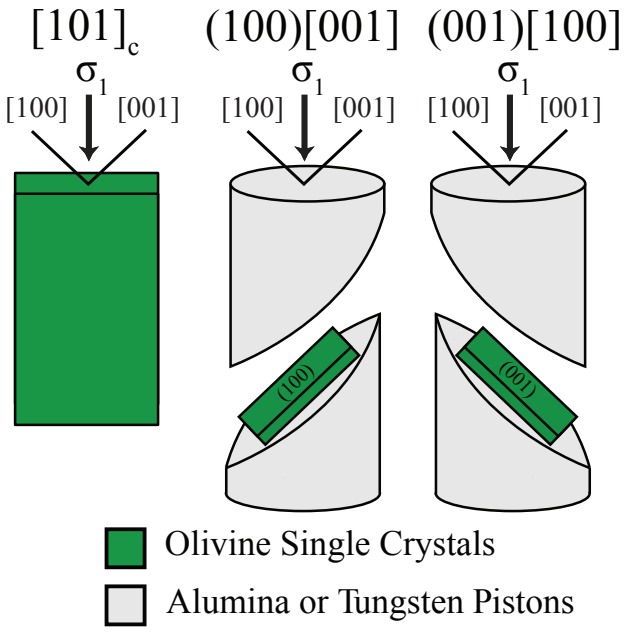

Figure 2.1: Illustrations of crystals oriented for deformation in triaxial compression in the $[101]_c$ orientation (left) and for crystals oriented for direct shear (middle and right) on the (100)[001] and (001)[100] slip systems, respectively. During triaxial compression of crystals in the $[101]_c$ orientation, dislocations on the (100)[001] and (001)[100] operate simultaneously, whereas the direct shear geometry allows for deformation on only one of the slip systems during deformation.

2.1.1 Applications to LPO

Many physical properties of mantle rocks are strongly influenced by the strength of LPO of their constitutive minerals. The presence of LPO affects the strength of anisotropy in propagation of seismic waves (*Ismail and Mainprice*, 1998; *Becker et al.*, 2006), the degree of attenuation

of seismic waves (*Farla et al.*, 2012), and the magnitude of electrical conductivity (*Pommier et al.*, 2015). Field based measurements of these properties, combined with data from laboratory experiments and numerical simulations of LPO development, form a framework for interpreting the structure and flow behavior of Earth's upper mantle.

Numerical simulations that implement the relative activity of dislocation slip systems inferred from deformation experiments carried out on olivine single crystals successfully reproduce the nature of the LPO observed at asthenospheric mantle conditions conditions (*Tommasi et al.*, 2000). The results from these numerical simulations predict the development of an LPO with crystallographic axes aligned in similar orientations with respect to an externally applied stress as those observed in high-temperature deformation experiments on olivine aggregates (e.g., *Zhang and Karato*, 1995; *Bystricky et al.*, 2000; *Hansen et al.*, 2011, 2012, 2014) and observed in many exposed mantle rocks (e.g., *Ismail and Mainprice*, 1998; *Warren and Hirth*, 2006; *Précigout and Hirth*, 2014).

2.1.2 The Power-Law Creep Regime

At conditions of high temperature and low stress, the strain rate of olivine crystals follows a power-law relationship with stress and an Arrhenius relationship with temperature. The strain rate of crystals deforming in a power-law regime, $\dot{\varepsilon}_{\mathrm{power}}$, is expressed as

$$\dot{\varepsilon}_{\mathrm{power}} = A_{\mathrm{p}} \sigma^{n} \exp\left(\frac{-Q_{\mathrm{p}}}{\mathrm{R}T}\right), \tag{2.1}$$

where A_{p} is a material-specific parameter, σ is stress, n is the stress exponent, Q_{p} is the activation energy, R is the gas constant, and T is the temperature in K (e.g., *Durham and Goetze*, 1977; *Darot and Gueguen*, 1981; *Bai et al.*, 1991). Materials that deform in this manner are consistent with strain via glide of dislocations, with strain rate limited by the mean velocity at which dislocations climb to overcome obstacles such as other dislocations in the crystal lattice (e.g., *Poirier*, 1985, p. 103-107). The rate of climb of dislocations is controlled by diffusion of

the slowest diffusing ionic species along its fastest diffusive pathway, which for the case of anhydrous olivine at high temperatures is silicon diffusing through the cores of dislocations (*Hirth and Kohlstedt*, 2015).

2.1.3 The Exponential Creep Regime

Deformation experiments carried out at low temperatures and high stresses on olivine single crystals (*Phakey et al.*, 1972; *Evans and Goetze*, 1979; *Demouchy et al.*, 2009, 2013) and olivine aggregates (e.g., *Raterron et al.*, 2004; *Mei et al.*, 2010; *Druiventak et al.*, 2011) yield mechanical behavior markedly different from those performed at high-temperature and low-stress conditions. At low temperatures and high stresses, the strain rate of olivine single crystals follows an exponential dependence on stress. The strain rate of crystals deforming in an exponential regime, $\dot{\varepsilon}_{\rm exp}$, is expressed as

$$\dot{\varepsilon}_{\rm exp} = A_{\rm e}\sigma^{1.4}\exp\left[\left(\frac{-Q_{\rm e}}{\mathrm{R}T}\right)\left(1-\left(\frac{\sigma}{\sigma_{\rm e}}\right)^{p}\right)^{q}\right], \tag{2.2}$$

where $A_{\rm e}$ is a material dependent parameter, $Q_{\rm e}$ is the activation energy, $\sigma_{\rm e}$ is the stress needed to move dislocations in the absence of thermal energy, and p and q are parameters describing the shape and spacing of the impediments to dislocation motion (*Kocks*, 1976). Values of p range from 0.5 to 1 and values of q range from 1 to 2. Materials that deform in this manner are consistent with deformation that is rate limited by the ability of gliding dislocations to move through obstacles such as other dislocations or to overcome lattice resistance (*Frost and Ashby*, 1982, p. 6-9).

2.1.4 Inferring Slip System Activity

In this paper, we are primarily concerned with determining flow laws for the (001)[100] and (100)[001] slip systems in both the power law and exponential creep regimes. Previous researchers have used microstructural analyses and measurements of shape change to evaluate the activity of the slip systems that operate during deformation of crystals in the $[101]_{\rm c}$ orientation.

The most direct evidence of the relative activity of the (001)[100] and (100)[001] slip systems is from strain analyses carried out on deformed crystals (*Durham and Goetze*, 1977). Measurements of shape change and rotation of crystallographic planes resulting from compressive creep experiments on crystals in the $[101]_c$ orientation at 1600°C are consistent with most of the deformation occurring by glide of dislocations on the (001)[100] slip system. This conclusion is supported by microstructural observations of crystals that were deformed at high temperature, which reveal that dislocations with Burgers vectors parallel to [100] are more common than those with Burgers vectors parallel to [001] (*Durham et al.*, 1977).

At lower temperature and higher stress conditions, microstructural evidence suggests the activity of the (100)[001] slip system increases relative to the activity of the (001)[100] slip system. Transmission electron microscopy (TEM) analyses of a crystal deformed in the $[101]_c$ orientation at 1150°C demonstrates dislocations operating with [001] Burgers vectors become at least equally as prevalent as dislocations with [100] Burgers vectors (*Durham et al.*, 1977). Measurements of the preferred orientation of low-angle boundaries and shape change in a crystal deformed in the $[101]_c$ orientation at 1000°C demonstrate the (100)[001] slip system is dominant at those conditions (*Tielke et al.*, in prep). Furthermore, TEM analyses of polycrystaline olivine deformed at low-temperatures reveal dislocations with [001] Burgers vectors are either more common (*Phakey et al.*, 1972) or equally common (*Demouchy et al.*, 2014) as dislocations with [100] Burgers vectors at lower temperatures. These observations suggest that the relative strengths of the (001)[100] and (100)[001] slip systems are different at lithospheric conditions than at asthenospheric conditions.

However, inferring the relative activities of the two slip systems using microstructural observations requires important assumptions about the nature of deformation. For example, electron backscatter diffraction (EBSD) measurements of low-angle boundary orientations are only valid if deformation is dominated by the glide of edge dislocations, with a minimal amount of climb. In addition, TEM analyses used to image dislocations and determine Burgers vectors are carried out on very small volumes of samples, such that one must assume that the observed dislocations are representative of the entire sample. Even more critical is the assumption that the observed

dislocations in TEM analyses are those that are primarily responsible for the deformation rather than sessile dislocations.

The limitations of microstructural observations and interpretation of triaxial compression experiments emphasize the need for data from direct shear experiments to determine flow laws for the (001)[100] and (100)[001] slip systems. Orienting crystals with (001) parallel to the shear plane and [100] parallel to the shear direction promotes slip on the (001)[100] system, while restricting motion on the (100)[001] system. Similarly, orienting crystals with (100) parallel to the shear plane and [001] parallel to the shear direction promotes slip on the (100)[001] system, while restricting motion on the (001)[100] system. In this paper, we present results from direct shear experiments on olivine single crystals, with the goal of deriving flow laws that describe the mechanical behavior of the (001)[100] and (100)[001] slip systems over a range of temperatures that include both asthenospheric and lithospheric conditions.

2.2 Methods

2.2.1 Sample Preparation

The starting materials for the experiments performed in this study were single crystals of San Carlos olivine. Crystallographic orientations were acquired from more than 10 EBSD point measurements spanning a polished carbon-coated surface of the crystals. Once the starting orientations were known, the crystals were placed on a goniometer with 3 independent rotational axes and mounted for cutting with a diamond-blade saw. Slices 1-mm thick were produced with surfaces parallel to the (001) or (100) crystallographic planes. Multiple rectangular parallelepipeds with an area of 4.1 x 3.9 mm^2 were produced from each slice. The long axis of each rectangular parallelepiped was parallel to [100] for slices cut along (001) or long axes parallel to [001] for slices cut along (100). The crystals were then placed between shear pistons that consisted of cylinders cut at 45° to the compression direction, as illustrated in Figure 2.1. Shear pistons made of thoriated tungsten were used for experiments carried out at 1200° to 1300°C and alumina pistons were used for experiments carried out at 1000° to 1200°C. The crystals and

shear pistons were placed inside a nickel capsule and stored in a vacuum oven at $>100°$C for a minimum of 12 hours before each experiment.

2.2.2 Deformation Experiments

The nickel capsule containing the crystal and shear pistons was positioned between alumina and zirconia pistons, surrounded by an iron jacket, and inserted into a gas-medium deformation apparatus (*Paterson*, 1990). Deformation experiments were carried out with a thermocouple placed adjacent to the sample in the hot zone of the furnace to control temperature. The temperature was maintained to within $\pm$ 2°C relative to a calibration profile of the furnace. At the beginning of each experiment, the confining pressure and temperature were slowly raised over the duration of approximately 1 hour to the desired conditions. An initial anneal of greater than 3 hours at 1200° or 1300°C and a confining pressure of 300 MPa was performed to aid in adhering the interface between the crystal and the shear pistons. Experiments were carried out in a series of constant load steps as illustrated in Figure 2.2, and the resultant change in position was used to determine the strain rate for each step. The mechanical data were corrected for the small loads borne by the nickel capsules and iron jackets using the flow laws of *Frost and Ashby* (1982, p. 21).

2.2.3 Microstructural Analyses

Post-deformation microstructural analyses included observations using reflected light microscopy and measurements from EBSD analyses. After each experiment the deformation assembly was cut in half in the plane that includes the orientation of maximum compression stress and the shear direction as presented in Figure 2.3. The sample was then polished using diamond lapping film with particle sizes of 30 to 0.5 μm and finished by polishing for one hour with colloidal silica with a particle sizes of 0.04 μm. EBSD analyses were used to measure crystallographic orientations and characterize the development of low-angle boundaries. EBSD maps were made over entire cross sections of the crystals by stitching together multiple maps using the HKL Channel 5 software. The step size used for the maps was 20 μm and the data were corrected for

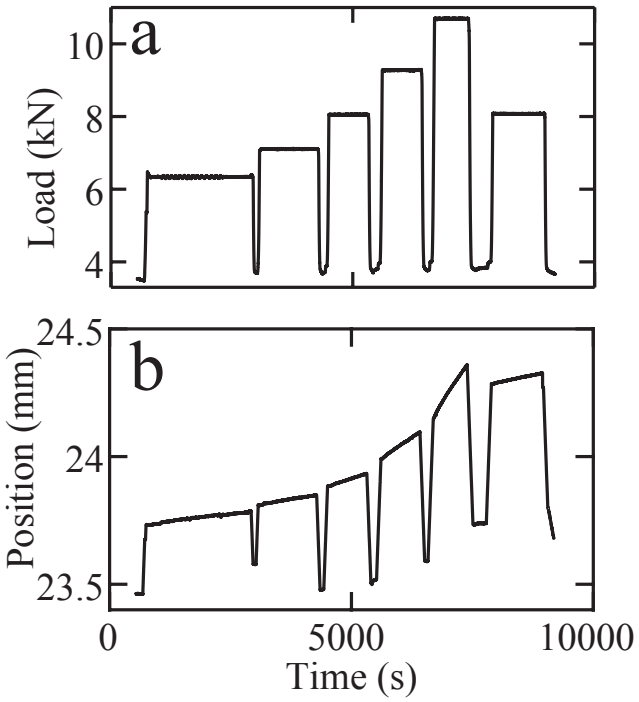

Figure 2.2: Mechanical data from experiment PI-1705. (a) Load as a function of time and (b) position as a function of time. The actuator was moved away from the sample between load steps to check for changes in the zero load. At the end of the experiment, an earlier load step was repeated to examine if strain hardening occurred. The zero load remained constant, and no strain hardening was observed.

systematic misindexing. Additional analyses, including determination of values of the Schmid factor, were carried out using the MTEX toolbox (*Bachmann et al.*, 2010) for MATLAB®.

2.3 Results

2.3.1 Mechanical Results and Flow Law Parameters

Experiments were conducted at 1000° to 1300°C, shear stresses between 60 and 334 MPa, and resultant shear strain rates between 7.4 x 10^{-6} and 6.7 x 10^{-4} s^{-1}, as presented in Table 2.1. The mechanical data for crystals deformed in both orientations demonstrate that the dependence of strain rate on stress is smaller at high-temperature and low-stress conditions than at low-temperature and high-stress conditions. At high temperatures ($\geq$1200°C) and low stresses ($\leq$200 MPa), strain rate is a power-law function of stress, whereas at lower temperatures and higher stresses, strain rate is an exponential function of stress.

Table 2.1: Experimental conditions and creep data

Exp #	T (°C)	b	Pistons	τ (MPa)	$\dot{\gamma}$ (s^{-1})	σ (MPa)	$\dot{\varepsilon}$ (s^{-1})
1705	1200	[100]	W-Th	101	2.7E-05	201	1.5E-05
				130	6.8E-05	260	3.9E-05
				168	1.4E-04	336	8.3E-05
				216	3.2E-04	432	1.9E-04
				136	4.3E-05	272	2.5E-05
1709	1200	[001]	W-Th	85	9.7E-05	170	5.6E-05
				115	2.0E-04	231	1.1E-04
				139	5.6E-04	279	3.3E-04
				190	2.1E-03	381	1.2E-03
				119	3.2E-04	238	1.8E-04
1713	1100	[001]	Al	172	1.9E-05	344	1.1E-05

Continued on next page

Table 2.1 – *Continued from previous page*

Exp #	T (°C)	b	Pistons	τ (MPa)	$\dot{\gamma}$ (s^{-1})	σ (MPa)	$\dot{\varepsilon}$ (s^{-1})
				182	4.2E-05	365	2.4E-05
				195	4.6E-05	390	2.6E-05
1721	1300	[100]	W-Th	60	6.6E-05	121	3.8E-05
				72	8.9E-05	145	5.2E-05
				94	2.4E-04	188	1.4E-04
				113	6.7E-04	227	3.9E-04
				64	5.7E-05	128	3.3E-05
				119	5.1E-04	238	3.0E-04
1725 a	1200	[100]	Al	93	2.3E-05	187	1.3E-05
				117	4.6E-05	234	2.7E-05
				140	8.7E-05	281	5.0E-05
				95	2.7E-05	190	1.5E-05
1725 b	1100	[100]	Al	225	2.8E-05	450	1.6E-05
				240	3.4E-05	480	2.0E-05
				259	4.8E-05	519	2.8E-05
				279	7.5E-05	557	4.3E-05
				243	3.8E-05	485	2.2E-05
1725 c	1000	[100]	Al	316	1.0E-05	631	6.0E-06
				334	1.5E-05	668	8.9E-06
1733a	1300	[001]	W-Th	93	1.8E-04	186	1.0E-04
				119	3.2E-04	239	1.9E-04
				156	5.9E-04	311	3.4E-04
				82	6.2E-05	164	3.6E-05
1733b	1200	[001]	W-Th	85	1.2E-05	169	6.7E-06
				110	1.9E-05	219	1.1E-05

Continued on next page

Table 2.1 – *Continued from previous page*

Exp #	T (°C)	b	Pistons	τ (MPa)	$\dot{\gamma}$ (s^{-1})	σ (MPa)	$\dot{\varepsilon}$ (s^{-1})
				129	2.6E-05	258	1.5E-05
				149	4.6E-05	297	2.7E-05
				168	8.4E-05	336	4.8E-05
				188	1.5E-04	375	8.8E-05
				118	3.1E-05	236	1.8E-05
1736a	1200	[001]	Al	149	8.9E-05	298	5.2E-05
				182	1.8E-04	363	1.0E-04
				213	6.2E-04	426	3.6E-04
1736b	1100	[001]	Al	149	7.4E-06	298	4.3E-06
				178	3.4E-05	356	2.0E-05

The values of the parameters A_{p} and Q_{p} in Equation 2.1 and A_{e}, Q_{e}, and σ_{e} in Equation 2.2 for both orientations were determined by performing least-squares fits of the data in Table 2.1. To facilitate comparison to data obtained from experiments carried out in triaxial compression, the data were converted to equivalent values of stress and strain rate by

$$\sigma = 2\tau \tag{2.3}$$

and

$$\dot{\varepsilon} = \frac{\sqrt{3}}{3}\dot{\gamma}, \tag{2.4}$$

where σ is the equivalent stress, τ is the shear stress, $\dot{\varepsilon}$ is the equivalent strain rate, and $\dot{\gamma}$ is the shear strain rate.

The parameters A_p and Q_p were determined by fitting the data collected at 1200° and 1300°C for crystals oriented for shear on the (001)[100] slip system using Equation 2.1. A value of n of 3.5 was used during the fitting procedure to minimize the number of fitting parameters. This value of n is well established for olivine deforming by dislocation creep (***Bai et al.***,

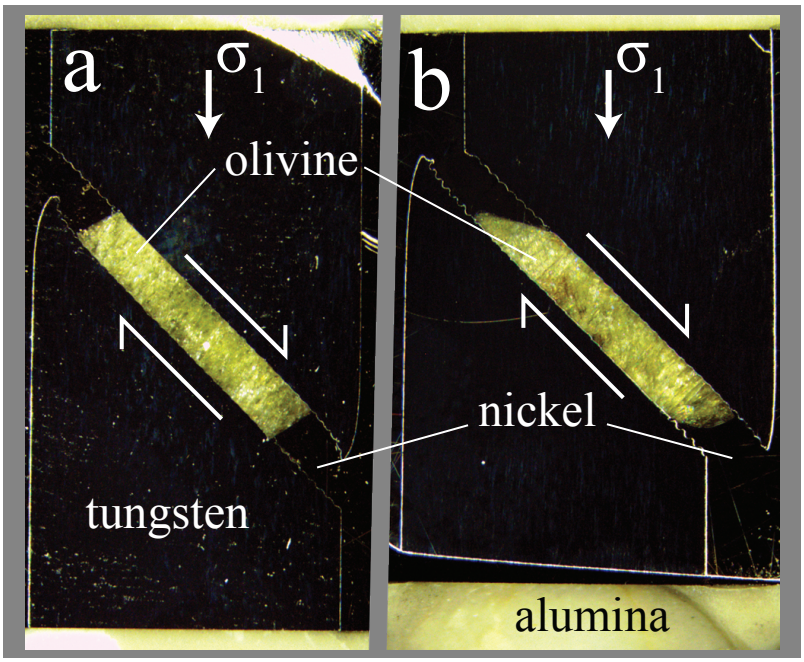

Figure 2.3: Reflected light image of deformed crystals. (a) Sample PI-1709 was oriented for maximum resolved shear stress on the (100)[001] slip system and deformed at 1200°C to a shear strain of 0.35. (b) Sample PI-1721 was oriented for maximum resolved shear stress on the (001)[100] slip system and deformed at 1300°C to a shear strain of 1.6. The slight bending at the tip of the tungsten pistons is from the nickel capsule flowing into the void next to the crystal during the pressurization process. The bright line above the alumina spacer in (b) is an artifact that formed at the extent of the polished surface because the bottommost portion of the assembly was not polished.

1991; *Hirth and Kohlstedt*, 2003). The power-law relationship determined for crystals oriented for shear on the (001)[100] dislocation slip system is

$$\dot{\varepsilon}_{\mathrm{power}}^{(001)[100]} = 10^{6.3\pm1.0}\sigma^{3.5}\exp\left(\frac{-540 \pm 30\ \mathrm{kJ/mol}}{\mathrm{R}T}\right). \tag{2.5}$$

In the same manner but excluding the highest load step at both 1200° and 1300°C, flow law parameters for crystals oriented for shear on the (100)[001] slip system were determined by fitting the data at 1200° and 1300°C using Equation 2.1. The power-law relationship for crystals oriented for shear on the (100)[001] slip system is

$$\dot{\varepsilon}_{\mathrm{power}}^{(100)[001]} = 10^{1.4\pm1.2}\sigma^{3.5}\exp\left(\frac{-410 \pm 40\ \mathrm{kJ/mol}}{\mathrm{R}T}\right). \tag{2.6}$$

Once the parameters for the power-law relationship were determined, the data were fit to determine the parameters in Equation 2.2. The large number of parameters in Equation 2.2 necessitated holding some of the parameters constant during the fitting procedure. Values of 0.5 and 2 were chosen for *p* and *q*, respectively. Results for fitting the data using a range of values of p and q are presented in Appendix B. The values of $p = 0.5$ and $q = 2$ are consistent with observations of olivine deforming at low temperature conditions from a review of published work (*Demouchy et al.*, 2013). In addition, the strain rate from some of the load steps for data at 1100°C contained a significant contribution of deformation in the power-law regime to the measured strain rate. To account for the contribution of strain rate from the power-law regime, the data were fit for the values of the flow law parameters using

$$\dot{\varepsilon}_{\,\mathrm{total}} = \dot{\varepsilon}_{\,\mathrm{power}} + \dot{\varepsilon}_{\,\mathrm{exp}}, \tag{2.7}$$

where $\dot{\varepsilon}_{\mathrm{total}}$ is the equivalent strain rate from the experiments in Table 2.1, $\dot{\varepsilon}_{\mathrm{power}}$ is the strain rate from Equation 2.5 at the given conditions, and $\dot{\varepsilon}_{\mathrm{exp}}$ is Equation 2.2, which contains the parameters of interest (i.e., A_e, Q_e, and σ_{e}). This procedure yielded

$$\dot{\varepsilon}_{\exp}^{(001)[100]} = 10^{5.1\pm1.0}\sigma^{1.4}\exp\left[\left(\frac{-475 \pm 40\ \mathrm{kJ/mol}}{\mathrm{R}T}\right)\left(1-\left(\frac{\sigma}{28\ \pm 4.0\ \mathrm{GPa}}\right)^{0.5}\right)^{2}\right], \tag{2.8}$$

for crystals oriented for shear on the (001)[100] slip system.

The data from load steps at 1100°C and the highest load step at both 1200° and 1300°C, which deviate from power-law behavior, were used to determine the parameters A_e, Q_e, and σ_{e} for crystals oriented for shear on the (100)[001] slip system. This procedure yielded

$$\dot{\varepsilon}_{\exp}^{(100)[001]} = 10^{2.4\pm0.4}\sigma^{1.4}\exp\left[\left(\frac{-455 \pm 30\ \mathrm{kJ/mol}}{\mathrm{R}T}\right)\left(1-\left(\frac{\sigma}{8.5 \pm 1.0\ \mathrm{GPa}}\right)^{0.5}\right)^{2}\right], \tag{2.9}$$

for crystals oriented for shear on the (100)[001] slip system. Equations 2.5, 2.6, 2.8, and 2.9 are in good agreement with the experimentally measured values of strain rate and stress at a temperature, as presented in Figure 2.4.

2.3.2 Microstructural Results

Orientation maps and pole figures compiled from EBSD measurements reveal the development of intracrystalline misorientation and low-angle boundaries in the deformed crystals. Rotational axes parallel to [010] are dominant as presented in the inverse pole figures in Figure 2.5. Low-angle boundaries present in the deformed samples in Figure 2.6 preferentially form perpendicular to the shear plane. The formation of low-angle boundaries is accompanied by minor rotation of the [100] and [001] crystallographic axes, as is apparent in the pole figures presented in Figure 2.6. This rotation has only a minor influence on the amount of resolved shear stress acting upon the dominant slip system in each sample because the largest volume of each crystal remains near a Schmid factor of 0.5 even after deformation to a shear strain of 1.6, as presented in Figure 2.6b.

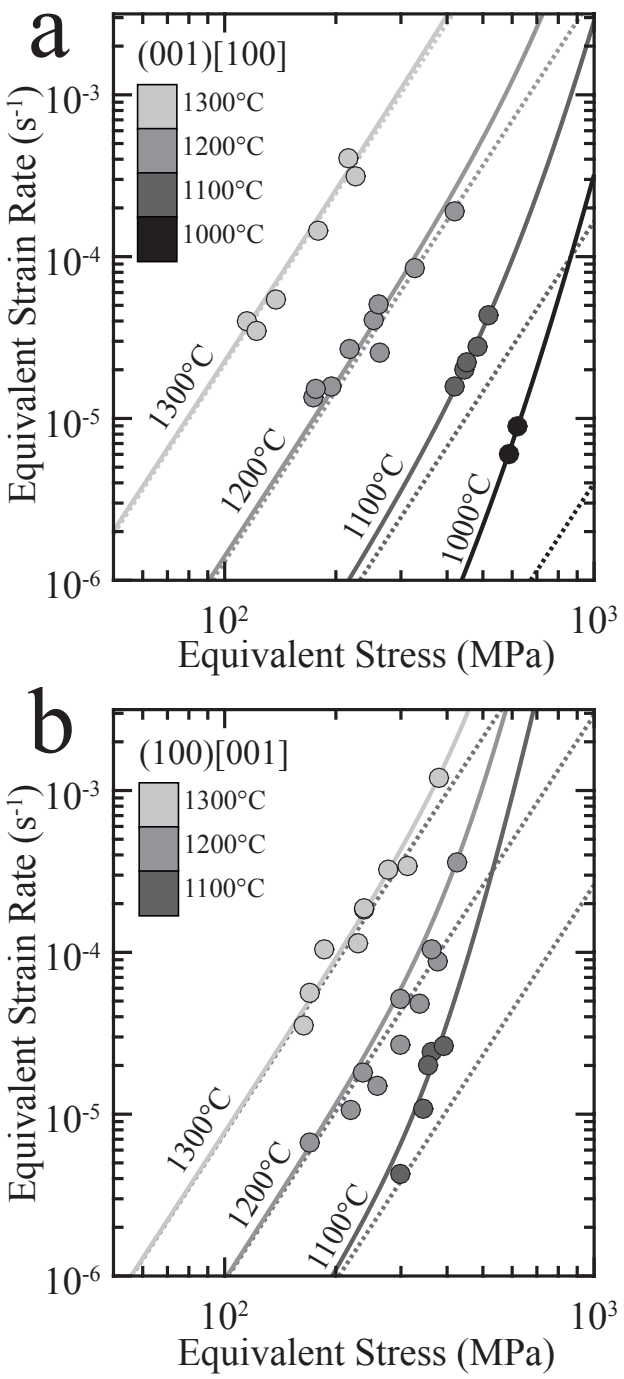

Figure 2.4: Plot of equivalent strain rate as a function of equivalent stress from direct shear experiments carried out on crystals oriented for slip on the (a) (001)[100] and (b) (100)[001] dislocation slip systems. The dotted lines in (a) are Equation 2.5 and the solid lines are the sum of Equations 2.5 and 2.8. The dotted lines in (b) are Equation 2.6 and the solid lines are the sum of Equations 2.6 and 2.9.

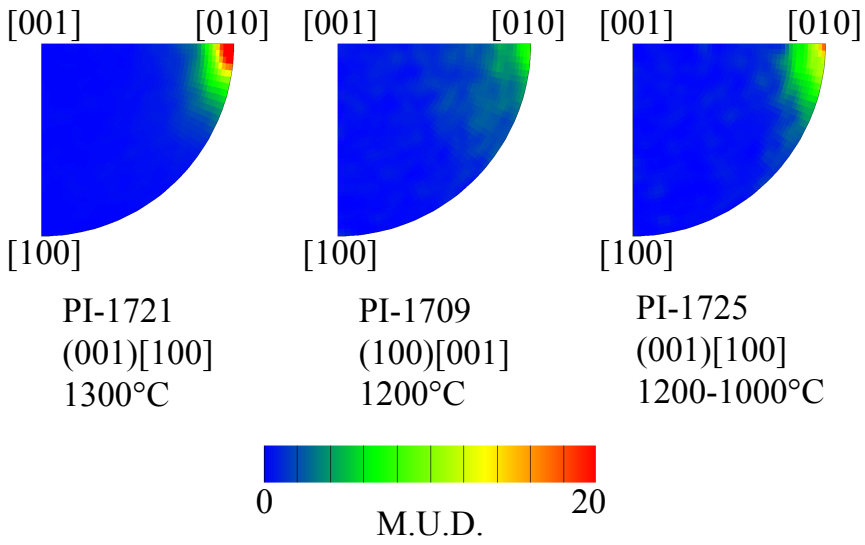

Figure 2.5: Inverse pole figures of misorientation axes in the crystallographic reference frame. Rotational axes are for misorientations between 1 and 10 degrees between neighboring pixels from EBSD maps of deformed samples. The scale for multiples of a uniform distribution for the pole figures correlates with the color bar on the bottom. Note the concentration of rotational axes about [010], consistent with deformation via the motion of dislocations on the (001)[100] and/or (100)[001] slip systems.

.

2.4 Discussion

The flow laws presented in Equations 2.5 and 2.8 as well as 2.6 and 2.9 describe deformation occurring by two independent dislocation mechanisms for the (001)[100] and (100)[001] slip systems, respectively. At high-temperature and low-stress conditions, the mechanical data for these two slip systems are well described by Equations 2.5 and 2.6, consistent with deformation operating by climb-controlled dislocation creep that is limited in rate by diffusion of silicon along dislocation cores (*Hirth and Kohlstedt*, 2015). At low-temperature and high-stress conditions, the mechanical data are well described by Equations 2.8 and 2.9, consistent with deformation occurring by glide-controlled dislocation creep that is limited by the rate at which dislocations glide to overcome lattice resistance or obstacles in the crystal lattice (*Frost and Ashby*, 1982, p. 6-9).

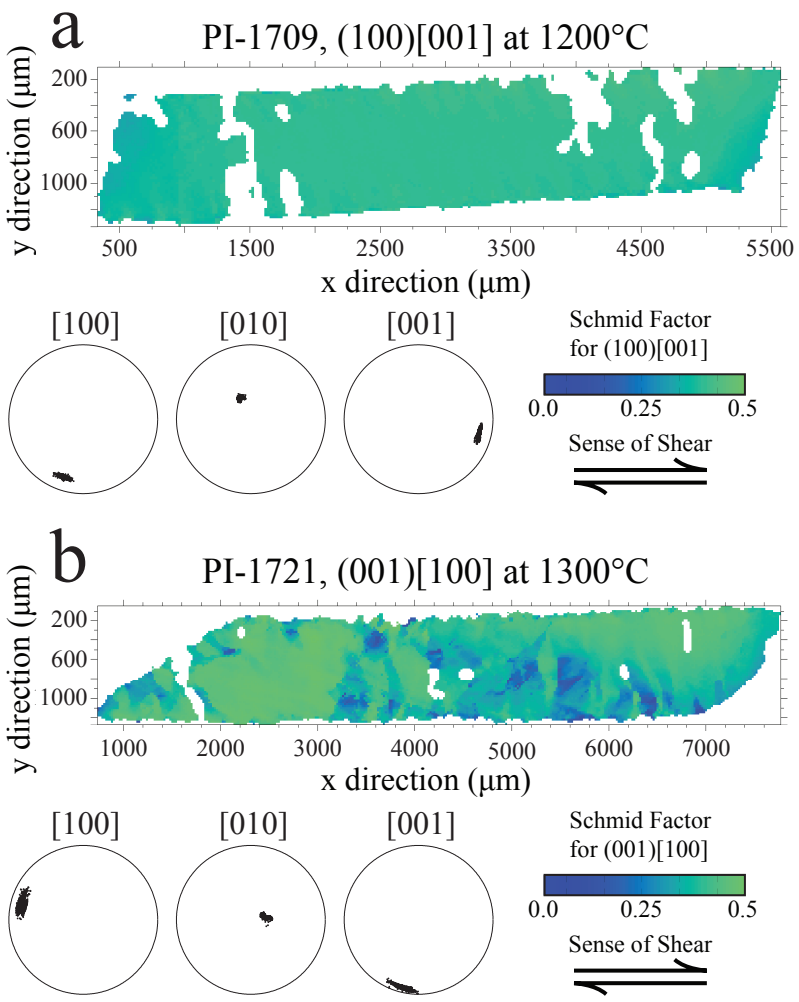

Figure 2.6: Maps of Schmid factor from EBSD data and equal area lower-hemisphere pole figures showing orientations for samples (a) PI-1709 and (b) PI-1721. Values of Schmid factor in the maps correlate with the color bar below each map. Note the development of vertically oriented low-angle boundaries that are apparent by the changes in Schmid factor in (b).

Analyses of EBSD measurements indicate that deformation occurred primarily by the glide of dislocations on the (001)[100] or the (100)[001] slip systems. Previous researchers used gradients in intracrystalline orientation (i.e., misorientation) and the development of low-angle boundaries to infer the activity of individual slip systems (e.g., *Lloyd et al.*, 1997; *Prior et al.*, 2002; *Hildyard et al.*, 2009; *Hansen et al.*, 2014). In a similar manner, the misorientation axes plotted in the crystallographic reference frame in Figure 2.5 have strong maxima of rotational axes parallel to the [010] crystallographic axis, which can form by the operation of dislocations on either the (001)[100] or the (100)[001] slip systems. The development of low-angle boundaries and rotation of the [100] and [001] axes about [010] plotted in the sample reference frame in Figure 2.6 are also consistent with deformation occurring by the motion of dislocations on either the (001)[100] or the (100)[001] slip system.

The relative strength of the (001)[100] and (100)[001] slip systems is strongly dependent upon temperature and stress, as presented in Figure 2.7. At high temperatures and low stresses in the power-law regime, the flow law for the (001)[100] slip system is in agreement with the flow law for $[101]_{\mathrm{c}}$ and is weaker than the (100)[001] slip system. Conversely, at low-temperature and high stress, in the exponential creep regime, the (100)[001] slip system in agreement with the flow law for $[101]_{\mathrm{c}}$ and is weaker than the (001)[100] slip system. The relative strengths of the slip systems during in the different regimes provides an opportunity to gain insight into important microphysical processes that govern deformation.

The observed weakness of the (001)[100] slip system relative to the (100)[001] slip system at high temperatures and low stresses allows for evaluation of the processes that govern deformation of olivine in a climb-controlled dislocaion creep regime. The climb-controlled model of dislocation creep (*Hirth and Lothe*, 1968, p. 506-519), which describes the strain rate of a material deforming by dislocation creep as rate limited by the velocity of climb, v_{c}, which is expressed as

$$v_{\mathrm{c}} = 2\pi \frac{\sigma V_{\mathrm{m}}}{\mathrm{R}T} \frac{D}{b} \frac{1}{\ln\left(R_{\mathrm{o}}/r_{\mathrm{o}}\right)}, \tag{2.10}$$

where V_{m} is the molar volume of the crystal, D is the diffusion coefficient of the slowest diffusing species, b is the Burgers vector, R_{o} is the dislocation spacing, and r_{o} is the dislocation core radius. This relationship states that the velocity of climb, and therefore the strain rate, is proportional to D. The value of n for both triaxial compression and direct shear experiments at high temperatures is $\sim$3.5, consistent with diffusion along the cores of dislocations (*Hirth and Kohlstedt*, 2015). Therefore, the observed difference in the temperature dependence and strength of the two slip systems likely reflects a difference in diffusivity along dislocations with either [100] or [001] Burgers vectors.

At low-temperature and high-stress conditions in the glide-controlled regime, the (001)[100] slip system is stronger than the (100)[001] slip system. At these conditions, deformation is rate limited by the ability of dislocations to either move through obstacles in the crystal lattice or to overcome the lattice resistance. The Peierls stress describes the stress needed to overcome lattice resistance in the absence of thermal energy. Therefore, the relative strength of (001)[100] and (100)[001] slip systems in the glide-controlled regimes may be used to evaluate values of Peierls stress for the two slip systems considered in this study.

Dislocation dynamics simulations of glide velocity (*Durinck et al.*, 2007a) and calculations of the properties of dislocation cores (*Durinck et al.*, 2007b) have been used to determine values of Peierls stress for dislocations on the (001)[100] and (100)[001] slip systems in olivine. Importantly, the calculations predict larger values of Peierls stress for both screw and edge dislocations operating on the (001)[100] than for dislocations on the (100)[001] slip system. The differences between the absolute values of Peierls stress determined from the calculations and the values of σ_{e} in the flow laws in Equations 2.8 and 2.9 is likely attributed to the operation of mixed dislocations in our samples or the different values of parameters (i.e., p and q in Equation 2.2) used in our analyses. Nonetheless, consideration of the values of Peierls stress from the calculations in terms of the glide-controlled model of dislocation creep is consistent with the strain rate from dislocations on the (001)[100] slip system being much slower than that of the (100)[001] slip system, a condition consistent with our results.

Consideration of the results presented above with previous results from compressive creep

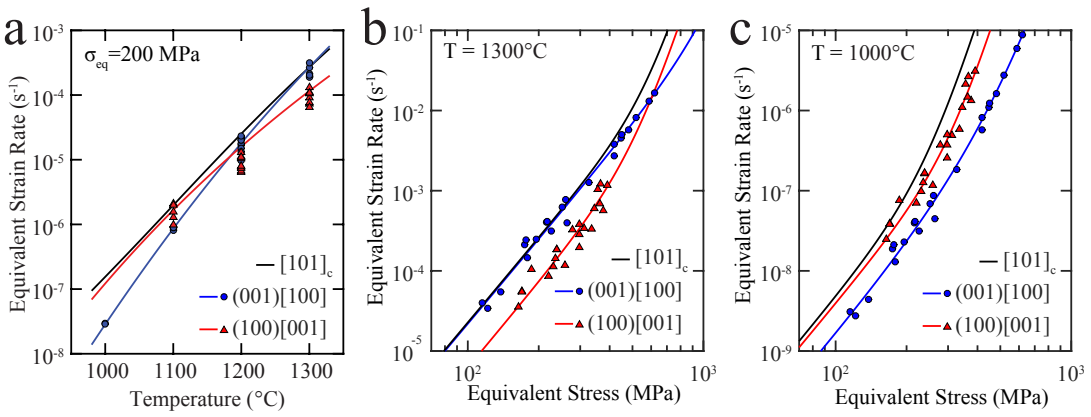

Figure 2.7: Plots of equivalent strain rate as a function of (a) temperature at normalized stress and (b,c) stress at normalized temperature with the flow laws for crystals deformed in triaxial compression in the $[101]_c$ orientation or in direct shear for deformation on either the (001)[100] or the (100)[001] slip systems. The lines represent flow laws consisting of power law and exponential components that are treated as two independent mechanisms (i.e., combined using Equation 2.7). The black lines are from a fit of triaxial compression experiments described in Tielke et al. (in prep), the blue lines are from crystals oriented for shear on (001)[100], and the red lines are from crystals oriented for shear on (100)[001]. The circles and triangles are the data in Table 2.1 normalized to (a) an equivalent stress of 200 MPa, (b) a temperature of 1300°C, or (c) a temperature of 1000°C using the flow law parameters from Equations 2.5 and 2.8 for (001)[100] and from Equations 2.6 and 2.9 for (100)[001].

experiments gives insight into the relative strengths of the four dominate dislocation slip systems in olivine. At lower-temperature and higher-stress conditions, crystals deformed in triaxial compression in the $[101]_c$ orientation are weaker than those deformed in the $[110]_c$ and $[011]_c$ orientations (*Phakey et al.*, 1972; *Goetze*, 1978; *Evans and Goetze*, 1979). Importantly, the results presented in Figure 2.7 demonstrate that equivalent strain rates of crystals oriented for shear on (100)[001] are approximately equal to the strain rates of crystals in the $[101]_c$ at an equivalent stress of 200 MPa and a temperature $\approx$1100°C. Therefore, (100)[001] is likely the weakest of the four dominate dislocation slip systems in olivine at low-temperature and high-stress conditions.

Extrapolation of the flow laws derived from the experiments in this study to the upper mantle conditions presented in Figure 2.8 predicts an even larger difference between the strength of the (100)[001] and (001)[100] slip systems. For conditions typical of Earth's lithospheric mantle (σ_{eq} = 20 MPa and T = 900°C), the strain rate of the (100)[001] slip system is a factor of $\sim$10 times faster than that of the (001)[100] slip system. For conditions typical of Earth's asthenospheric upper mantle (σ_{eq} = 0.1 MPa and T = 1400°C), the equivalent strain rate of the (001)[100] slip system is a factor of $\sim$5 times faster than that of the (100)[001] slip system.

Our results predict an LPO should develop with a maximum of [001] parallel to the shear direction in olivine-rich rocks deforming at lithospheric conditions where the (100)[001] slip systems is the weakest. Other workers have reported the relative strength of slip systems are dependent upon pressure (*Couvy et al.*, 2004; *Mainprice et al.*, 2005; *Raterron et al.*, 2007, 2009) and predict the development of an LPO with [001] parallel to the shear direction at high pressure conditions. These observations highlight the need for deformation experiments carried out on olivine single crystals and aggregates over a large range of temperature, stress, and pressure in order to gain deeper understanding into the mechanisms of LPO development in Earth's mantle.

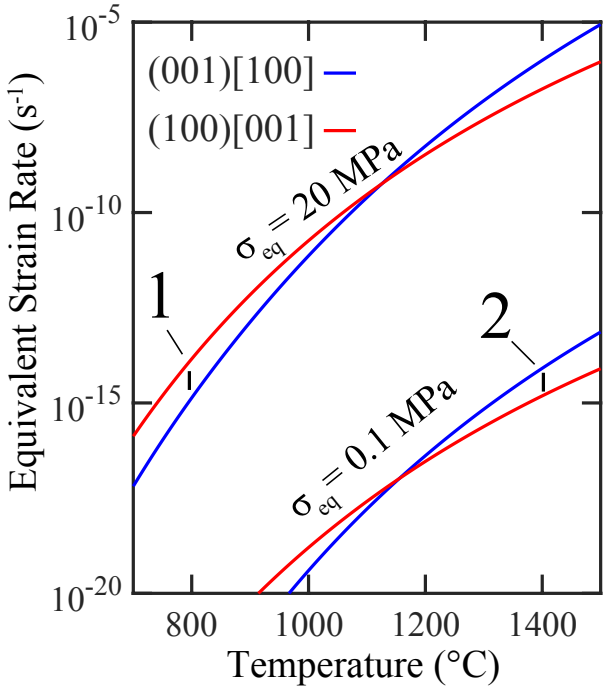

Figure 2.8: Equivalent strain rates from the constitutive equations derived from crystals oriented for shear on either the (001)[100] or the (100)[001] slip system extrapolated to a typical lithospheric stress of 20 MPa and a typical asthenospheric stress of 0.1 MPa. The lines represent the flow laws for the power-law and exponential creep regimes for each orientation, combined using Equation 2.7 for lithospheric conditions. For asthenospheric conditions only the power laws were used. For an equivalent stress of 20 MPa at 800°C, represented by line 1, the equivalent strain rate of the (100)[001] slip system is ∼10 times larger than that of the (001)[100] slip system. For an equivalent stress of 0.1 MPa at 1400°C, represented by the line 2, the equivalent strain rate of the (001)[100] slip system is ∼5 times larger than that of the (100)[001] slip system.

2.5 Conclusions

The results presented above are consistent with temperature and stress dependence of the relative strength of the (001)[100] and (100)[001] dislocation slip systems in olivine. At high temperatures ($\geq$ 1200°C) and low stress ($\leq$ 200 MPa), the (001)[100] slip system is weaker than the (100)[001] slip system, whereas at lower temperature and higher stress the (100)[001] slip system is weaker than the (001)[100] slip system. The transition in the weakest slip system coincides with a transition in rheological regimes. At high temperatures, strain rate follows a power-law relationship with stress consistent with a climb-controlled dislocation regime where (001)[100] is the weakest. At low temperatures, strain rate is an exponential function of stress, consistent with a glide-controlled regime where (100)[001] is weakest.

2.6 Acknowledgments

This work benefited greatly from discussions with Amanda Dillman and Shenghua Mei and was supported by NASA PG&G grants NNX10AM95G and NNX15AL53G. Parts of this work were carried out in the Characterization Facility, University of Minnesota, which receives partial support from NSF through the MRSEC program.

Chapter 3

Hydrolytic weakening in olivine single crystals deforming by dislocation creep at mantle temperatures

Deformation experiments on single crystals of San Carlos olivine under hydrous (hydrogen-rich) conditions were performed to investigate the microphysical processes responsible for hydrolytic weakening during dislocation creep. Crystals were oriented relative to the applied load in triaxial compression to exert the maximum shear stress on the (100)[001] and (001)[100] dislocation slip systems, that is, the $[101]_c$ orientation. Hydrogen was supplied to the crystals using either talc or brucite sealed in nickel capsules with the crystal. Deformation experiments were carried out using a gas-medium apparatus with high resolution in temperature ($\pm$2°C) and stress ($\pm$2 MPa) at 1050° to 1250°C, differential stresses of 45 to 306 MPa, and resultant strain rates of 1.5 x 10^{-6} to 4.4 x 10^{-4} s^{-1}. Hydroxyl concentrations determined using Fourier transform infrared spectroscopy varied from 190 to 260 ppm H/Si. For talc-buffered (i.e., water and orthopyroxene buffered) samples at high temperatures, the dependence of strain rate on stress follows a power-law relationship with a stress exponent (n) of $\sim$2.5 and an activation energy (Q) of $\sim$480 kJ/mol. By comparison, samples deformed under anhydrous conditions and

buffered by orthopyroxene yield $n \approx 3.5$ and $Q \approx 470$ kJ/mol. Brucite-buffered (i.e., water and periclase-buffered) samples deformed faster than talc-buffered samples but contained similar hydrogen concentrations, demonstrating that strain rate is influenced by orthopyroxene activity under hydrous conditions. The values of n and dependence of strain rate upon orthopyroxene activity are consistent with hydrolytic weakening occurring in the climb-controlled dislocation creep regime that is associated with deformation controlled by lattice diffusion under hydrous conditions and by pipe diffusion under anhydrous conditions. At lower temperatures and higher stresses, under both hydrous and anhydrous conditions, the strain rate of orthopyroxene-buffered samples follows an exponential relationship with stress. Analyses of post-deformation electron-backscatter diffraction data demonstrate that dislocations with [100] Burgers vectors are dominant during in the climb-controlled regime and dislocations with [001] are dominant in the glide-controlled regime. Extrapolation of the constitutive equations derived in this study to conditions of stress and temperature of the asthenospheric mantle demonstrates that crystals deformed under hydrous conditions (containing $\sim$200 ppm H/Si, a lower-bound for mantle conditions) will deform one to two orders of magnitude faster than crystals deformed under anhydrous conditions.

3.1 Introduction

The rate of plastic deformation of upper mantle materials controls many important geophysical processes, including convection in Earth's upper mantle and the associated movements of Earth's tectonic plates. The strength of nominally anhydrous silicate minerals is strongly influenced by the addition of hydrogen as a point defect, a phenomenon referred to as hydrolytic weakening. A large literature documents hydrolytic weakening of olivine, the major mantle phase, during high-temperature ($\geq 1200^{\circ}$C) deformation experiments (e.g., *Carter and Ave'Lallemant*, 1970; *Chopra and Paterson*, 1984; *Mackwell et al.*, 1985; *Karato et al.*, 1986; *Mei and Kohlstedt*, 2000a,b). However, few studies have attempted to quantify hydrolytic weakening of olivine at low-temperature ($< 1200^{\circ}$C) conditions (e.g., *Katayama and Karato*, 2008).

The goal of this study was to carry out experiments over a range of temperatures that span the transition from lithospheric to asthenospheric conditions in order to quantify hydrolytic weakening in olivine deforming by dislocation creep and gain greater understanding into the microphysical processes responsible for this phenomenon.

Hydrolytic weakening has been observed in constant displacement rate experiments carried out on olivine single crystals. Crystals deformed at 1300°C and a confining pressure of 300 MPa with 270 to 420 ppm H/Si, as determined from FTIR spectra calibration (*Paterson*, 1982) multiplied by a factor of 3.5 (*Bell et al.*, 2003), deform at a factor of 1.4 to 2.5 lower flow stress than crystals deformed under anhydrous conditions (*Mackwell et al.*, 1985). Similarly, crystals deformed at 1200°C and a confining pressure of 4 to 7 GPa with 1030 to 2520 ppm H/Si deform at a factor of 1.3 to 1.6 lower flow stress than crystals under anhydrous conditions (*Girard et al.*, 2013).

Hydrolytic weakening has also been observed in constant load experiments preformed on olivine single crystals. Crystals deformed at 1184° to 1561°C and at atmospheric pressure in the presence of H_2/H_2O gas mixtures have been reported to deform roughly one order of magnitude faster than crystals deformed in the presence of CO/CO_2 gas mixtures (*Poumellec and Jaoul*, 1984). The increase in strain rate for a given stress reported in these experiments corresponds to a reduction in flow stress of a factor of $\sim$2 if a strain rate is dependent on stress to the power of 3.

Hydrolytic weakening occurs during experimental deformation of olivine-bearing rocks and olivine aggregates deforming by multiple deformation mechanisms. Natural dunites deformed in the climb-controlled dislocation creep regime were significantly weaker under hydrous conditions than under anhydrous conditions (*Carter and Ave'Lallemant*, 1970; *Chopra and Paterson*, 1984). Fine-grained olivine aggregates deformed in both the climb-controlled dislocation creep and diffusion creep regimes exhibit significant hydrolytic weakening (*Karato et al.*, 1986; *Mei and Kohlstedt*, 2000a,b). Olivine aggregates deforming by grain-boundary sliding (*McDonnell et al.*, 1999) and by glide-controlled dislocation creep (*Katayama and Karato*, 2008) also reveal hydrolytic weakening.

3.2 Theoretical Background

3.2.1 A Climb-controlled Model of Dislocation Creep

A climb-controlled model of dislocation creep is often used to describe the strain rate, $\dot{\varepsilon}$, of a material deforming by the motion of dislocations at conditions of high temperature and low stress (e.g., *Mott*, 1951; *Weertman*, 1955; *Poirier*, 1985, p. 94-144). This model is based on the Orowan equation, which states that

$$\dot{\varepsilon} = \rho b \bar{v}, \tag{3.1}$$

where ρ is the density of mobile dislocations, b is the Burgers vector, and $\bar{v}$ is the mean velocity of dislocations. The dislocation density is primarily controlled by stress for olivine and follows the relationship

$$\rho \propto \sigma^{1.4}, \tag{3.2}$$

(*Bai and Kohlstedt*, 1992). Commonly observed Burgers vectors are [100] and [001] for olivine deforming in the climb-controlled regime (*Phakey et al.*, 1972; *Goetze and Kohlstedt*, 1973). During climb-controlled dislocation creep, strain rate is primarily controlled by the rate at which dislocations can climb to overcome impediments such as sessile dislocations. Under these conditions, $\bar{v}$ can be described by

$$\bar{v} = \frac{l_g}{l_c} v_c, \tag{3.3}$$

where l_g is the glide distance and l_c is the climb distance (*Weertman*, 1999). The climb velocity, v_c, is given by

$$v_{\mathrm{c}} = 2\pi \frac{\sigma V_{\mathrm{m}}}{\mathrm{R}T} \frac{D_{\mathrm{vol}}}{b} \frac{1}{\ln\left(R_{\mathrm{o}}/r_{\mathrm{c}}\right)}, \tag{3.4}$$

where V_{m} is the molar volume of the crystal, R is the gas constant, T is the absolute temperature, D_{vol} is the self-diffusion coefficient of the slowest species diffusing through grain interiors,

which for the case of olivine is silicon under both anhydrous (*Dohmen et al.*, 2002) and hydrous conditions (*Costa and Chakraborty*, 2008), b is the Burgers vector, R_o is the average spacing between dislocations, and r_c is the radius of the dislocation core (*Hirth and Lothe*, 1968, p. 506-519). By combining Equations 3.1, 3.2, and 3.4, we arrive at

$$\dot{\varepsilon} \propto \rho\, \sigma D_{\mathrm{vol}} \propto \sigma^{2.4} D_{\mathrm{vol}}, \tag{3.5}$$

if strain rate is limited by diffusion of the slowest diffusing species through the crystal lattice.

A different dependence of strain rate on stress is predicted if strain rate is rate limited by diffusion of the slowest species along the cores of dislocations, often referred to as pipe diffusion. When pipe diffusion is important, the strain rate is given by

$$\dot{\varepsilon} \propto \rho^2 \sigma D_{\mathrm{pipe}}, \tag{3.6}$$

where D_{pipe} is diffusion of the slowest species through dislocation cores (*Spingarn et al.*, 1979). For olivine, using Equation 3.2, this expression becomes

$$\dot{\varepsilon} \propto \sigma^{3.8} D_{\mathrm{pipe}}. \tag{3.7}$$

Empirically derived constitutive equations for high-temperature creep are thus often expressed in the general form

$$\dot{\varepsilon}_{\mathrm{climb}} = A_{\mathrm{c}} \sigma^n \exp\left(\frac{-Q_{\mathrm{c}}}{\mathrm{R}T}\right), \tag{3.8}$$

where A_{c} is a material-specific parameter, n is the stress exponent, and Q_{c} is the activation energy.

3.2.2 Hydrolytic Weakening in the Climb-controlled Regime

The climb-controlled model of dislocation creep connects microphysical processes, including the formation of point defects and rates of diffusion, to macroscopic observations of hydrolytic weakening. As hydrogen enters the olivine lattice in the form of charged point defects (protons),

it influences the concentrations of vacancies on the metal, silicon, and oxygen sublattices. For diffusion of silicon by a vacancy mechanism, the relationship between the self-diffusivity of silicon ($D_{\mathrm{Si}}^{\mathrm{vol}}$) and the concentration of silicon vacancies ($X_{\mathrm{V_{Si}}}$) is

$$D_{\mathrm{Si}}^{\mathrm{vol}} = X_{\mathrm{V_{Si}}}\, D_{\mathrm{V_{Si}}}, \tag{3.9}$$

where $D_{\mathrm{V_{Si}}}$ is the diffusion coefficient for vacancies on the silicon sublattice (*Nakamura and Schmalzried*, 1983). Modification of the $X_{\mathrm{V_{Si}}}$ term in Equation 3.9 provides an explanation for how structurally incorporated hydrogen influences the strength of olivine at high-temperature conditions. The relationship between strain rate and water fugacity ($f_{\mathrm{H_2O}}$) can be expressed by combining the relationships in Equations 3.5 and 3.9 with the known dependence of strain rate on $f_{\mathrm{H_2O}}$, as

$$\dot{\varepsilon} \propto D_{\mathrm{Si}}^{\mathrm{vol}} \propto X_{\mathrm{V_{Si}}} \propto f_{\mathrm{H_2O}}^{r}, \tag{3.10}$$

where $r \approx 1$ (*Mei and Kohlstedt*, 2000b). The empirically derived value of $r \approx 1$ is consistent with $X_{\mathrm{V_{Si}}}$ forming point defects associated with either one or two or three hydrogen atoms near a silicon vacancy (*Kohlstedt*, 2006). It is important to note that although hydrogen ions also enter the olivine lattice in association with metal vacancies, the dominant means by which hydrogen affects strain rate in the climb-controlled regime is through its influence on the concentration of silicon vacancies.

3.2.3 A Glide-controlled Model of Dislocation Creep

For deformation at lower temperature and higher stress conditions, a glide-controlled model of dislocation creep has been employed to describe the strain rate as a function of stress and temperature for a plastically deforming material. During deformation in a glide-controlled regime, strain rate is limited by the ability of dislocations to overcome obstacles such as other dislocations, inclusions, grain boundaries, or the lattice resistance (*Frost and Ashby*, 1982, p. 7-8). Similar to the climb-controlled model, the glide-controlled model is derived from Equation 3.1,

with the relationship between dislocation density and stress expressed by Equation 3.2. In the glide-controlled model $\bar{v}$ is taken as the velocity of glide (v_g), which can be described by

$$v_g \propto \exp\left[\left(\frac{-Q_{\mathrm{g}}}{\mathrm{R}T}\right)\left(1-\left(\frac{\sigma}{\sigma_{\mathrm{g}}}\right)^{p}\right)^{q}\right], \tag{3.11}$$

where Q_{g} is the activation energy of glide, σ_{g} is the critical stress required to move dislocations in the absence of thermal energy, and p and q are parameters describing the shape and spacing of the impediments to dislocation motion (*Kocks*, 1976). Values of p and q range from 0.5 to 1 and from 1 to 2, respectively. Combining Equations 3.1 and 3.11 leads to the following relationship for a material deforming during glide-controlled creep:

$$\dot{\varepsilon}_{\mathrm{glide}} = A_{\mathrm{g}}\sigma^{1.4}\exp\left[\left(\frac{-Q_{\mathrm{g}}}{\mathrm{R}T}\right)\left(1-\left(\frac{\sigma}{\sigma_{\mathrm{g}}}\right)^{p}\right)^{q}\right], \tag{3.12}$$

where A_{g} is a material-dependent parameter. For olivine, the reported values for Q_{g}, σ_{g}, p, and q vary significantly among several studies (e.g., *Evans and Goetze*, 1979; *Raterron et al.*, 2004; *Mei et al.*, 2010; *Long et al.*, 2011; *Demouchy et al.*, 2013).

3.2.4 Hydrolytic Weakening in the Glide-controlled Regime

The theory of hydrolytic weakening for the glide-controlled regime is less well established than for the climb-controlled regime. One hypothesis for hydrolytic weakening in the glide-controlled regime that is rate limited by the ablility of dislocations to overcome the lattice resistance is that σ_{e} is lowered when hydrogen ions weaken Si-O bonds in silicate crystals (*Griggs*, 1967). The process of lowering σ_{e} results in lower energy of kink formation and propagation. In turn, the increased propagation rate of kinks results in faster rates of glide and, therefore, faster strain rates (*Katayama and Karato*, 2008).

3.3 Methods

3.3.1 Sample Preparation

The starting materials for all of the experiments in this study were oriented single crystals of San Carlos olivine. Crystal orientations were determined from electron backscatter diffraction (EBSD) measurements carried out on flat surfaces that were polished using diamond-lapping film and colloidal silica. The crystals were then oriented relative to a diamond saw blade and cut into rectangular parallelepipeds with dimensions of 8.0 x 3.9 x 4.1 mm. The samples were cut in the $[101]_{\mathrm{c}}$ orientation, with the long axes of the samples at 45° to [100] and [001], so that both the (001)[100] and the (100)[001] dislocation slip system would be activated during deformation.

For each experiment, an oriented crystal was placed into a nickel capsule with a 7 mm outer diameter, as illustrated in Figure 3.1. Hydrogen was supplied to each crystal by the addition of either talc or brucite powder placed along the edges of the sample in combination with a drop of deionized water added immediately before the capsule was sealed using a laser welder. In addition to supplying hydrogen to the samples, talc and brucite control the chemical environment at different orthopyroxene activities (a_{opx}) resulting from their reaction products. At high temperatures, talc dehydrates via the reaction

$$\mathrm{Mg_3Si_4O_{10}(OH)_2} \longrightarrow 3\,\mathrm{MgSiO_3} + \mathrm{SiO_2} + \mathrm{H_2O}, \tag{3.13}$$

to produce water, orthopyroxene, and excess silica, which buffers the crystals at high a_{opx} at experimental conditions. The excess silica produced from the dehydration of talc reacts with olivine to form a thin layer of orthopyroxene on the surface of the crystal (e.g., *Girard et al.*, 2013). At high temperatures, brucite dehydrates to

$$\mathrm{Mg(OH)_2} \longrightarrow \mathrm{MgO} + \mathrm{H_2O}, \tag{3.14}$$

producing water and periclase, which buffers the crystals at a lower a_{opx} at experimental conditions.

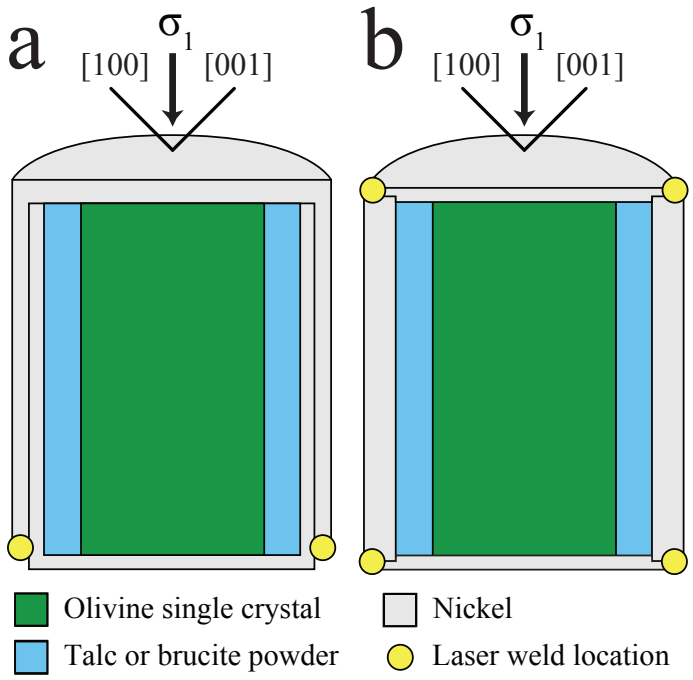

Figure 3.1: Illustrations representing the capsules and deformation geometry for experiments performed in this study. (a) Interlocking thin-walled cylinders of nickel were used in initial experiments. (b) Thin-walled nickel cylinders with nickel caps were used in later experiments. The buffering material, either talc or brucite, was sealed inside the capsule by laser welding. The orientation of compressive stress was at 45° to the [100] and [001] olivine crystallographic axes.

For each experiment, the laser-welded nickel capsule was inserted between alumina and zirconia pistons and placed inside of an iron jacket. The nickel capsule that contained the single crystal was positioned in the hot zone of a furnace inside of a gas-medium deformation apparatus (*Paterson*, 1990). Temperature was measured using an R-type thermocouple placed adjacent to the capsule and maintained to within ±2°C during the duration of each experiment based on the temperature profile obtained from a calibration run. Each crystal was annealed at 1250°C and a confining pressure of 300 MPa for 75 minutes to allow hydrogen to diffuse into

the olivine crystal. each crystal was subsequently deformed at 1250°, 1200°, 1150°, or 1050°C.

3.3.2 Deformation Experiments

For the deformation portion of each experiment, the actuator was advanced toward the sample at a rate of 0.01 mm/s until a load of 0.5 kN (corresponding to a stress of ∼30 MPa) was registered. The actuator was then advanced at a rate of 0.001 mm/s until a predetermined higher load was achieved. Next, the actuator was set to load control, and the crystal was deformed using a series of constant load steps, starting with small loads and progressing to larger loads. During each step, the load was maintained until the displacement rate became constant. At the end of each load-stepping sequence, deformation at a smaller load was repeated. Comparison of the strain rate from the last load step of the experiment to the strain rate from an earlier portion of the experiment at a similar load was used to test for strain hardening or loss of water during the experiment. After each experiment, the temperature was lowered to below 900°C within 10 minutes. Temperature and pressure were then simultaneously lowered to 100°C and 100 MPa, at which point the remaining pressure was released. The load applied to the crystals was calculated by subtracting the load supported by the nickel capsule and the iron jackets using published flow laws (*Frost and Ashby*, 1982, p. 21) and in-lab calibrations.

3.3.3 FTIR Analyses

Fourier transform infrared spectroscopy (FTIR) analyses were carried out on the starting material, a sample after the hydration anneal, and samples after deformation. Samples were prepared for FTIR analyses by extracting slices parallel to (010) from the center of each sample. The slices were adhered to a glass slide using crystalbond adhesive and polished using diamond lapping film of various particle sizes, finishing with a particle size of 3 μm. The other side of the sample was then polished following a similar procedure. The final thickness of each sample used for FTIR analyses was between 300 and 500 μm. After removing the samples from the glass slide on a hot plate, samples were immersed in acetone for at least 12 hours before FTIR measurements were carried out.

Samples were positioned with the [010] axis parallel to an unpolarized IR beam using a window size of 100 x 100 μm^2. Analyses were carried out on areas free of cracks and visible inclusions. The baseline was determined by using a spline fit to the absorption spectrum between wavenumbers of 4000 to 3800 and 2800 to 2000 cm^{-1}, regions of the IR spectrum that are away from the OH stretching bands. Hydrogen concentrations were calculated by numerical integration of the baseline-corrected spectra over the range of 3000 to 3650 cm^{-1} using an established hydrogen calibration (*Paterson*, 1982) modified with a correction factor of 3.5 (*Bell et al.*, 2003).

3.3.4 EBSD Analyses

Post-deformation EBSD analyses were used to characterize the development of low-angle boundaries, measure crystallographic misorientation in the crystals, and infer the dominant dislocation slip systems that operated during the experiments. EBSD maps were compiled from data collected from entire slices of deformed crystals by stitching together up to 50 individual maps using the HKL Channel 5 software. The step sizes used for collecting EBSD data were either 15 or 16 μm. The MTEX toolbox (*Bachmann et al.*, 2010) for Matlab was used to determine values of Schmid factor and positions of low-angle boundaries. Analyses of the distribution of orientations of low-angle boundaries were carried out using ImageJ software.

Mechanical data from experiments performed under hydrous conditions during this study and those performed under anhydrous conditions from previous studies were corrected for small variations in initial orientation using crystallographic orientations from EBSD analyses. The values of stress used in determining flow law parameters were calculated by multiplying the resolved shear stress on the (001)[100] slip system (equal to the resolved shear stress on the (100)[001] system) by a factor of two. This correction factor, which resulted in maximum deviation from the applied stress of 10%, ensured that the minor misalignments of the crystals that occurred during the cutting procedure when preparing the crystals for deformation did not contaminate the dataset.

3.4 Results

3.4.1 Results for Experiments at Hydrous Conditions

The results of deformation experiments carried out using brucite-buffered and talc-buffered samples are presented in Table 3.1. Experiments were conducted at 1050° to 1250°C, differential stresses between 41 and 306 MPa, and resultant strain rates between 1.5 x 10^{-6} and 4.4 x 10^{-4} s^{-1}. At low-stress ($\leq$100 MPa) and high-temperature conditions ($\geq$1200°C), strain rate follows a power-law dependence upon stress. At high-stress ($\geq$100 MPa) and low-temperature conditions ($\leq$1100°C) conditions, strain rate is more stress sensitive than at low-stress and high-temperature conditions, suggestive of an exponential dependence upon stress.

Table 3.1: Experimental Conditions and Creep Data

Exp. #	σ (MPa)	$\dot{\varepsilon}$ (s^{-1})	T (°C)	Buffer	ε
PI-1697*	-	-	1250	talc	-
PI-1615	100	2.3E-05	1200	talc	1.38
	122	6.2E-05	1200	talc	1.45
	150	1.2E-04	1200	talc	3.16
	204	2.3E-04	1200	talc	1.49
PI-1616	86	1.3E-05	1200	talc	4.26
	133	5.6E-05	1200	talc	2.98
	206	2.8E-04	1200	talc	2.87
	250	4.4E-04	1200	talc	6.41
PI-1618	52	4.5E-06	1200	brucite	0.74
	85	3.3E-05	1200	brucite	1.54
	133	3.3E-04	1200	brucite	2.74
PI-1622	45	3.2E-06	1200	brucite	1.20
	72	1.2E-05	1200	brucite	1.01

Continued on next page

Table 3.1 – *Continued from previous page*

Exp. #	σ (MPa)	$\dot{\varepsilon}$ (s^{-1})	T (°C)	Buffer	ε
	110	5.6E-05	1200	brucite	3.12
	142	1.2E-04	1200	brucite	1.75
	166	3.0E-04	1200	brucite	3.87
PI-1766a	64	3.3E-06	1250	talc	0.33
	87	9.6E-06	1250	talc	0.30
	109	2.6E-05	1250	talc	0.55
	75	6.1E-06	1250	talc	0.37
	97	1.7E-05	1250	talc	0.50
PI-1766b	132	2.7E-06	1150	talc	0.21
	160	7.0E-06	1150	talc	0.23
	188	1.6E-05	1150	talc	0.52
	138	4.9E-06	1150	talc	0.28
	167	9.3E-06	1150	talc	0.34
	194	1.9E-05	1150	talc	0.52
PI-1766c	232	1.5E-06	1050	talc	0.08
	262	2.7E-06	1050	talc	0.21
	294	3.6E-06	1050	talc	0.15
PI-1782a	82	8.1E-05	1250	talc	1.38
	99	1.5E-04	1250	talc	1.42
	63	3.4E-05	1250	talc	0.49
	83	7.7E-05	1250	talc	0.87
	42	1.6E-05	1250	talc	0.22
	67	3.1E-05	1250	talc	0.68
PI-1782b	93	6.8E-06	1150	talc	0.44
	133	2.2E-05	1150	talc	0.99

Continued on next page

Table 3.1 – *Continued from previous page*

Exp. #	σ (MPa)	$\dot{\varepsilon}$ (s^{-1})	T (°C)	Buffer	ε
	165	4.4E-05	1150	talc	1.23
	196	7.2E-05	1150	talc	1.63
	129	2.0E-05	1150	talc	0.61

*Experiment was stopped after hydration anneal.

3.4.2 Comparison to Results under Anhydrous Conditions

Published results from deformation experiments carried out on crystals of San Carlos olivine in the $[101]_c$ orientation under anhydrous conditions were used for determining flow law parameters for comparison to the data presented in Table 3.1. Data were obtained from deformation experiments performed at 900° to 1300°C, differential stresses between 87 and 487 MPa, and resultant strain rates between 2.0 x 10^{-6} and 1.8 x 10^{-4} s^{-1} (*Mackwell et al.*, 1985; *Schneider*, 2008; *Demouchy et al.*, 2009). The data from experiments carried out in iron capsules (*Mackwell et al.*, 1985) were normalized from oxygen fugacity conditions set by Fe/FeO to those set by the Ni/NiO buffer by using the oxygen fugacity dependence determined by previous studies (*Bai et al.*, 1991). This normalization results in an increase in strain rate by a factor of 1.8 at 1300°C. Mechanical data from crystals that had starting length to width ratios of less than two (*Schneider*, 2008) were omitted from the data fitting process. This omission ensured that deformation of all of the analyzed experiments occurred in a similar state of stress.

3.4.3 Determination of Flow Law Parameters

The total measured strain rate, $\dot{\varepsilon}_{\,\mathrm{total}}$, of crystals deformed under anhydrous and hydrous conditions were fit by minimizing the square of the residuals in a least squares sense for parameters in a combined flow law composed of two independent mechanisms

$$\dot{\varepsilon}_{\,\mathrm{total}} = \dot{\varepsilon}_{\,\mathrm{climb}} + \dot{\varepsilon}_{\,\mathrm{glide}}, \tag{3.15}$$

where $\dot{\varepsilon}_{\rm climb}$ and $\dot{\varepsilon}_{\rm glide}$ are Equations 3.8 and 3.12, respectfully. The large number of parameters in the exponential function required some to be held constant during the fitting procedure. Values of 0.5 and 2 were used for p, and q, respectively. These values were chosen based on analyses of previous experiments (*Demouchy et al.*, 2013).

Flow law parameters for anhydrous and hydrous conditions were determined by fitting the data obtained at high-temperature conditions using a power-law relationship (Eq. 3.8) and then fitting the entire dataset using the combined flow law (Eq. 3.15) with the power-law (Eq. 3.8) and exponential relationships (Eq. 3.12). For data from anhydrous experiments, A_c, n, and Q_c were determined by fitting data collected at 1200° and 1300°C using Equation 3.8. The values of A_g, Q_g, and σ_g were then determined by performing a least-squares fit to the entire dataset using Equation 3.15.

For data from hydrous experiments, values for $A_{\rm c}$, n, and $Q_{\rm c}$ were determined using the data from experiments conducted at 1150°, 1200°, and 1250°C. The data determined from experiments at 1050°C under hydrous conditions are in very good agreement with the strain rate predicted by Equation 3.12 using values of $A_{\rm g}$, $Q_{\rm g}$, and σ_g determined under anhydrous conditions. That is, no hydrolytic weakening was detected at 1050°C for our experimental conditions.

Our findings can be summarized with the following flow laws combined to yield constitutive equations for anhydrous and hydrous conditions of the form expressed in Equation 3.15. The power-law relationship determined from experiments under anhydrous conditions is

$$\dot{\varepsilon}^{\rm dry}_{\rm climb} = 10^{4\pm2}\sigma^{3.5\pm0.3}\exp\left(\frac{-470\pm62\,{\rm kJ/mol}}{{\rm R}T}\right){\rm s}^{-1}, \tag{3.16}$$

for σ in MPa. The power-law relationship determined from experiments conducted under hydrous conditions is

$$\dot{\varepsilon}^{\rm wet}_{\rm climb} = 10^{7.5\pm0.9}\sigma^{2.5\pm0.1}\exp\left(\frac{-480\pm27\,{\rm kJ/mol}}{{\rm R}T}\right){\rm s}^{-1}. \tag{3.17}$$

The exponential law under both anhydrous and hydrous conditions is

$$\dot{\varepsilon}_{\text{glide}}^{\text{dry,wet}} = 10^{0.9\pm1.4}\sigma^{1.4}\exp\left[\left(\frac{-421 \pm 63\ \text{kJ/mol}}{\text{R}T}\right)\left(1-\left(\frac{\sigma}{5.8 \pm 0.7\ \text{GPa}}\right)^{0.5}\right)^{2}\right] \text{s}^{-1}. \tag{3.18}$$

The results of the least-squares fit are in good agreement with experimentally determined values of strain rate and stress as presented in Figures 3.2 and 3.3.

3.4.4 Dependence of Strain Rate on Orthopyroxene Activity

The influence of a_{opx} on the strain rate of olivine single crystals under hydrous conditions is apparent from the mechanical data for brucite-buffered samples and talc-buffered samples in Figure 3.4. At these conditions the dehydration of brucite to periclase results in a a_{opx} of $\sim$ 0.12 based on a value of -25.7 kJ/mol for the Gibbs free energy of formation of iron-bearing olivine from mixed oxides at 1200°C (*Hobbs*, 1983) whereas the talc-buffered samples are fixed at a_{opx} of $\sim$ 1. At the same stress, the strain rate of brucite-buffered crystals is approximately a factor of three times faster than talc-buffered samples. This observation can be generalized to

$$\dot{\varepsilon} \propto a_{\text{opx}}^{v}, \tag{3.19}$$

where v describes the sensitivity of the strain rate to a_{opx}. A least-squares fit of strain rates as a function of a_{opx} for talc-buffered and brucite-buffered data at 1200°C yields $v \approx$ -0.5, compared to a value of 1.2 determined for olivine crystals deformed under anhydrous conditions (*Ricoult and Kohlstedt*, 1985a).

3.4.5 Results from FTIR Analyses

The FTIR spectra presented in Figure 3.5 demonstrate that a significant amount of hydrogen was incorporated into the olivine lattice during talc-buffered experiments. Spectra from the starting material (natural San Carlos olivine) reveal no absorption peaks over the range of wavenumbers that are associated with OH stretching. The talc-buffered crystal from the experiment that was

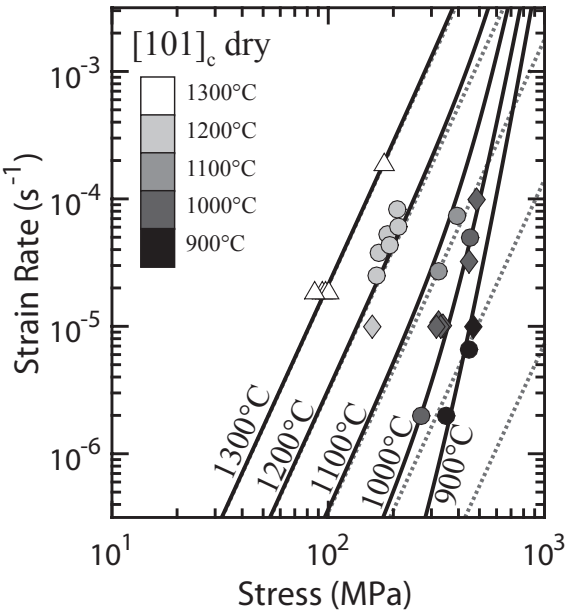

Figure 3.2: Strain rate as a function of stress for single crystals deformed under anhydrous conditions. The solid lines are a combination of the power and exponential laws (Equations 3.16 + 3.18) and the dotted lines are the power law alone (Equation 3.16). At high-temperatures, the data are well described by the power-law relationship, whereas at lower temperatures the data are weaker than predicted from the power-law. Triangles are from *Mackwell et al.* (1985), circles are from *Schneider* (2008), and diamonds are from *Demouchy et al.* (2009).

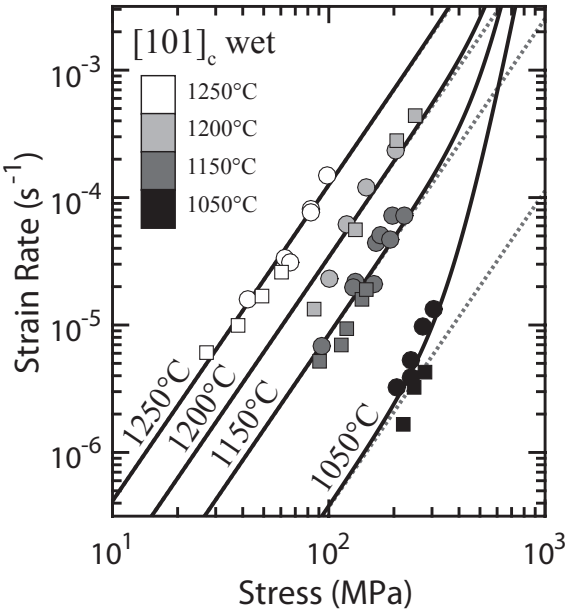

Figure 3.3: Strain rate as a function of stress for single crystals deformed under hydrous conditions. The solid lines are a combination of the power and exponential laws (Equations 3.17 + 3.18) and the dotted lines are the power law alone (Equation 3.17). At high-temperatures, the data are well described by the power-law relationship, whereas at lower temperatures and higher stress conditions, the data are weaker than predicted from the power-law. Circles and squares are used to differentiate different experiments when more than one experiment was performed at a given temperature.

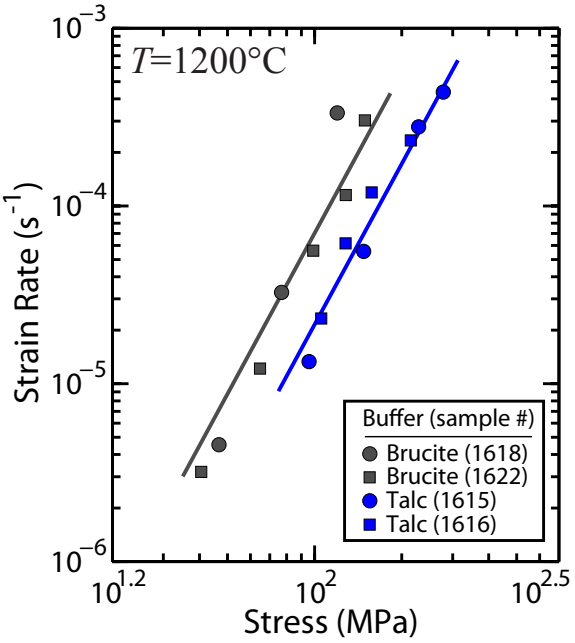

Figure 3.4: Stress versus strain rate for crystals deformed in the $[101]_c$ orientation at 1200°C in different chemical environments. Red data points are for orthopyroxene-buffered samples from *Schneider* (2008), blue data points are for talc-buffered samples, and grey data points are for brucite-buffered samples. The lines are least-square fits for each buffer using a power-law relationship with a stress exponent of 3. For a given stress, $\dot{\varepsilon}_{\mathrm{talc-buffered}} \approx 3\,\dot{\varepsilon}_{\mathrm{orthopyroxene-buffered}}$ and $\dot{\varepsilon}_{\mathrm{brucite-buffered}} \approx 3\,\dot{\varepsilon}_{\mathrm{talc-buffered}}$.

stopped after a hydration anneal at 1250°C contains 190 ppm H/Si whereas post-deformation analyses yield hydrogen contents of 260 ppm H/Si and 210 ppm H/Si after deformation of talc-buffered crystals at 1200° and 1050°C, respectively.

The FTIR spectra for talc-buffered samples reveal variation in peak height but not peak position among the samples. The dominant peak positions are at wavenumbers of 3573, 3526, 3357, 3328, and 3229 cm^{-1}. The height of absorption peaks at wavenumbers 3573 and 3526 cm^{-1}, corresponding to Group I IR bands (*Bai and Kohlstedt*, 1993), increase with increasing temperature for deformed samples. In contrast, the heights of peaks at wavenumbers 3357, 3328, and 3229 cm^{-1}, corresponding to Group II IR bands, are similar at different temperatures.

Post-deformation FTIR spectra of brucite-buffered samples yield hydrogen contents similar to those from talc-buffered samples. However, some of the Group II IR bands observed in talc-buffered samples are not observed in brucite-buffered samples. Specifically, the small peaks at 3357 and 3329 cm^{-1} are absent in brucite-buffered samples, as demonstrated in the FTIR spectra in Figure 3.6.

3.4.6 Results from EBSD Analyses

EBSD analyses of deformed samples reveal the development of intracrystalline misorientation and low-angle boundaries. Rotational axes parallel or subparallel to the [010] axes are dominant in samples deformed at both anhydrous and hydrous conditions, as presented in Figure 3.7. The strength of the concentration of rotational axes about the [010] axis is strongest at 1050°C under hydrous conditions and weakest at 1000°C under anhydrous conditions, where a slight preference in the direction of the [100] axis becomes apparent.

Straight low-angle boundaries are present in the deformed samples, as presented in Figure 3.8. In experiments under hydrous conditions, in the power-law creep regime, low-angle boundaries align preferentially in the (100) planes with a smaller population oriented parallel to the (001) planes. In contrast, in experiments under anhydrous conditions, in the exponential creep regime, low-angle boundaries preferentially align in the (001) planes with an additional population aligning with the (100) planes.

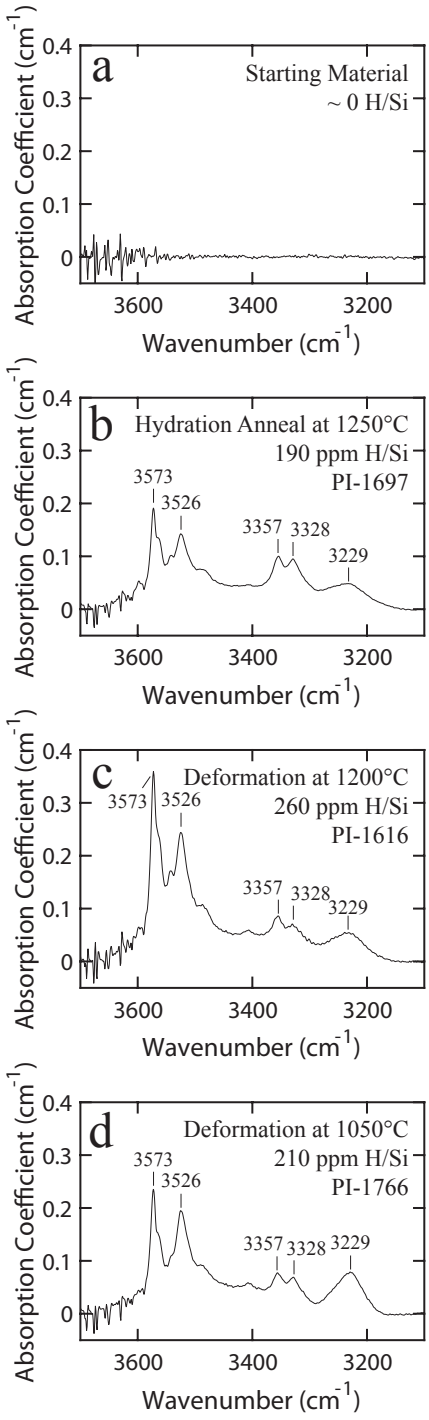

Figure 3.5: Unpolarized FTIR spectra taken with the IR bean parallel to [010] for (a) a natural crystal of San Carlos olivine, (b) a crystal hydrothermally annealed at 1250°C, (c) a crystal hydrothermally annealed at 1250°C and then deformed at 1200°C, and (d) a crystal hydrothermally annealed at 1250°C and then deformed at 1050°C. The spectra in b, c, and d were from experiments on talc-buffered crystals.

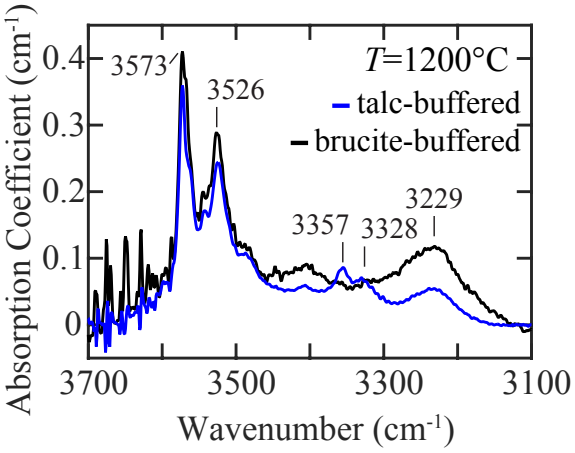

Figure 3.6: FTIR spectra taken parallel to IR beam parallel to [010] for crystals annealed and deformed in the presence of talc (blue) or brucite (black). The magnitude and positions of peaks are similar except that the brucite-buffered sample lacks the minor peaks between 3300 and 3400 cm^{-1} that are present in spectra from the talc-buffered sample.

An analysis of the distributions of low-angle boundaries determined using the fast multiscale clustering method in MTEX toolbox is presented in Figure 3.9. For the crystal deformed in the power-law creep regime, the normalized concentration of low-angle boundaries parallel to the (100) plane is >3 times larger than that predicted for a uniform distribution. In contrast, for the crystal deformed in the exponential creep regime, the normalized concentration of low-angle boundaries parallel to the (001) plane is >3 times larger than that predicted for a uniform distribution.

3.5 Discussion

3.5.1 Deformation in the Climb-Controlled Regime

The flow laws presented in Equations 3.16 and 3.17 are consistent with deformation occurring by climb-controlled dislocation creep at high-temperature conditions. In experiments conducted under anhydrous conditions and at high a_{opx}, results of the least-squares fit in Equation 3.16 yield a value of n of $\sim$3.5. This value of n is consistent with deformation that is rate limited by

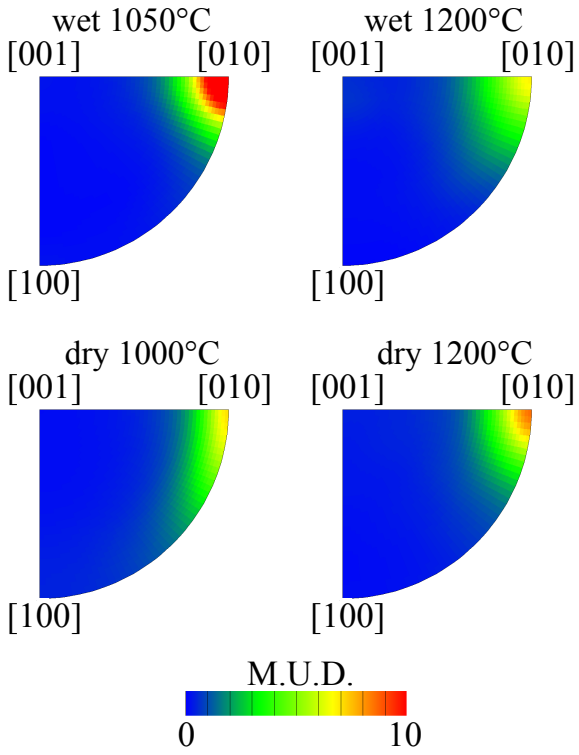

Figure 3.7: Inverse pole figures of misorienation axes in the crystallographic coordinate system. Rotational axes are for misorientations between 1 to 10 degrees for neighboring pixels from orientation maps of deformed samples. The scale for multiples of uniform distribution is presented on the bottom of the figure. The concentration around the [010] axis and are consistent with deformation occurring primarily by dislocations on the (001)[100] and (100)[001] slip systems.

the climb of dislocations, with the climb velocity controlled by diffusion of the slowest species through the cores of dislocations (*Hirth and Kohlstedt*, 2015). In experiments conducted under hydrous conditions, at high a_{opx}, and at high temperatures, results of the least-squares fit in Equation 3.17 yield a value of the n of $\sim$2.5. This value of n is compatible with deformation occurring in a climb-controlled regime, with the climb velocity controlled by diffusion of the slowest species through the lattice (*Hirth and Kohlstedt*, 2015).

A similar hydrogen-induced transition in the value of n is apparent by comparing previous work on both single crystal and polycrystalline olivine. For single crystals, a value for n of $\sim$3.5 was determined under anhydrous conditions (*Durham and Goetze*, 1977; *Ricoult and Kohlstedt*,

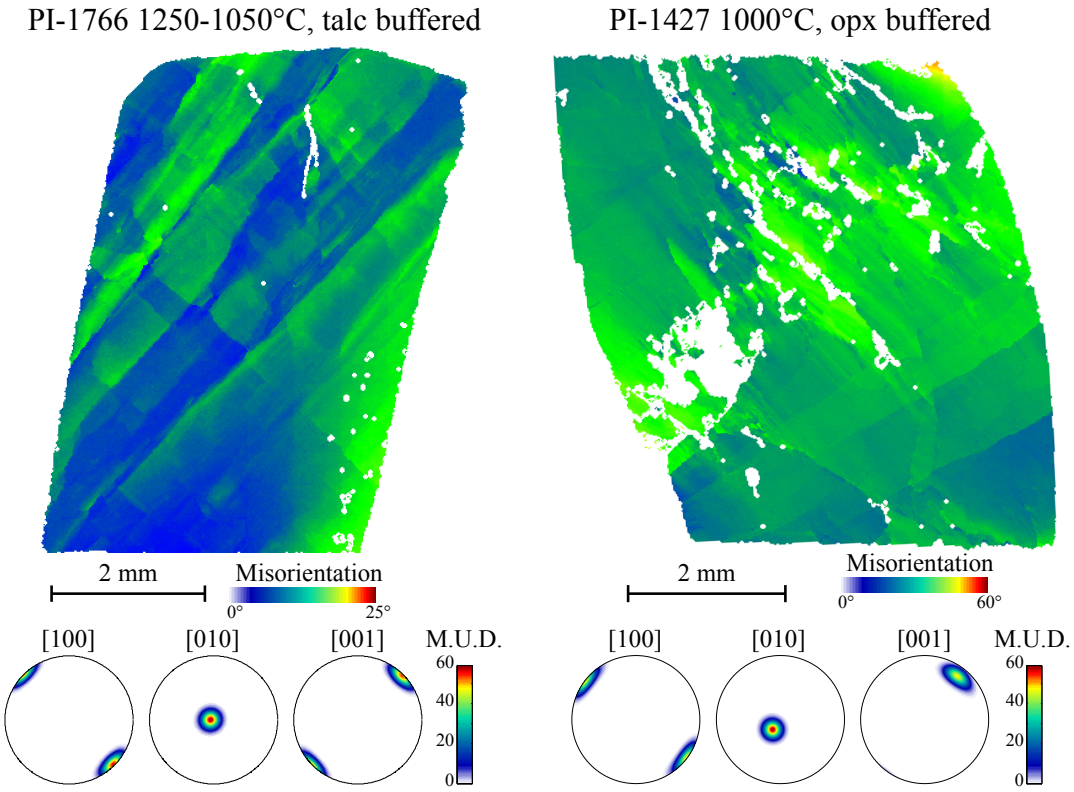

Figure 3.8: Maps of misorientation and pole figures with orientations for samples PI-1766 (left) and PI-1427 (right). The value of misorientation in each map is relative to the orientation at center of the crystal along the boundary with the adjacent alumina piston. Pole figures are equal area and lower hemisphere projections with corresponding scale of multiples of uniform distribution on the right. The development of crystallographically controlled low-angle boundaries is apparent in the misorientaiton maps and is consistent with deformation occurring by the motion of dislocations.

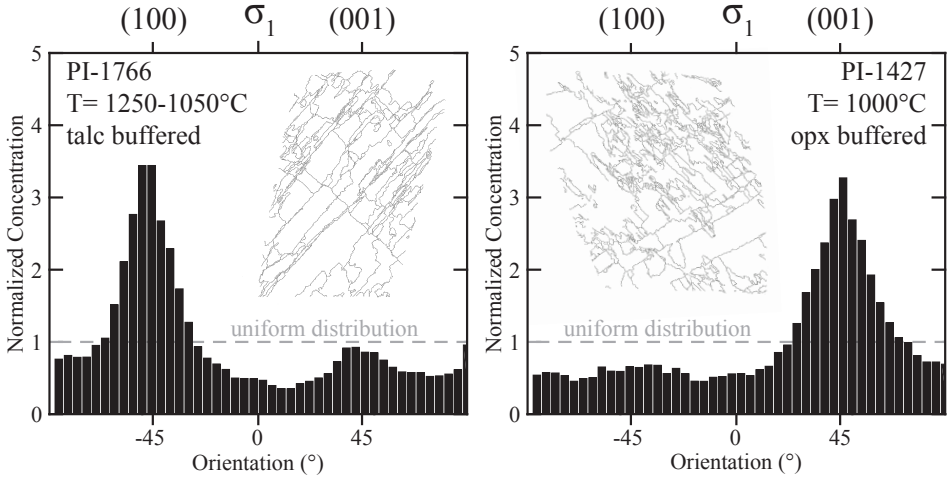

Figure 3.9: Histograms of the normalized concentration of the orientations of low-angle boundaries for samples PI-1766 (left) and PI-1427 (right). The differences in preferred orientation of low-angle boundaries in the two samples may suggest different populations of dislocation types operate at the different experimental conditions.

1985b; *Bai et al.*, 1991), whereas a value of ∼2.5 was determined under hydrous conditions (*Mackwell et al.*, 1985). For experimentally deformed natural dunite, a value of n of ∼4.8 was obtained when deformation occurred in the absence of water, whereas a value of of ∼2.4 was determined when deformation occurred in the presence of water (*Carter and Ave'Lallemant*, 1970). For fine-grained olivine aggregates, a value of n of ∼3.5 was obtained under anhydrous conditions, whereas a value of ∼3.0 was determined under hydrous conditions (*Karato et al.*, 1986).

A hydrogen-induced transition in the value of value of n was not determined in some previous work on hydrolytic weakening in olivine. A value of n of ∼3.6 was determined for both dry Anita Bay and dry Åheim dunite, whereas wet Anita Bay dunite yielded a value of ∼3.4 and wet Åheim dunite yielded a value of ∼4.5 (*Chopra and Paterson*, 1984). The lack of a systematic hydrogen-induced transition in the value of n obtained from Anita Bay and Åheim dunite may possibly be attributed to the presence of additional phases, including possibly melt (*Hirth and Kohlstedt*, 1996), in the starting material. Fine-grained olivine aggregates revealed a value of n of ∼3 at both wet and dry conditions (*Mei and Kohlstedt*, 2000b). However, these

data were obtained from samples that were deformed near the transition from diffusion creep to dislocation creep, which increases the difficulty of obtaining precise values of n for the two mechanisms.

The differences in strain rate at fixed temperature and stress between brucite-buffered and talc-buffered samples in Figure 3.4 are consistent with deformation occurring in the climb-controlled dislocation creep regime that is governed by diffusion of silicon through the crystal lattice. Diffusion of silicon through the olivine crystal lattice is controlled by both $f_{\mathrm{H_2O}}$ and the a_{opx}. Under hydrous conditions (i.e., talc-buffered or brucite-buffered experiments), hydrogen ions are introduced into olivine which act to increase $X_{\mathrm{V_{Si}}}$. The different orthopyroxene buffers also influence $X_{\mathrm{V_{Si}}}$ where brucite, dehydrated into periclase, acts to suppress vacancies associated with metal sites and talc, dehydrated into orthopyroxene, acts to suppress vacancies associated with silicon sites.

The creep data presented in Figures 3.2 and 3.3 can be used to evaluate the model of climb-controlled dislocation creep. The rate of climb predicted by Equation 3.4 using the silicon self-diffusion coefficient for olivine under anhydrous conditions (*Dohmen et al.*, 2002) demonstrate that a ratio of the length of glide to the length of climb, l_g/l_c, of 10^4 is required to match the strain rates determined from Equation 3.16. However, values of l_g/l_c are unlikely to exceed $\sim$100 for typical experimental conditions (*Hirth and Kohlstedt*, 2015). In addition, the time required to diffuse a silicon ion one unit cell using this value of silicon self-diffusion coefficient is $\sim$2.5 hours, revealing that deformation rates would be exceedingly slow for these conditions if deformation occurs in a climb-controlled regime that is controlled by lattice diffusion (*Kohlstedt*, 2007; *Hirth and Kohlstedt*, 2015). These observations strongly suggest that the strain rate of anhydrous olivine crystals deforming at high temperatures cannot be rate limited by diffusion of silicon through the olivine lattice.

In contrast, measured values of silicon diffusivity in olivine under hydrous conditions, when combined with Equation 3.4, are consistent with the experimental observations presented in Figure 3.3. Using the silicon self-diffusion coefficient for olivine obtained under hydrous conditions (*Costa and Chakraborty*, 2008) for $f_{\mathrm{H_2O}} \approx 300$ MPa, values of l_g/l_c required to match

the strain rate in Equation 3.17 range from 90 to 150 for values of the f_{H_2O} exponent for silicon self-diffusion (r) ranging from 0.5 to 1.0. These values of l_g/l_c and are on the same order of magnitude, and therefore compatible with, dislocation creep that is rate limited by diffusion of silicon through the olivine lattice (*Hirth and Kohlstedt*, 2015). Furthermore, the calculated time required to climb one unit cell is reduced to 4 to 7 seconds using the same values of r. These times are compatible with climb that is limited by lattice diffusion occurring during the duration of a deformation experiment. We also note that additional data are available for silicon diffusion for iron-free olivine (*Fei et al.*, 2012, 2013), but a direct application of these data to deformation of iron-bearing olivine is not appropriate due to the importance of iron on the concentration of point defects in olivine (e.g., *Nakamura and Schmalzried*, 1983).

3.5.2 Deformation in the Glide-Controlled Regime

At temperatures $\leq$1100°C and stresses $\geq$100 MPa, the mechanical data presented in Figures 3.3 and 3.2 are weaker than predicted by the climb-controlled relationship, suggesting deformation occurring in the glide-controlled dislocation creep regime. Importantly, Equation 3.18 fits the data from both anhydrous and hydrous experiments performed at low-temperature, and high-stress conditions. Although hydrolytic weakening is observed in the climb-controlled regime, it is not observed in the glide-controlled regime for the experimental conditions of this study.

However, results from experiments performed on olivine aggregates at conditions of higher f_{H_2O} demonstrate that hydrolytic weakening occurs in the glide-controlled regime. A lower value of Peierls stress was determined for olivine deformed under hydrous conditions compared to anhydrous conditions (*Katayama and Karato*, 2008). The discrepancy between that observation and the data presented in Table 3.1 and Figures 3.3 and 3.2 are likely the result of the higher f_{H_2O} conditions ($\sim$ 12 GPa) resulting from the higher pressure conditions ($\sim$ 2 GPa) used in the *Katayama and Karato* (2008) study. Therefore, it is likely that conditions of higher f_{H_2O} are needed in order to achieve significant hydrolytic weakening in the glide controlled dislocation creep regime. A similar conclusion was reached from analysis of data from experimentally deformed quartz single crystals, where it was reported that a minimum of 100 ppm

H/Si is needed to weaken quartz single crystals at 1070°C, whereas 9000 ppm H/Si is needed at 380°C (*Griggs and Blacic*, 1964).

3.5.3 Microstructural Observations

Deformation of olivine in the climb-controlled regime involves simultaneous operation of multiple dislocation slip systems. At high-temperature, low-stress conditions in the climb-controlled regime, deformation occurs primarily by the motion of dislocations on the (010)[100], (001)[100], (100)[001], and (010)[001] slip systems with possible additional activation of the (0kl)[001] and (110)[001] systems (*Durham and Goetze*, 1977; *Durham et al.*, 1977). The $[101]_c$ orientation used in this study produces no resolved shear stress on dislocation slip systems that involve glide on the (010) plane, so that the contribution of the (010)[100] and (010)[001] slip systems to the strain rate is negligible. The observed rotations about the [010] axis presented in Figure 3.7 are consistent with the formation of low-angle boundaries due to operation of the (001)[100] and (100)[001] slip systems, with minor contribution from other slip systems likely gliding on the (0kl) or (110) planes. However, the relative contribution of individual slips systems to the strain in the sample cannot be inferred from Figure 3.7.

The relative contribution of the (001)[100] and (100)[001] slip systems may be inferred form the rotation of the crystals in Figure 3.8. During dislocation creep of single crystals, the crystallographic plane on which most of the dislocations responsible for deformation in single crystals operate rotates so that its crystallographic axis becomes more parallel with the direction of the applied stress (*Durham and Goetze*, 1977). At conditions of high temperature and low stress, consistent with deformation in the climb-controlled regime, the crystal rotates so that the [001] axis rotates towards the direction of applied stress. Whereas, at conditions of low temperature and high stress, consistent with deformation in the glide-controlled regime, the crystal rotates so that the [100] axis rotates towards the direction of applied stress. These observations are congruous with the dominance of the (001)[100] slip system in the climb-controlled regime and the (100)[001] slip system in the glide-controlled regime.

The results presented in Figure 3.9 give more insight into the identity of the dominant slip

system at different conditions. The preferred orientation of low angle boundaries in the (100) plane in a sample deformed in the presence of talc at 1250°, 1150°, and 1050°C is consistent with the dominance of [100] Burgers vectors during climb-controlled dislocation creep under hydrous conditions. In contrast, in a sample deformed at 1000°C and under anhydrous conditions, low angle boundaries preferentially align in the (001) plane, consistent with deformation that is dominated by glide of edge dislocations with [001] Burgers vectors.

3.5.4 Scaling to Mantle Conditions

Scaling of these results to upper mantle conditions requires extrapolation over significant ranges of stress, temperature, and hydrogen concentration. Importantly, hydrogen contents in our samples are ∼200 ppm H/Si, considerably less than the 1000 to 3000 ppm H/Si predicted to be present in the upper mantle (*Hirschmann*, 2006). Therefore, the results presented above are a lower-bound for hydrolytic weakening in olivine single crystals at upper mantle conditions. Using the constitutive relationships presented in Equations 3.16, 3.17, and 3.18, it is possible to scale to lower stress conditions as presented in Figure 3.10. For a typical laboratory stress of 200 MPa, the flow laws yield a hydrolytic weakening factor ($\dot{\varepsilon}_{\mathrm{wet}}/\dot{\varepsilon}_{\mathrm{dry}}$) of ∼1 at 600°C, which increases to ∼10 at 1400°C. In contrast, for a typical lithospheric stress of 20 MPa, the hydrolytic weakening factor increases from ∼1 at 900°C to ∼50 at 1400°C. These results demonstrate that a small amount of structurally incorporated hydrogen results in significant weakening of olivine at asthenospheric mantle conditions.

3.6 Conclusions

Hydrolytic weakening is observed in samples deformed at high-temperature conditions and results in lower values of n compared to crystals deformed under anhydrous conditions. These observations are consistent with dislocation motion that is rate limited by pipe diffusion under anhydrous conditions and by lattice diffusion under hydrous conditions. Hydrolytic weakening is not observed at low-temperature and high-stress conditions in the glide-controlled dislocation

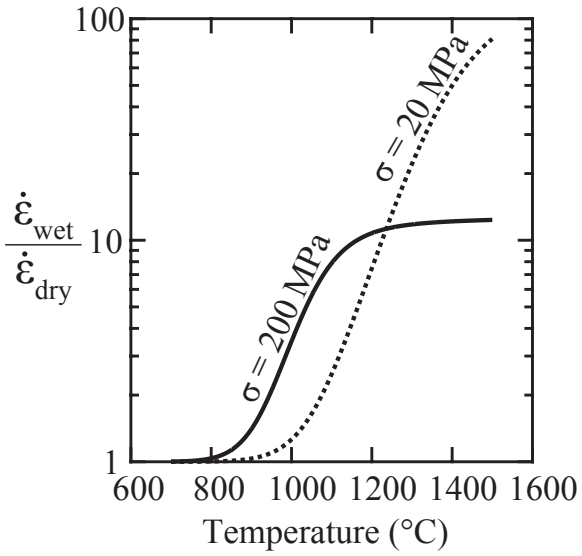

Figure 3.10: Plot of the ratio of strain rates predicted using Equation 3.15 with the flow law parameters for wet (hydrous) or dry (anhydrous) deformation from Equations 3.16, 3.17, and 3.18. The black line represents a typical laboratory stress of 200 MPa and the dotted line represents a typical lithospheric stress of 20 MPa. The larger ratio of strain rates predicted under lithospheric stress conditions is a result of the different values of stress exponent, which reflect the different microphyical processes operating for olivine under hydrous and anhydrous conditions at high temperature. At lower temperatures, hydrolytic weakening is less pronounced because the exponential function in Equation 3.18 describes both hydrous and anhydrous samples equally well.

creep regime for our experimental conditions. Extrapolation of the flow laws derived from data in this study to conditions of stress and temperature of upper mantle conditions demonstrates significant hydrolytic weakening occurs in olivine single crystals.

Chapter 4

Observations of grain-size sensitive power-law creep of olivine aggregates over a large range of lattice-preferred orientation strength

This chapter is under review for publication in the Journal of Geophysical Research, with co-authors Lars Hansen, Miki Tasaka, Cameron Meyers, Mark Zimmerman, and David L. Kohlstedt.

Grain-size sensitive (GSS) power-law creep of San Carlos olivine aggregates was investigated by comparing strain rates measured in laboratory deformation experiments to strain rates determined from a micromechanical model of intragranular dislocation processes. The plastic flow behavior of olivine aggregates due solely to intragranular slip was determined using flow laws for olivine single crystals in combination with grain orientations measured by electron-backscatter diffraction. Measured strain rates were compared to results from the micromechanical model for samples deformed in compression to an axial strain of <0.2 and in torsion to a shear strain of up to 7.4. Olivine aggregates deform up to a factor of 4.6 times faster than

the maximum possible rates determined from the micromechanical model of intragranular slip. Comparison of our data to published flow laws indicates that diffusion creep cannot account for this difference. The ratio of experimentally determined strain rates to those from the micromechanical model is strongly dependent upon grain size, but is independent of stress and strength of lattice-preferred orientation. These observations indicate that GSS power-law creep, consistent with dislocation-accommodated grain-boundary sliding, occurs in both weakly and strongly textured olivine aggregates at the studied conditions.

4.1 Introduction

Geodynamic simulations of solid-state flow in the upper mantle require flow laws derived from experimental deformation of olivine-rich rocks. These flow laws define rheological regimes, which describe conditions at which the mechanical behavior of materials behave in a defined manner. An important aspect of experimental deformation is relating flow laws to deformation mechanisms that describe the atomistic process that give rise to flow (*Frost and Ashby*, 1982). Multiple deformation mechanisms may operate simultaneously during high-temperature deformation. The relative influence of each mechanism depends upon state variables including grain size, stress, and strength of lattice-preferred orientation (LPO) (*Evans*, 2005), each of which may vary significantly between laboratory and upper-mantle conditions. It is therefore possible that the dominant deformation mechanism at laboratory conditions is not the dominant mechanism under mantle conditions, a situation that would result in significant error in geodynamic simulations. To evaluate the contributions of different deformation mechanisms operating during polycrystalline deformation, we compared strain rates measured in deformation experiments on olivine aggregates to strain rates determined from a micromechanical model.

The micromechanical model used in this paper allows for isolation of the contribution of the motion of lattice dislocations, a grain size insensitive (GSI) process, to the total strain rate of an aggregate. This step is carried out by combining crystallographic orientation data from

deformation experiments on olivine aggregates with flow laws for individual slip systems obtained from high-temperature creep experiments on olivine single crystals. We compare strain rates determined from the micromechanical model to strain rates measured from experimentally deformed samples to quantify the influence of grain-size sensitive (GSS) processes. These data are then used to identify the dominant deformation mechanism that is operating at different conditions of grain size, stress, and strength of LPO.

Multiple rheological regimes have been identified during high-temperature steady-state deformation of olivine aggregates. These regimes include GSS linear creep, GSS power-law creep, and GSI power-law creep. The steady-state rheological behavior of olivine aggregates under high-temperature conditions is well described by flow laws of the form

$$\dot{\varepsilon} = A\frac{\sigma^n}{d^p} f_{\mathrm{O_2}}^m f_{\mathrm{H_2O}}^r \exp\left(\frac{-Q}{\mathrm{R}T}\right), \tag{4.1}$$

where $\dot{\varepsilon}$ is strain rate, A is a material specific parameter, σ is differential stress, n is the stress exponent, d is grain size, p is the grain size exponent, $f_{\mathrm{O_2}}$ is oxygen fugacity, m is the oxygen fugacity exponent, $f_{\mathrm{H_2O}}$ is water fugacity, r is the water fugacity exponent, Q is activation enthalpy, R is the gas constant, and T is temperature. If the rheological regimes represent deformation mechanisms that operate independently of one another, the total strain rate for a viscously deforming aggregate, $\dot{\varepsilon}_{\mathrm{total}}$, can be expressed as a constitutive equation of the form

$$\dot{\varepsilon}_{\mathrm{total}} = \dot{\varepsilon}_{\mathrm{GSS\text{-}linear}} + \dot{\varepsilon}_{\mathrm{GSS\text{-}power}} + \dot{\varepsilon}_{\mathrm{GSI\text{-}power}}, \tag{4.2}$$

where the subscripts GSS-linear, GSS-power, and GSI-power refer to the strain rates from GSS linear creep, GSS power-law creep, and GSI power-law regimes, respectively.

The flow law parameters that define individual rheological regimes of a plastically deforming olivine aggregate may be used to infer the dominant, or rate-controlling, deformation mechanism operating in each regime. During GSS linear creep, n equals 1 and p equals 2 or 3, and deformation occurs by a diffusion mechanism (*Nabarro*, 1948; *Herring*, 1950; *Coble*, 1963). GSS power-law creep occurs when n is greater than 1 and p is greater than 0, and indicates

deformation occurs by a mechanism that involves the motion of lattice dislocations aided by deformation associated with the migration of and displacement along grain boundaries (*Langdon*, 1994). GSI power-law creep occurs when values of n are 3 to 4 and values of p are 0 and indicates that dislocation creep is dominant (*Poirier*, 1985, p. 103-109). The dominant deformation mechanisms operating during GSS linear creep and GSI power-law creep are well agreed upon. However, the deformation mechanism operating during the GSS power-law regime of olivine aggregates has been attributed to dislocation-accommodated grain boundary sliding (disGBS) (*Hirth and Kohlstedt*, 2003; *Drury*, 2005; *Hansen et al.*, 2011, 2012) or dynamic recrystallization-controlled (DRX) dislocation creep (*Platt and Behr*, 2011; *Johanesen and Platt*, 2015).

The dominant deformation mechanism may also be inferred from microstructural observations of deformed rocks. Typically, a strong LPO is interpreted as evidence of dislocation creep, while a weak LPO or nearly random orientation distribution is interpreted as evidence of diffusion creep (e.g., *Warren and Hirth*, 2006; *Mehl and Hirth*, 2008; *Toy et al.*, 2010). However, determination of the dominant deformation mechanism based on microstructural observations is not always straightforward. In olivine aggregates that were experimentally deformed in GSS linear and GSS power law regimes, LPOs of various strength have been observed. For example, a LPO has been observed in very fine-grained olivine aggregates deformed at low differential stress with n close to 1, suggesting fabric development may occur when diffusion creep is the dominant deformation mechanism (*Miyazaki et al.*, 2013; *Sundberg and Cooper*, 2008). Similarly, a LPO has been observed in olivine aggregates in which n is approximately 3 and p equals 0.7 (*Hansen et al.*, 2011), indicating that a LPO develops during GSS power-law creep.

In naturally deformed mantle rocks interpreted to have deformed by both GSS linear and GSS power-law creep, a LPO has also been observed. Lherzolite deformed at lithospheric mantle conditions displays a weak olivine LPO at conditions of stress and grain size near the transition from GSS linear to GSS power-law creep (*Drury et al.*, 2011). Peridotite deformed at conditions consistent with GSS power-law creep develops an LPO whose strength and orientation correlates with grain size (*Précigout and Hirth*, 2014). Numerical simulations indicate

that mantle materials retain a preexisting LPO after deformation via GSS linear creep (*Wheeler*, 2009), further complicating the interpretation of observations of LPO in the field.

These observations highlight the need for a method, in addition to experimentally determined flow law parameters and observation of microstructure, to infer the activity of individual deformation mechanisms in deformed rocks. In this paper, results from a micromechanical model are compared to measurements of strain rate from experimentally deformed olivine aggregates to investigate the operation of GSS power-law creep as a function of grain size, stress, and LPO strength. This process provides an additional tool to investigate the nature of the deformation mechanism that operates during GSS power-law creep of olivine aggregates.

4.2 Methods

Mechanical and crystallographic orientation data from experiments on olivine aggregates deformed in triaxial compression, direct shear (samples sheared between pistons cut at 45° to the compression direction), or torsion were utilized for the micromechanical model. The starting material for all experiments consisted of dried powders of San Carlos olivine that were uniaxially cold pressed at 100 MPa pressure and room temperature and then isostatically hot pressed at 300 MPa and 1200° or 1250°C. During the hot press and deformation portion of the experiments, the samples were surrounded by a nickel sleeve to control oxygen fugacity at the Ni/NiO buffer.

Values of grain size were determined from EBSD analyses of deformed samples using the MTEX toolbox for MATLAB® (*Bachmann et al.*, 2010). Examples of typical EBSD maps used to quantify grain size and LPO are presented in Figure 4.1. Step sizes used for EBSD mapping were between 0.25 and 1.0 μm and a critical misorientation angle of 10° was used to separate grains. Clusters of less than 5 pixels were omitted from calculations of grain size values for each sample. The mean grain size for each sample was determined by taking the arithmetic mean of the equivalent diameter of the grains calculated from the area. Values of grain size for each sample are well fit by a log-normal distribution. The mean value was then

multiplied by a factor of 1.5 to correct for artifacts introduced by the non-spherical nature of olivine grains as described by *Underwood* (1970, p. 80-93).

The steady-state values of stress and strain rate at the last segment of deformation of each experiment were used in the micromechanical model. Therefore, measurements of crystallographic fabric and grain size directly correspond with the mechanical data. A uniform stress condition is assumed such that the strain rate of each grain is calculated from the orientation of the dislocation slip systems with respect to the applied stress. The strain rate from dislocation creep for each grain in a deformed aggregate is estimated using published single crystal flow laws combined with the crystallographic orientation of the grain determined from EBSD. The stress tensor in the sample reference frame for triaxial compression, $\boldsymbol{\sigma}_{\mathrm{t}}$, is

$$\boldsymbol{\sigma}_{\mathrm{t}} = \begin{bmatrix} \sigma_{\mathrm{A}} + P & 0 & 0 \\ 0 & P & 0 \\ 0 & 0 & P \end{bmatrix} \tag{4.3}$$

and the stress tensor in the sample reference frame for torsion or direct shear experiments, $\boldsymbol{\sigma}_{\mathrm{s}}$, is

$$\boldsymbol{\sigma}_{\mathrm{s}} = \begin{bmatrix} P & \sigma_{\mathrm{A}} & 0 \\ \sigma_{\mathrm{A}} & P & 0 \\ 0 & 0 & P \end{bmatrix}, \tag{4.4}$$

where σ_A is the applied stress and P is the confining pressure. Either stress tensor can then be rotated into the crystallographic reference frame, as indicated by the prime symbol, by $\boldsymbol{\sigma}' = \mathbf{R}^T \boldsymbol{\sigma}\, \mathbf{R}$, where $\mathbf{R}$ is the rotation matrix defining the orientation of the crystal reference frame relative to the sample reference frame.

The symmetric glide tensor, $\boldsymbol{\mu}^{\alpha}$, for each slip system ($\alpha$) is determined from the relation (*Lebensohn and Tomé*, 1993)

$$\boldsymbol{\mu}^{\alpha} = \frac{1}{2}\left(b_i^{\alpha} n_j^{\alpha} + b_j^{\alpha} n_i^{\alpha}\right), \tag{4.5}$$

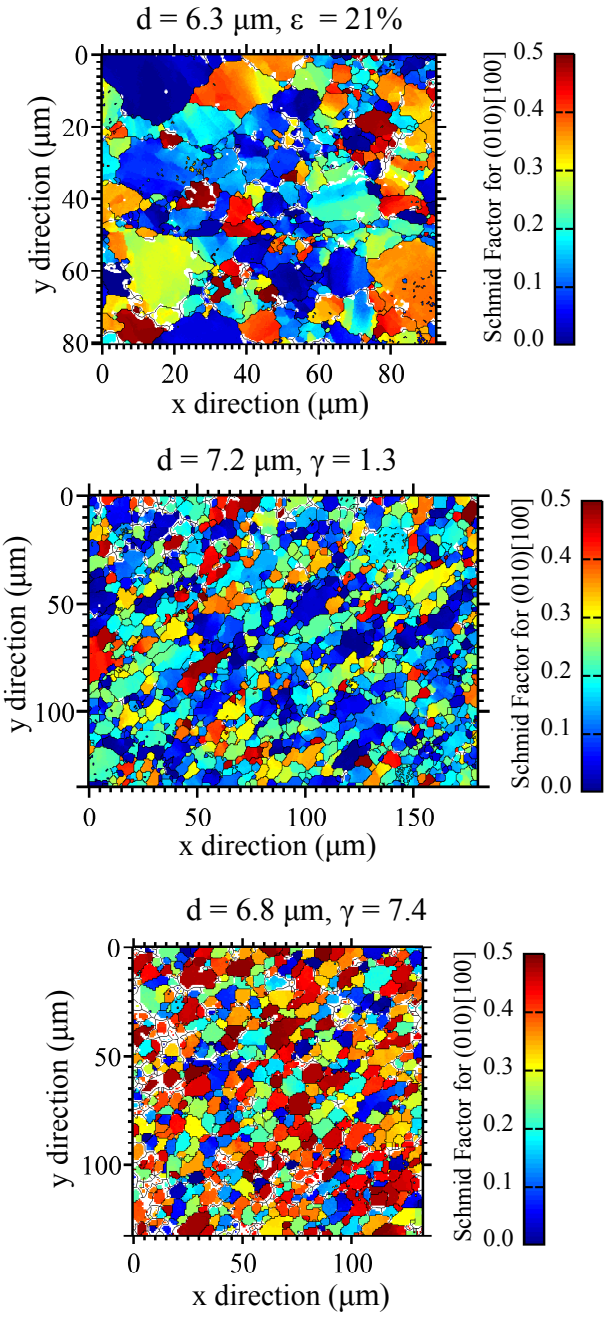

Figure 4.1: Maps of grains, reconstructed from EBSD data, for samples PI3-1477 (top), PI10-941 (middle), and PI10-949 (bottom). Colors represent values of Schmid factor calculated for the (010)[100] slip system.

where *b* is the Burgers vector and *n* is a unit vector normal to the slip plane for each slip system. The shear stress resolved onto each slip system, τ^{α}, is calculated by

$$\tau^{\alpha} = \boldsymbol{\mu}^{\alpha} : \boldsymbol{S'}, \tag{4.6}$$

where the deviatoric stress tensor, $\boldsymbol{S'}$, is

$$\boldsymbol{S'} = \begin{bmatrix} \sigma_{11} - \sigma_{\mathrm{m}} & \sigma_{12} & \sigma_{13} \\ \sigma_{21} & \sigma_{22} - \sigma_{\mathrm{m}} & \sigma_{23} \\ \sigma_{31} & \sigma_{32} & \sigma_{33} - \sigma_{\mathrm{m}} \end{bmatrix}, \tag{4.7}$$

and $\sigma_{\mathrm{m}} = \frac{1}{3}\mathrm{trace}(\boldsymbol{\sigma'})$.

Once the differential stress on each slip system, $\Delta\sigma^{\alpha}$, is determined from

$$\Delta\sigma^{\alpha} = |2\tau^{\alpha}|, \tag{4.8}$$

the strain rate due to dislocation glide is calculated. The strain rate due to glide, $\dot{\varepsilon}_g^{\alpha}$, on each slip system is then calculated using the flow laws from Table 4 of *Bai et al.* (1991) for olivine single crystals deforming by dislocation creep, which is

$$\dot{\varepsilon}_{\mathrm{g}}^{\alpha} = \dot{\varepsilon}_{\mathrm{g}}^{\alpha}\left(\Delta\sigma^{\alpha}, T, f_{\mathrm{O}_2}\right) \mathrm{sgn}\left(\tau^{\alpha}\right), \tag{4.9}$$

where $\mathrm{sgn}\left(\tau^{\alpha}\right)$ indicates the sign (positive or negative) of the value of the resolved shear stress on the given slip system. The $[110]_{\mathrm{c}}$, $[101]_{\mathrm{c}}$, and $[011]_{\mathrm{c}}$ orientations were assumed to deform by operation of the (010)[100], (001)[100], and (010)[001] slip systems, respectively. To calculate the total strain rate due to glide in each grain, shear strain rates from glide, $\dot{\gamma_g^{\alpha}}$, are required:

$$\dot{\gamma_g^{\alpha}} = 2\,\dot{\varepsilon}_g^{\alpha}. \tag{4.10}$$

The strain rate tensor for glide in the crystallographic reference frame, $\dot{\boldsymbol{\varepsilon}}'_g$, is determined for each grain by summing the contribution from all of the slip systems:

$$\dot{\boldsymbol{\varepsilon}}'_g = \sum_{\alpha=1}^{3} \boldsymbol{\mu}^{\alpha} \dot{\gamma}_g^{\alpha}. \tag{4.11}$$

To calculate the strain rate of the aggregate, the strain rate tensor must be rotated back into the sample reference frame. The strain rate tensor for each grain in the sample reference frame, $\dot{\boldsymbol{\varepsilon}}_{\text{grain}}$, is

$$\dot{\boldsymbol{\varepsilon}}_{\text{grain}} = \mathbf{R}^{\text{T}}\, \dot{\boldsymbol{\varepsilon}}'_g\, \mathbf{R} = \begin{bmatrix} \dot{\varepsilon}_{11} & \dot{\varepsilon}_{12} & \dot{\varepsilon}_{13} \\ \dot{\varepsilon}_{21} & \dot{\varepsilon}_{22} & \dot{\varepsilon}_{23} \\ \dot{\varepsilon}_{31} & \dot{\varepsilon}_{32} & \dot{\varepsilon}_{33} \end{bmatrix}. \tag{4.12}$$

Assuming a uniform stress state and ignoring strain compatibility, we estimate the volume-averaged strain rate from

$$\dot{\boldsymbol{\varepsilon}} = \frac{\sum_{\alpha=1}^{\text{N}} \dot{\boldsymbol{\varepsilon}}_{\text{grain}}^{\alpha} V_{\text{grain}}^{\alpha}}{\sum_{\alpha=1}^{\text{N}} V_{\text{grain}}^{\alpha}}, \tag{4.13}$$

where V_{grain} is the volume of each grain. The calculated value of the equivalent strain rate due to dislocation creep using the measured crystallographic orientations from deformation experiments, $\dot{\varepsilon}_{\text{dis}}$, is

$$\dot{\varepsilon}_{\text{dis}} = \sqrt{\frac{2}{3}\, \dot{\varepsilon}_{ij}\, \dot{\varepsilon}_{ji}}\,, \tag{4.14}$$

which allows for comparison between experiments carried out in different deformation geometries. Values of $\dot{\varepsilon}_{\text{dis}}$ were calculated using the distribution of grain orientations as determined from EBSD analyses, $\dot{\varepsilon}_{\text{calc-fabric}}$, and calculated from a uniform fabric, $\dot{\varepsilon}_{\text{calc-uni}}$, generated from a large population of random grain orientations. A complete description of the MATLAB® script used to carry out the calculations is presented in Appendix A.

4.3 Results

Calculated values of equivalent strain rate for individual grains determined from Equation 4.12 depend upon grain orientation, as illustrated in Figure 4.2. The grains with the largest values of resolved shear stress on (010)[100] ($RSS_{(010)[100]}$) have the highest values and smallest range of calculated equivalent strain rate. Grains that have the smallest values of $RSS_{(010)[100]}$ generally have lower values and a larger range of calculated equivalent strain rate.

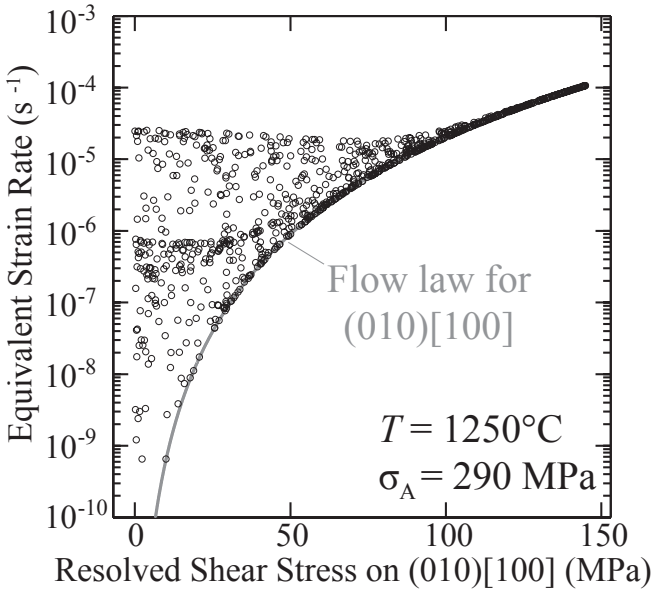

Figure 4.2: Calculated values of equivalent strain rate for each grain in a compression experiment as a function of resolved shear stress on the (010)[100] slip system.

The primary microstructural difference between samples deformed in triaxial compression to those deformed in direct shear and torsional shear is the strength and geometry of the LPO as presented in Figure 4.3. For the case of compression, the [010] axes align preferentially with the compression axis, and the [100] and [001] axes form a girdle perpendicular to the orientation of the compression axis. For direct shear and torsion experiments, the [100] axes preferentially align in the direction of shear, and the [010] and [001] axes form a girdle around the direction of shear that is associated with a maximum of [010] perpendicular to the shear plane. Values

for the J-index, a measure of fabric strength (*Bunge*, 1982), range from 1.2 for compression experiments and up to 5.5 for torsion experiments.

To quantify the difference between the measured strain rate, $\dot{\varepsilon}_{\,\mathrm{meas}}$, and $\dot{\varepsilon}_{\,\mathrm{calc\text{-}fabric}}$, we define the strain rate enhancement factor, f, as

$$f = \frac{\dot{\varepsilon}_{\,\mathrm{meas}}}{\dot{\varepsilon}_{\,\mathrm{calc\text{-}fabric}}} \,. \tag{4.15}$$

Measured and calculated values of strain rate and associated values of f are presented in Table 4.1. The values of f vary as a function of grain size, but are nearly independent of stress and LPO, as illustrated in Figure 4.4. A least-squares fit of f as a function of grain size measured at the end of each experiment yields

$$f = 10^{1.1 \pm 0.6} d^{-1.0 \pm 0.7} \,, \tag{4.16}$$

where d is the grain size in 10^{-6} m.

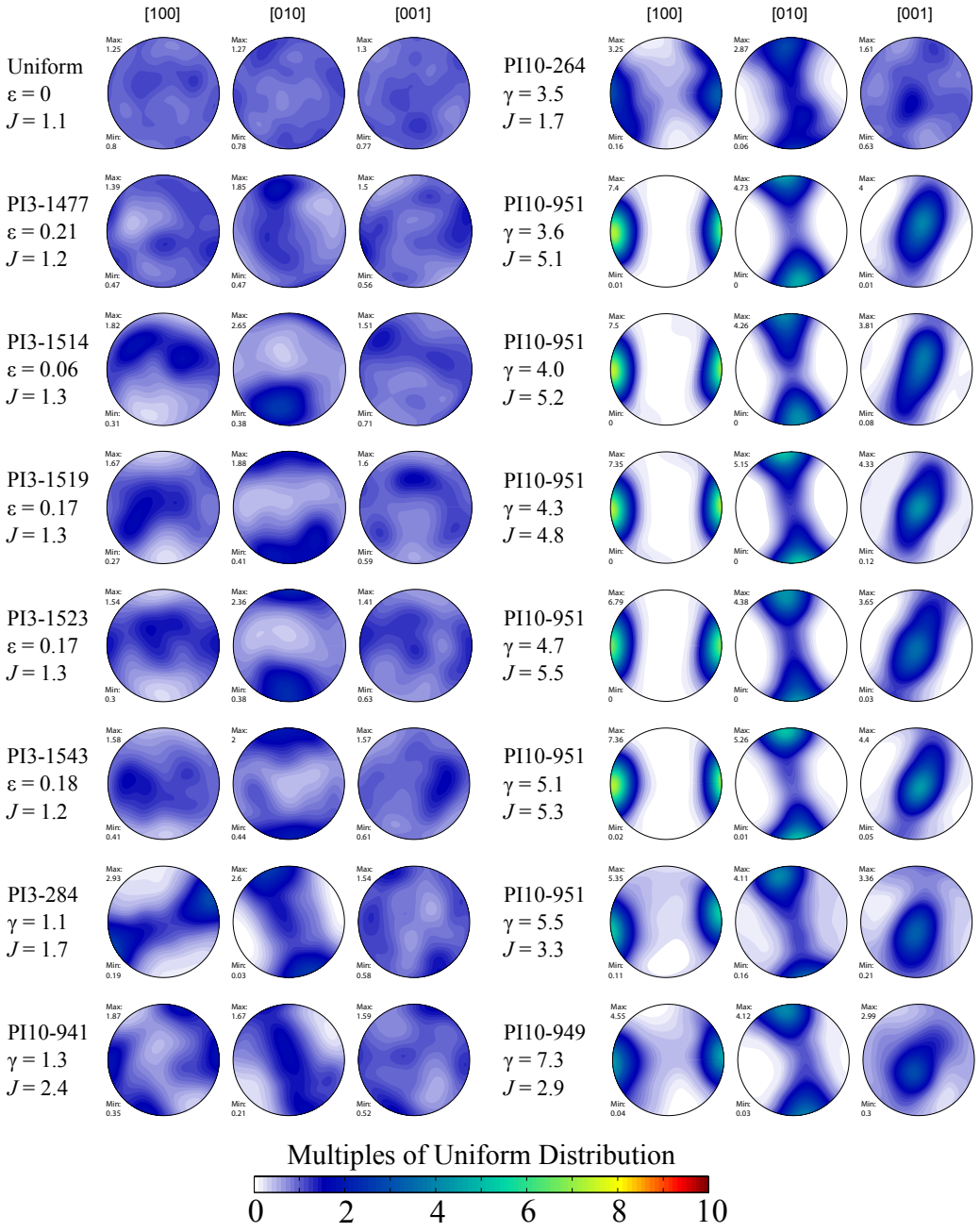

Figure 4.3: Equal area, lower hemisphere pole figures generated from EBSD measurements for each data set used in the micromechanical model. Values of multiples of uniform distribution are represented by the color scale. All of the experiments performed on PI3 were carried out in triaxial compression, with the exception of PI3-284, which was carried out in direct shear. The experiments preformed using PI10 were carried out in torsional shear. The orientation of maximum compression is to the north for pole figures from compression experiments and the direction of shear is top to the right for pole figures from shear experiments.

Exp #	σ (MPa)	d (μm)	T (K)	γ	J	$\dot{\varepsilon}_{meas}$ (s^{-1})	$\dot{\varepsilon}_{calc-fabric}$ (s^{-1})	$\dot{\varepsilon}_{calc-uni}$ (s^{-1})	f
PI3-1477$^{\downarrow}$	304	6.3	1473	0.4	1.2	5.60E-05	2.30E-05	2.99E-05	2.4
PI3-1514$^{\downarrow}$	328	20.0	1473	0.1	1.3	1.50E-05	3.10E-05	3.90E-05	0.5
PI3-1519$^{\downarrow}$	290	4.6	1473	0.2	1.3	6.20E-05	2.00E-05	2.54E-05	3.1
PI3-1523$^{\downarrow}$	420	5.4	1473	0.3	1.3	9.80E-05	7.30E-05	9.27E-05	1.3
PI3-1543$^{\downarrow}$	441	16.0	1473	0.4	1.2	7.00E-05	8.60E-05	1.10E-04	0.8
PI3-284$^{\rightleftharpoons}$	414	7.0	1473	1.1	1.7	1.70E-04	1.00E-04	5.18E-05	1.7
PI10-941$^{\circlearrowleft}$	227	7.2	1523	1.3	2.4	1.30E-04	2.80E-05	6.32E-06	4.6
PI10-264$^{\circlearrowleft}$	369	3.6	1473	3.5	1.7	1.86E-04	8.50E-05	3.46E-05	2.2
PI10-951$^{\circlearrowleft}$	171	12.1	1523	3.6	5.1	3.60E-05	5.48E-05	2.35E-06	0.7
PI10-951$^{\circlearrowleft}$	177	12.1	1523	4.0	5.2	4.00E-05	5.84E-05	2.65E-06	0.7
PI10-951$^{\circlearrowleft}$	182	11.4	1523	4.3	4.8	4.40E-05	6.32E-05	2.92E-06	0.7
PI10-951$^{\circlearrowleft}$	187	11.5	1523	4.7	5.5	4.70E-05	7.58E-05	3.21E-06	0.6
PI10-951$^{\circlearrowleft}$	191	10.9	1523	5.1	5.3	5.10E-05	7.77E-05	3.45E-06	0.7
PI10-951$^{\circlearrowleft}$	197	11.6	1523	5.5	3.3	5.70E-05	5.86E-05	3.85E-06	1.0
PI10-949$^{\circlearrowleft}$	238	6.8	1523	7.4	2.9	1.90E-04	6.40E-05	7.46E-06	3.0

$^{\downarrow}$triaxial compression $^{\rightleftharpoons}$direct shear $^{\circlearrowleft}$torsional shear

Table 4.1: Table of experimental conditions and results of the micromechanical model. Values of σ and $\dot{\varepsilon}$ are in equivalent terms. Strain in compression experiments was converted to shear strain for comparison. The deformation geometry for each experiment is indicated by the symbols referenced below the table. Data from compression and direct shear experiments were previously reported in *Hansen et al.* (2011) and *Lee et al.* (2002) respectively.

4.4 Discussion

The values of f presented in Table 4.1 indicate that the strain rates obtained from the micromechanical model are often significantly slower than those measured experimentally over a large range of conditions of grain size, stress, and LPO strength. Calculations of aggregate plasticity can be made using end-member models (uniform stress versus uniform strain rate) to bound the most realistic scenarios (e.g., *Dawson and Wenk*, 2000). Here we made the simplifying assumption that all grains were subject to the same stress state (*Sachs*, 1928), which ignores compatibility requirements. This end-member model describes the fastest strain rates possible with purely intragranular plasticity. Although more sophisticated grain-scale micromechanical models are available, such as those described by *Lebensohn and Tomé* (1993), we have taken the most conservative approach to characterizing the discrepancies between experiments and calculations. Therefore, values of f in Table 4.1 are minimum estimates.

In light of these observations, it is clear that the experimentally measured strain rate cannot be accounted for by the activity of intragranular dislocations alone. As illustrated in Figure 4.4, the ratio of the measured to calculated strain rates increases with decreasing grain size, implying that a grain-size sensitive deformation mechanism is operating. Published flow laws for olivine aggregates (*Hansen et al.*, 2011; *Hirth and Kohlstedt*, 2003) demonstrate that strain rates due to diffusion creep (a grain-size sensitive mechanism) at the conditions of these experiments account for only 0.1 to 21% of the measured strain rates; thus diffusion creep cannot be responsible for the observed discrepancies. Furthermore, values of stress exponents measured by load-stepping sequences in triaxial compression experiments and rate-stepping excursions in torsion experiments are between 2 and 4, indicating the importance of the motion of dislocations to the strain rate. The combination of high values of n and observed grain-size sensitivity indicate deformation occurred in the GSS power-law rheological regime.

One mechanism proposed to account for GSS power-law creep of quartz (*Platt and Behr*, 2011) and olivine (*Johanesen and Platt*, 2015) is dynamic recrystallization (DRX) controlled dislocation creep. In this creep regime, strain-induced grain boundary migration acts to grow

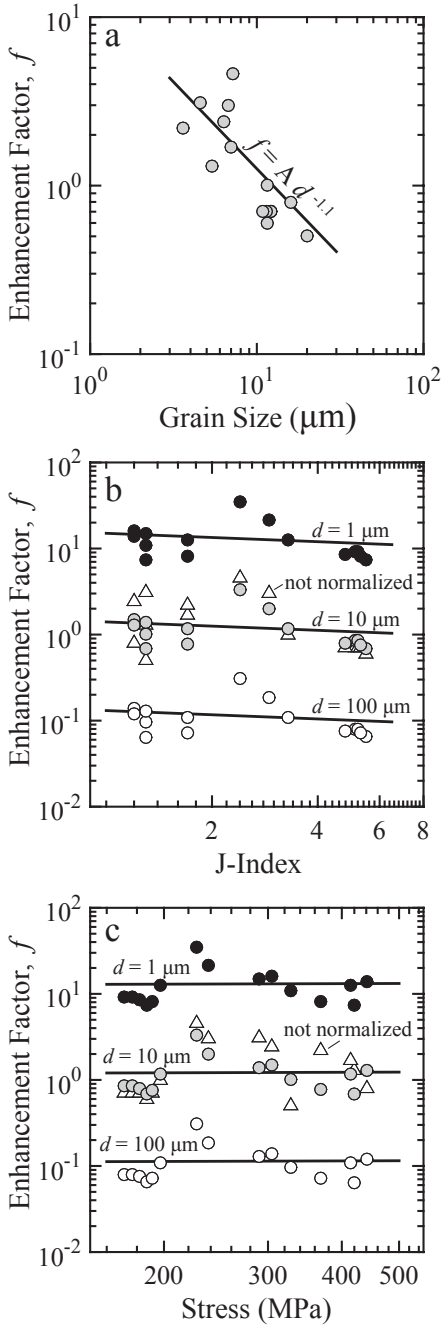

Figure 4.4: (a) Strain rate enhancement factor (f) as a function of grain size. The line is a least squares fit of the data represented by Equation 4.16. (b) f as a function of J index. (c) f as a function of equivalent stress. The values of f in plots (b) and (c) were normalized to grain sizes of 1 (black circles), 10 (grey circles), and 100 μm (white circles) using Equation 4.16 and the triangles represent non-normalized values. The lines in (b) and (c) are least square fits of grain-size normalized values of f as function of J-index or stress. The results indicate that, at constant grain size, f is independent of J-index and stress with $f \propto J^{-0.2\pm0.5}$ and $f \propto \sigma^{0.0\pm1.0}$.

grains with low dislocation densities at the expense of those with high dislocation densities. This process works to counteract strain hardening induced by the presence of sessile dislocations in grains. *Johanesen and Platt* (2015) argue that this mechanism was operating in exhumed peridotite shear zones, largely because curved and lobate grain boundaries are taken to indicate high rates of grain-boundary migration.

Microstructural observations from laboratory experiments argue against DRX controlled creep as the primary mechanism operating during high-temperature deformation of olivine aggregates. Analyses of experimentally deformed olivine aggregates indicate that grains with the largest dislocation densities are those with the largest Schmid factor for the (010)[100] dislocation slip system in both low strain compression experiments (*Farla et al.*, 2011) and higher strain direct shear experiments (*Lee et al.*, 2002). Thus, one would expect that strain driven grain boundary migration selectively removes grains that are well orientated with respect to the externally applied stress for deformation on the (010)[100] dislocation slip system. If DRX controlled creep were the dominant mechanism operating during deformation, migration of grain boundaries would create an aggregate with either a random LPO or a LPO with a maximum of [001] parallel to the shear direction. We therefore conclude that although DRX creep may be important during low-temperature deformation, observations of the LPOs that develop during anhydrous deformation of olivine aggregates argue against its importance at high-temperature conditions.

Dislocation-accommodated GBS (disGBS) has been identified as an important deformation mechanism in olivine aggregates based on experiments performed in the GSS power-law rheological regime (*Hirth and Kohlstedt*, 1995, 2003; *Wang et al.*, 2010; *Hansen et al.*, 2011). Similar behavior has been documented in other geological materials including calcite (*Schmid et al.*, 1977; *Walker et al.*, 1990) and ice (*Goldsby and Kohlstedt*, 2001). The results of these studies are in good agreement with theoretical models of grain-boundary sliding accommodated by the motion of intragranular dislocations as described by *Langdon* (1994).

In contrast to the incompatibility of DRX controlled creep with observed LPOs, disGBS

is compatible with the nature and strength of the LPO observed in samples deformed in laboratory experiments. During disGBS, displacements along grain boundaries are coupled with the motion of lattice dislocations in adjacent grains (*Hirth and Kohlstedt*, 2003). This coupling results in a significant contribution of intracrystalline dislocation processes to the strain rate of a deforming aggregate and therefore to the rotation and preferred alignment of individual grains. Observations of LPO development during GSS power-law creep (e.g., *Hansen et al.*, 2012, 2014) are consistent with this process. The similarities between observations of LPO in olivine aggregates deformed during GSS power-law creep and those predicted from models of GSI power-law creep (e.g., *Tommasi et al.*, 2000; *Kaminski and Ribe*, 2001; *Castelnau et al.*, 2009) are consistent with significant operation of intracrystalline dislocation processes during disGBS.

Laboratory-derived flow laws for GSS power-law creep have values of n between those for diffusion creep and dislocation creep. This observation suggests that GSS power-law creep may be due to simultaneous operation of diffusion and dislocation creep. However, the results presented in Figure 4.4 indicate the observed GSS power-law regime attributed to the operation of one deformation mechanism. If the rheological behavior attributed to disGBS were actually only the result of simultaneous operation of diffusion creep and dislocation creep, then one would expect the LPOs observed at high-strain conditions in Figure 4.3, which promote an increase in the resolved shear stress acting upon the weakest dislocation slip system, to promote dislocation creep over diffusion creep. In this scenario, increasing the strength of the crystallographic fabric would result in a significant decrease of the contribution of grain-size sensitive deformation to the total strain rate, a situation that would result in a strong decrease in f with increasing LPO strength. In contrast, the results presented in Figure 4.4b indicate that values of f, which describe the contribution of grain size sensitive deformation, remain essentially constant with increasing LPO strength.

The results presented in Figure 4.4c indicate that f is not dependent on stress for the studied

experimental conditions. This result is also consistent with the operation of all of the experiments in one rheological regime. If the observed GSS mechanism were the result of a combination of two processes, the values of f would decrease with increasing stress, which is not observed. Therefore, disGBS must be a separate deformation mechanism rather than a transition between diffusion creep and dislocation creep. This conclusion is supported by the experimentally derived flow laws for olivine aggregates presented in Figure 4.5, where it is apparent that the strain rate from the disGBS flow law cannot be explained by a combination of the diffusion and dislocation creep flow laws. If the strain rate from disGBS were actually due to a combination of the two mechanisms, the dashed line, which represents a combination of diffusion creep and dislocation creep in Figure 4.5, would correspond with the solid line representing disGBS. However, the dashed line is a factor of 6 lower in strain rate than the disGBS flow law for the stress at which the diffusion and dislocation creep flow laws intersect.

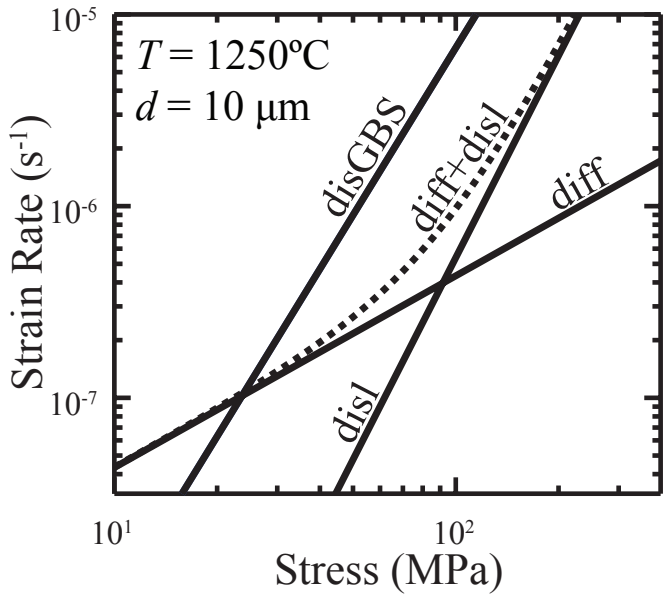

Figure 4.5: Strain rate as a function of stress with flow laws for diffusion creep (diff) and dislocation creep (disl) from *Hirth and Kohlstedt* (2003) and dislocation-accommodated grain boundary sliding (disGBS) from *Hansen et al.* (2011) at conditions typical of laboratory experiments. The dashed line is a sum of the strain rates from the diffusion and dislocation creep flow laws.

Investigations of the rheological behavior of ice (*Goldsby and Kohlstedt*, 2001) and olivine (*Hirth and Kohlstedt*, 2003) at relatively low strain conditions indicate the the strain rate of the disGBS mechanism is limited by either the strain rate from displacement along grain boundaries ($\dot{\varepsilon}_{\mathrm{GBS}}$) or the strain rate from the weakest dislocation slip system ($\dot{\varepsilon}_{\mathrm{easy}}$). Comparison of values of $\dot{\varepsilon}_{\mathrm{easy}}$ determined from the flow laws of *Bai et al.* (1991) and $\dot{\varepsilon}_{\mathrm{GBS}}$ estimated from the analyses of *Jackson et al.* (2014) indicates that $\dot{\varepsilon}_{\mathrm{easy}} \approx 10^{-6}\ \dot{\varepsilon}_{\mathrm{GBS}}$ for the experimental conditions used in this study. Therefore, $\dot{\varepsilon}_{\mathrm{disGBS}}$ would be expected not to surpass $\dot{\varepsilon}_{\mathrm{easy}}$. This relationship is consistent with the observations presented in Figure 4.6.

A comparison of all of the data in Table 4.1 demonstrates that $\dot{\varepsilon}_{meas}$ / $\dot{\varepsilon}_{easy}$ approaches unity at conditions of higher strain, as presented in Figure 4.7. As the value of the J-index increases, $\dot{\varepsilon}_{meas}$ / $\dot{\varepsilon}_{easy}$ increases rapidly. However, for a value of J-index greater than 2, $\dot{\varepsilon}_{meas}$ / $\dot{\varepsilon}_{easy}$ remains relatively constant at approximately unity. This observation is consistent with deformation that is rate limited by the strength of the weakest dislocation slip system. The implication of these observations is that the strain rate of olivine aggregates deforming by the disGBS mechanism will approach the strain rate of the weakest slip systems once a LPO has developed. However, results carried out over a larger range in temperature and grain size are required to test this hypothesis.

4.5 Conclusions

Our analysis demonstrates that the observed strain rate in deformation experiments of olivine aggregates cannot be explained by the operation of intragranular dislocation or diffusion mechanisms alone. A deformation mechanism that is both grain-size sensitive and has a power-law dependence of strain rate upon stress must operate. The independence of values of f on stress and fabric strength indicates a simple combination of diffusion creep and dislocation creep cannot account for the observed strain rate. Therefore, disGBS operates in olivine aggregates over a large range of conditions of stress and crystallographic fabric strength.

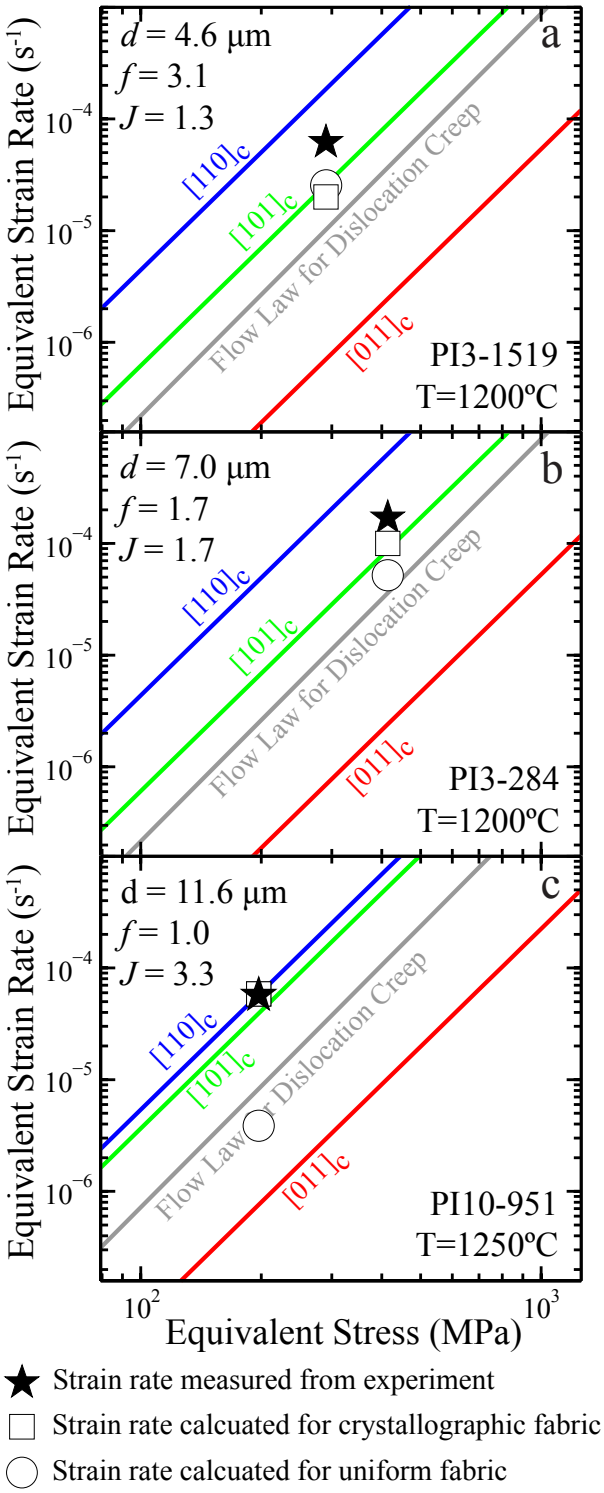

Figure 4.6: Equivalent strain rate as a function of equivalent stress for data from samples deformed in compression (a), direct shear (b), and torsion (c). The gray line is the flow law for dislocation creep of dunite from *Keefner et al.* (2011) and the colored lines are the single crystal flow laws from *Bai et al.* (1991).

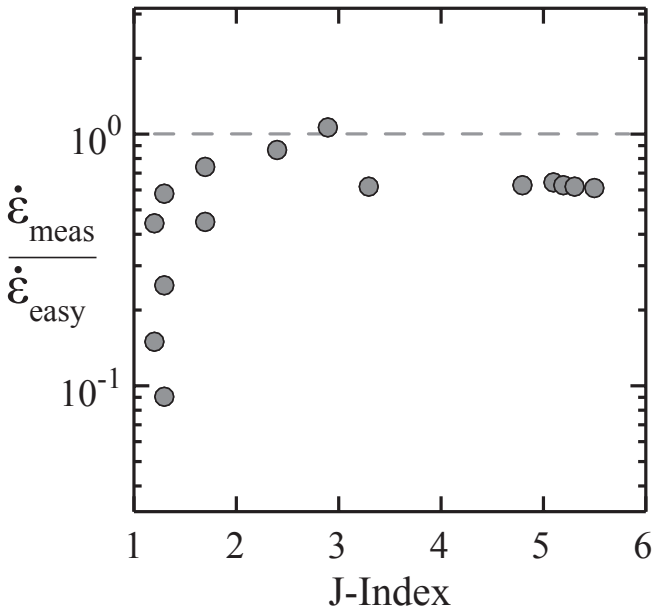

Figure 4.7: Ratio of measured strain rate to the strain rate for the flow law for single crystals in the $[110]_c$ orientation from *Bai et al.* (1991) as a function of J-index. Conditions at which the measured strain rate is equal to the flow law for the easy slip system are indicated by the horizontal dashed line.

Chapter 5

Conclusions

5.1 Summary of results

In this thesis, the flow behavior of olivine was investigated by carrying out experiments on olivine single crystals and developing a micromechaincal model that connects single crystal flow laws to polycrystalline deformation. A review of the main points from each chapter is presented here.

Chapter 1 The purpose of studying the flow behavior of olivine single crystals is explained. Analyses of mechanical data from single crystal deformation experiments allow for the precise determination of the value of the stress sensitivity under a large range of conditions. These experimentally determined values have important implications for extrapolating data from laboratory to upper mantle conditions. Single crystals also provide excellent opportunities to study hydrolytic weakening without the added complication introduced by the presence of water on grain boundaries in fine grained samples. Importantly, single crystals provide an excellent opportunity to model polycrystalline deformation.

Chapter 2 Direct shear experiments were performed on olivine single crystals to determine the relative strength of the (001)[100] and (100)[001] slip systems. The results demonstrate that the (100)[001] slip system is weaker than the (001)[100] slip system in the glide-controlled

dislocation creep regime whereas the (001)[100] slip system is weaker than the (100)[001] slip system in the climb-controlled regime. These observations have important implications for the development of lattice-preferred orientation of olivine-rich rocks at mantle conditions.

Chapter 3: Triaxial compression experiments were carried out on olivine single crystals under hydrous conditions. Comparison of results under hydrous conditions to previous results from crystals deformed under anhydrous conditions indicates significant weakening occurs at asthenospheric mantle temperatures in the climb-controlled dislocation creep regime. Under anhydrous conditions, flow law parameters are consistent with deformation that is rate limited by diffusion of silicon through the cores of dislocations. Under hydrous conditions, the flow law parameters are consistent with deformation that is rate limited by the diffusion of silicon through the olivine lattice. At low temperatures, the strain rate of both anhydrous and hydrous crystals are well described by the same exponential creep relationship, indicating hydrolytic weakening cannot be resolved in the glide-controlled dislocaion creep regime at the studied experimental conditions.

Chapter 4: A micromechanical model was developed that calculates the strain rate of a deforming aggregate based on anisotropy in the mechanical behavior at the crystal scale. Results indicate that the fastest possible strain rate from dislocation creep cannot account for the observed strain rate in deformation experiments on olivine aggregates. Furthermore, the results are consistent with the operation of a grain-size sensitive power-law creep regime that operates over a large range of conditions of stress, grain size, and strength of lattice-preferred orientation. Consideration of the microstructural observations and mechanical data suggest that the grain-size sensitive power-law regime is most consistent with the operation of dislocation-accommodated grain-boundary sliding in experimentally deformed olivine aggregates.

5.2 Implications and Future directions

5.2.1 Direct Shear Experiments at Hydrous Conditions

One promising direction to continue this work would involve carrying out direct shear experiment on olivine single crystals under hydrous conditions. In order to evaluate this opportunity, two exploratory experiments were carried out. No useful mechanical data were obtained from either experiment. However, in both experiments the crystals were successfully hydrated and a design was established to increase the success rate of future direct shear experiments on hydrous olivine single crystals.

The first attempt to shear an olivine single crystal under hydrous conditions consisted of an assembly similar to those carried out under anhydrous conditions, but with an additional sleeve of talc placed around the deformation assembly. A thin nickel sleeve was placed inside of the talc sleeve to avoid direct contact of the talc with the olivine crystal. Post-deformation observation of this experiment demonstrated that most of the deformation occurred by slipping along the interface between the crystal and the alumina piston and by deformation of the alumina piston and spacers, as presented in Figure 5.1. It appears likely that during the pressurization phase of the experiment, the talc penetrated the inner nickel sleeve and filled the open space at the ends of the olivine crystal. The talc subsequently reacted with the alumina shear pistons and spacers. The results of this experiment demonstrate the importance of separating talc from alumina during these types of experiments.

Changes were made to the deformation assembly in order to avoid the interaction of talc and alumina that occurred in PI-1789. Most importantly, the problem arising form the void at the ends of the crystal was resolved by using oval-shaped crystals. These crystals were manufactured by coring cylinders from olivine crystals and the cutting slices at 45°. This type of direct shear assembly was used in PI-1791, as presented in Figure 5.2. However, problems with the internal load cell prevented deformation during this experiment so a hydration anneal was carried out instead.

The direct shear assemblies used in PI-1789 and PI-1791 were able to maintain a modest

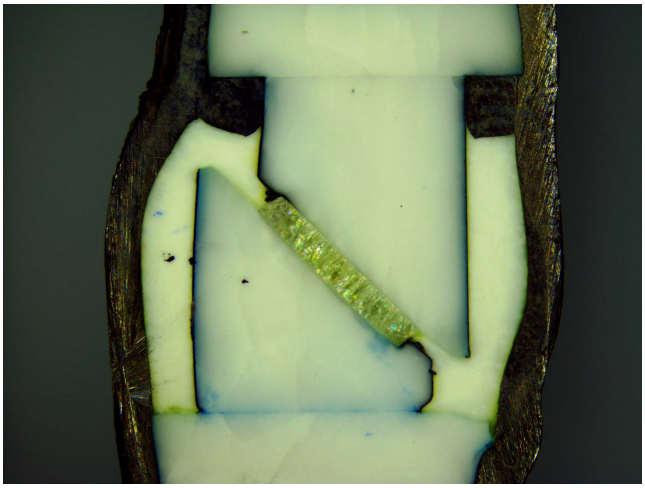

Figure 5.1: Reflected light image of experiment PI-1789. The crystal was oriented for shear on (001)[100] using alumina pistons. During pressurization, the talc sleeve surrounding the shear pistons and crystal were able to penetrate the thin protective sleeve of nickel. The strength of the alumina was greatly reduced by its reaction with talc. Although the crystal was slightly deformed, most of the deformation took place in the weakened alumina pistons and spacers.

amount of hydrogen throughout the duration of each experiment. Post-experiment FTIR spectra presented in Figure 5.3 reveal peaks with heights and positions characteristic of O-H stretching bands. However, the calculated values of hydrogen content of 98 and 125 ppm H/Si were slightly lower than expected for saturation at the given conditions.

Although the design used in PI-1791 successfully isolates the talc from the alumina during the experiment, there are some disadvantages to using an oval shaped single crystal. As a single crystal of this shape is sheared, areas at the ends of the crystals are not under load. This results in a complicated stress state where dislocations are moving in repose to the applied stress and encounter low stress regions at the end of the crystal. To avoid this problem, a nickel sample holder was designed to fill the gap at the ends of the crystal (and thus remove the driving force for the talc to break the nickel sleeve around the alumina shear pistons) and hold a crystal in place. The concept of the direct shear crystal holder is presented in Figure 5.4 and a crystal positioned inside of a prototype is presented in Figure 5.5.

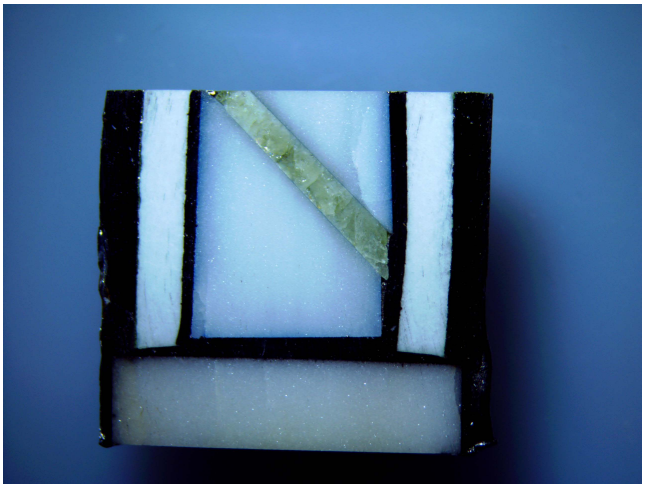

Figure 5.2: Reflected light image of experiment PI-1791. The crystal was oriented for shear on (001)[100] using alumina pistons. The talc was successfully isolated from the alumina, but problems with the load cell prevented deformation. The sample had to be cut in half in order to identify the shear direction, before completing the usual cut in the plane that includes the direction of maximum comprehensive force and the shear direction.

5.2.2 Direct Shear on the (010)[100] and (010)[001] Slip Systems

Nine attempts were made to deform single crystals oriented for shear on the (010)[100] and (010)[001] dislocation slip systems under anhydrous conditions. These experiments were carried out using pistons fabricated from alumina and thoriated tungsten. All of the attempts to shear a crystal parallel to the (010) plane were unsuccessful and resulted in slipping on the interface between the crystal and the shear piston. A compilation of the experimental conditions, crystal orientations, and piston materiel used for these experiments is presented in Table 5.1.

An experiment attempted with porous alumina as the shear piston material is presented in Figure 5.6. This experiment was attempted because the larger frictional properties from the roughness of the porous alumina was hypothesized to prevent slipping on the interface between the crystal and the shear piston. In addition, at experimental conditions the pores in the porous alumina are at conditions of lower pressure and therefore the surface of the crystal attempts to move into the pores, which may aid in adhesion. However, the roughness of the porous alumina surface resulted in a smaller area of contact between the shear piston and the crystal.

Table 5.1: Unsuccessful direct shear experiments

Exp. #	T(°)C	slip system	shear pistons
1873	1200	(010)[100]	alumina
1875	1100-1200	(010)[100]	alumina
1876	1100-1200	(010)[100]	alumina
1879	1100-1200	(010)[100]	alumina
1880	1100-1200	(010)[100]	alumina
1881	1000-1200	(010)[100]	porous alumina
1882	1100-1200	(010)[001]	alumina with ledge
1883	1200	(010)[001]	thoriated tungsten
1894	1200	(010)[100]	alumina

An experiment was also attempted using ledges ground into the shear pistons to prevent slipping. The ledges were ground into the shear piston using a diamond polishing wheel. The ledges provided an additional step that would support the crystals along the surfaces normal to the shear direction. However, the shear pistons fractured during the experiment, presumably due to the stress concentration along the ledges, as presented in Figure 5.7.

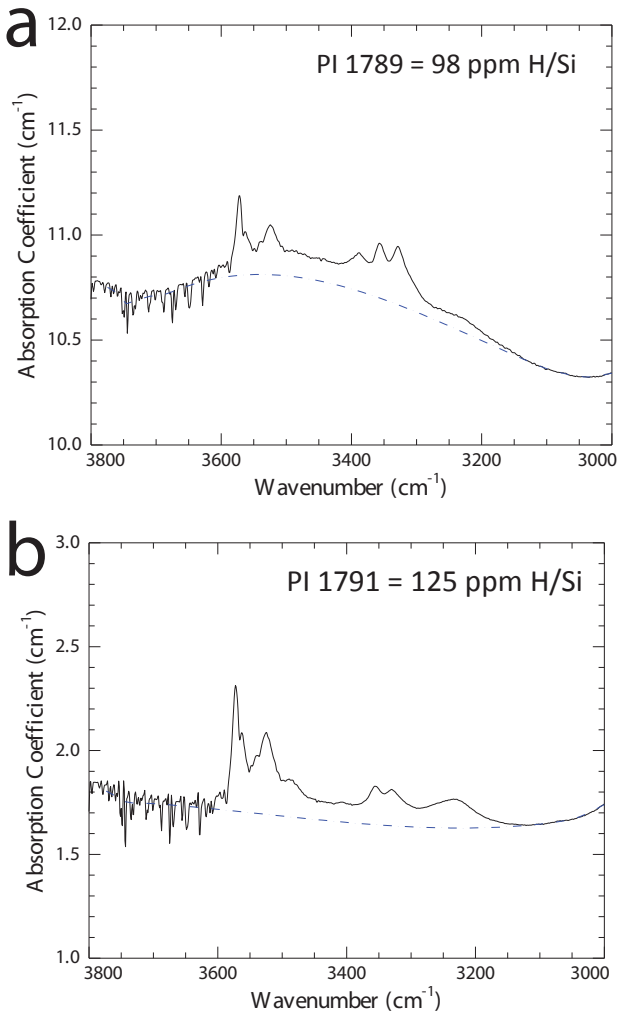

Figure 5.3: FTIR spectra taken with an unpolarized IR beam parallel to the [010] axis for (a) PI-1789 and (b) PI-1791. The black lines represent IR absorption and the dashed blue line is the baseline used to calculate hydrogen content. The labeled hydrogen content was calculated using the method of *Paterson* (1982) multiplied by a factor of 3.5 as suggested by *Bell et al.* (2003).

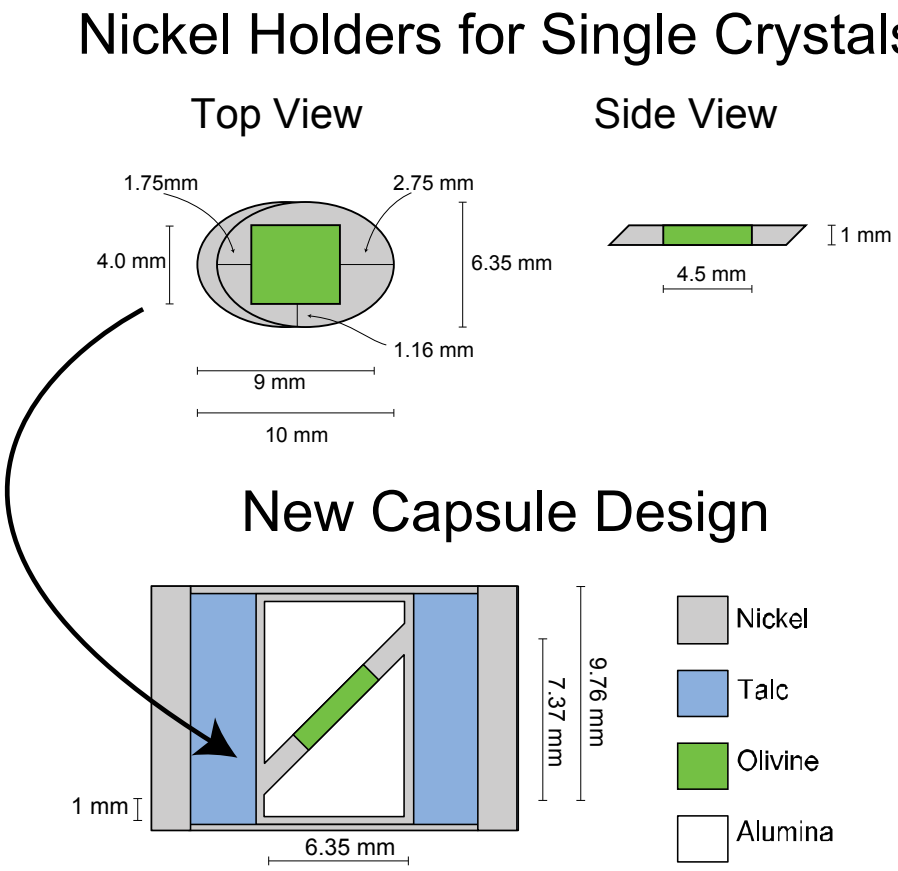

Figure 5.4: Illustration of single crystal holder for direct shear experiments under hydrous conditions.

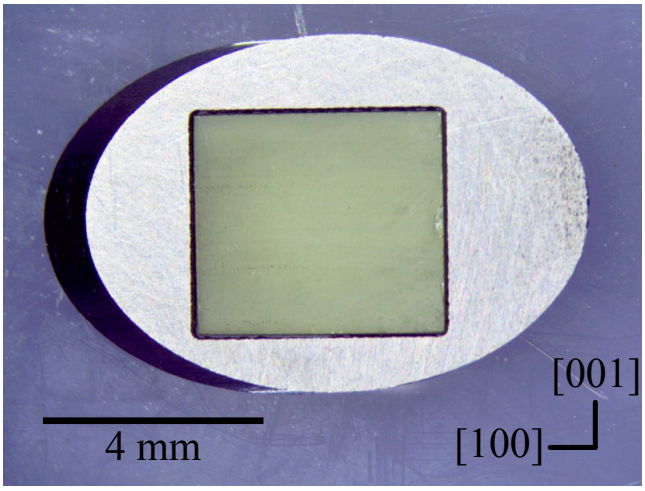

Figure 5.5: Reflected light image of a single crystal inside of a nickel holder for direct shear experiments.

Figure 5.6: Reflected light image of experiment PI-1881. The crystal was oriented for shear on (010)[100] using porous alumina pistons. The surrounding metal is a nickel capsule and there are solid alumina spacers on the top and the bottom of the shear pistons. The bottom spacer fractured while cutting the deformation capsule after the experiment.

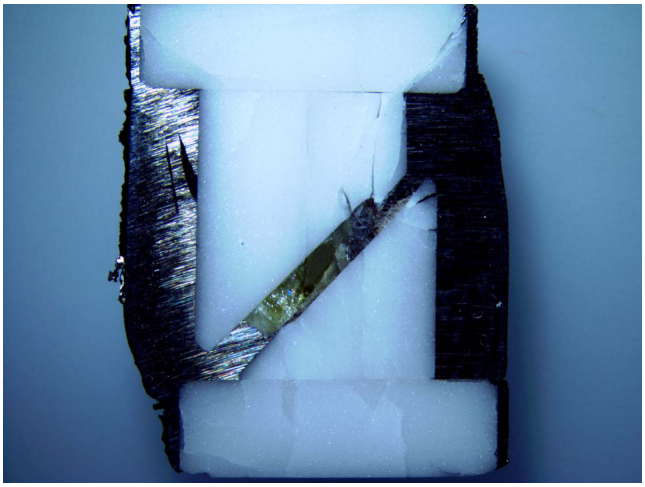

Figure 5.7: Reflected light image of experiment PI-1882. The crystal was oriented for shear on (010)[100] using alumina pistons with a ledge ground into them. The surrounding metal is a nickel capsule and there are solid alumina spacers on the top and the bottom of the shear pistons. The top piston fractured along the ledge and the crystal was able to slide over the ledge on the bottom piston.

References

Bachmann, F., R. Hielscher, and H. Schaeben (2010), Texture analysis with mtex–free and open source software toolbox, *Solid State Phenomena*, *160*, 63–68.

Bai, Q., and D. Kohlstedt (1992), High-temperature creep of olivine single crystals, 2. dislocation structures, *Tectonophysics*, *206*(1), 1–29.

Bai, Q., and D. Kohlstedt (1993), Effects of chemical environment on the solubility and incorporation mechanism for hydrogen in olivine, *Physics and Chemistry of Minerals*, *19*(7), 460–471.

Bai, Q., S. Mackwell, and D. Kohlstedt (1991), High-temperature creep of olivine single crystals 1. Mechanical results for buffered samples, *J. Geophys. Res.*, *96*, 2441–2463, doi: doi:10.1029/90JB01723.

Becker, T., and H. Kawakatsu (2011), On the role of anisotropic viscosity for plate-scale flow, *Geophys. Res. Lett.*, *38*(17), L17307, doi:10.1029/2011GL048584.

Becker, T. W., S. Chevrot, V. Schulte-Pelkum, and D. K. Blackman (2006), Statistical properties of seismic anisotropy predicted by upper mantle geodynamic models, *Journal of Geophysical Research: Solid Earth (1978–2012)*, *111*(B8).

Bell, D., G. Rossman, J. Maldener, D. Endisch, and F. Rauch (2003), Hydroxide in olivine: A quantitative determination of the absolute amount and calibration of the ir spectrum, *Journal of Geophysical Research*, *108*(B2), 2105.

Bunge, H. (1982), *Texture analysis in materials science*, Butterworths, Boston.

Bystricky, M., K. Kunze, L. Burlini, and J. P. Burg (2000), High shear strain of olivine aggregates; rheological and seismic consequences, *Science*, *290*(5496), 1564–1567, doi: 10.1126/science.290.5496.1564.

Carter, N. L., and H. G. Ave'Lallemant (1970), High temperature flow of dunite and peridotite, *Geological Society of America Bulletin*, *81*(8), 2181–2202.

Castelnau, O., D. Blackman, R. Lebensohn, and P. Castañeda (2008), Micromechanical modeling of the viscoplastic behavior of olivine, *J. Geophys. Res*, *113*, B09,202, doi: 10.1029/2007JB005444.

Castelnau, O., D. K. Blackman, and T. W. Becker (2009), Numerical simulations of texture development and associated rheological anisotropy in regions of complex mantle flow, *Geophys. Res. Lett*, *36*, L12304, doi:10.1029/2009GL038027.

Chopra, P., and M. Paterson (1984), The role of water in the deformation of dunite, *J. Geophys. Res.*, *89*, 7861–7876, doi:doi:10.1029/JB089iB09p07861.

Coble, R. (1963), A model for boundary diffusion controlled creep in ceramic materials, *Journal of Applied Physics*, *34*(6), 1679–1682.

Costa, F., and S. Chakraborty (2008), The effect of water on si and o diffusion rates in olivine and implications for transport properties and processes in the upper mantle, *Physics of the Earth and Planetary Interiors*, *166*(1), 11–29.

Couvy, H., D. J. Frost, F. Heidelbach, K. Nyilas, T. Ungar, S. Mackwell, and P. Cordier (2004), Shear deformation experiments of forsterite at 11 GPa, 1400 degrees C in the multianvil apparatus, *European Journal of Mineralogy*, *16*(6), 877–889.

Darot, M., and Y. Gueguen (1981), High-temperature creep of forsterite single crystals, *Journal of Geophysical Research: Solid Earth (1978–2012)*, *86*(B7), 6219–6234.

Dawson, P. R., and H.-R. Wenk (2000), Texturing of the upper mantle during convection, *Philosophical Magazine A*, *80*(3), 573–598.

Demouchy, S., S. Schneider, S. Mackwell, M. Zimmerman, and D. Kohlstedt (2009), Experimental deformation of olivine single crystals at lithospheric temperatures, *Geophysical Research Letters*, *36*(4), L04,304.

Demouchy, S., A. Tommasi, T. B. Ballaran, and P. Cordier (2013), Low strength of earths uppermost mantle inferred from tri-axial deformation experiments on dry olivine crystals, *Physics of the Earth and Planetary Interiors*, *220*, 37–49.

Demouchy, S., A. Mussi, F. Barou, A. Tommasi, and P. Cordier (2014), Viscoplasticity of polycrystalline olivine experimentally deformed at high pressure and 900 c, *Tectonophysics*, *623*, 123–135.

Dohmen, R., S. Chakraborty, and H. Becker (2002), Si and O diffusion in olivine and implications for characterizing plastic flow in the mantle, *Geophys. Res. Lett.*, *29*(21), 2030, doi:10.1029/2002GL015480.

Druiventak, A., C. A. Trepmann, J. Renner, and K. Hanke (2011), Low-temperature plasticity of olivine during high stress deformation of peridotite at lithospheric conditions - an experimental study, *Earth and Planetary Science Letters*, *311*(3), 199–211.

Drury, M. (2005), Dynamic recrystallization and strain softening of olivine aggregates in the laboratory and the lithosphere, *243*(1), 143, doi:10.1144/GSL.SP.2005.243.01.11.

Drury, M., H. A. Lallemant, G. Pennock, and L. Palasse (2011), Crystal preferred orientation in peridotite ultramylonites deformed by grain size sensitive creep, étang de lers, pyrenees, france, *Journal of Structural Geology*, *33*(12), 1776–1789.

Durham, W. B., and C. Goetze (1977), Plastic flow of oriented single crystals of olivine 1. Mechanical data, *J. Geophys. Res.*, *82*(36), 5737–5753, doi:doi:10.1029/JB082i036p05737.

Durham, W. B., C. Goetze, and B. Blake (1977), Plastic flow of oriented single crystals of olivine 2. observations and interpretations of the dislocation structures, *J. Geophys. Res.*, *82*(36), 5755–5770, doi:10.1029/JB082i036p05755.

Durinck, J., B. Devincre, L. Kubin, and P. Cordier (2007a), Modeling the plastic deformation of olivine by dislocation dynamics simulations, *American Mineralogist*, *92*(8-9), 1346–1357.

Durinck, J., P. Carrez, and P. Cordier (2007b), Application of the peierls-nabarro model to dislocations in forsterite, *European Journal of Mineralogy*, *19*(5), 631–639.

Evans, B. (2005), Creep constitutive laws for rocks with evolving structure, *Geological Society, London, Special Publications*, *245*(1), 329–346.

Evans, B., and C. Goetze (1979), The temperature variation of hardness of olivine and its implication for polycrystalline yield stress, *J. Geophys. Res.*, *84*(B10), 5505–5524, doi: 10.1029/JB084iB10p05505.

Farla, R., J. F. Gerald, H. Kokkonen, A. Halfpenny, U. Faul, and I. Jackson (2011), Slip-system and ebsd analysis on compressively deformed fine-grained polycrystalline olivine, *Geological Society, London, Special Publications*, *360*(1), 225–235.

Farla, R. J., I. Jackson, J. D. F. Gerald, U. H. Faul, and M. E. Zimmerman (2012), Dislocation damping and anisotropic seismic wave attenuation in earth's upper mantle, *Science*, *336*(6079), 332–335.

Fei, H., C. Hegoda, D. Yamazaki, M. Wiedenbeck, H. Yurimoto, S. Shcheka, and T. Katsura (2012), High silicon self-diffusion coefficient in dry forsterite, *Earth and Planetary Science Letters*, *345*, 95–103.

Fei, H., M. Wiedenbeck, D. Yamazaki, and T. Katsura (2013), Small effect of water on upper-mantle rheology based on silicon self-diffusion coefficients, *Nature*, *498*(7453), 213–215.

Frost, H., and M. Ashby (1982), *Deformation Mechanism Maps*, Pergamon Press, New York.

Girard, J., J. Chen, P. Raterron, and C. W. Holyoke (2013), Hydrolytic weakening of olivine at mantle pressure: Evidence of [100](010) slip system softening from single-crystal deformation experiments, *Physics of the Earth and Planetary Interiors*, *216*, 12–20.

Goetze, C. (1978), The mechanisms of creep in olivine [and discussion], *Philosophical Transactions of the Royal Society of London. Series A, Mathematical and Physical Sciences*, *288*(1350), 99–119.

Goetze, C., and D. Kohlstedt (1973), Laboratory study of dislocation climb and diffusion in olivine, *Journal of Geophysical Research*, *78*(26), 5961–5971.

Goldsby, D., and D. Kohlstedt (2001), Superplastic deformation of ice: Experimental observations, *J. Geophys. Res.*, *106*, 11,017–11,030, doi:10.1029/2000JB900336.

Griggs, D. (1967), Hydrolytic weakening of quartz and other silicates, *Geophysical Journal International*, *14*(1-4), 19–31.

Griggs, D., and J. Blacic (1964), The strength of quartz in the ductile regime, *Trans. Am. Geophys. Union*, *45*, 102–103.

Hansen, L., M. Zimmerman, and D. Kohlstedt (2011), Grain boundary sliding in san carlos olivine: Flow law parameters and crystallographic-preferred orientation, *Journal of Geophysical Research*, *116*(B8), B08,201.

Hansen, L., M. Zimmerman, and D. Kohlstedt (2012), The influence of microstructure on deformation of olivine in the grain-boundary sliding regime, *Journal of Geophysical Research: Solid Earth (1978–2012)*, *117*(B9).

Hansen, L. N., Y.-H. Zhao, M. E. Zimmerman, and D. L. Kohlstedt (2014), Protracted fabric evolution in olivine: Implications for the relationship among strain, crystallographic fabric, and seismic anisotropy, *Earth and Planetary Science Letters*, *387*, 157–168.

Herring, C. (1950), Diffusional viscosity of a polycrystalline solid, *Journal of Applied Physics*, *21*(5), 437–445.

Hildyard, R. C., D. J. Prior, D. R. Faulkner, and E. Mariani (2009), Microstructural analysis of anhydrite rocks from the triassic evaporites, umbria-marche apennines, central italy: An insight into deformation mechanisms and possible slip systems, *Journal of Structural Geology*, *31*(1), 92–103.

Hirschmann, M. M. (2006), Water, melting, and the deep Earth H_2O cycle, *Annu. Rev. Earth Planet. Sci.*, *34*, 629–653.

Hirth, G., and D. Kohlstedt (1995), Experimental constraints on the dynamics of the partially molten upper mantle 2: Deformation in the dislocation creep regime, *J. Geophys. Res.*, *100*, 15,441–15,449, doi:10.1029/95JB01292.

Hirth, G., and D. Kohlstedt (2003), Rheology of the mantle wedge, in *Inside the Subduction Factory*, vol. 138, pp. 83–105.

Hirth, G., and D. Kohlstedt (2015), The stress dependence of olivine creep rate: Implications for extrapolation of lab data and interpretation of recrystallized grain size, *Earth and Planetary Science Letters*, *418*, 20–26.

Hirth, G., and D. L. Kohlstedt (1996), Water in the oceanic upper mantle: Implications for rheology, melt extraction and the evolution of the lithosphere, *144*(1-2), 93–108, doi: 10.1016/0012-821X(96)00154-9.

Hirth, J., and J. Lothe (1968), *Theory of Dislocations*, 780 pp., New York: McGraw-Hill.

Hobbs, B. (1983), Constraints on the mechanism of deformation of olivine imposed by defect chemistry, *Tectonophysics*, *92*(1), 35–69.

Ismail, W. B., and D. Mainprice (1998), An olivine fabric database: an overview of upper mantle fabrics and seismic anisotropy, *Tectonophysics*, *296*(1-2), 145–157, doi:10.1016/S0040-1951(98)00141-3.

Jackson, I., U. H. Faul, and R. Skelton (2014), Elastically accommodated grain-boundary sliding: New insights from experiment and modeling, *Physics of the Earth and Planetary Interiors*, *228*, 203–210.

Johanesen, K. E., and J. P. Platt (2015), Rheology, microstructure, and fabric in a large scale mantle shear zone, ronda peridotite, southern spain, *Journal of Structural Geology*, *73*, 1–17.

Kaminski, E., and N. Ribe (2001), A kinematic model for recrystallization and texture development in olivine polycrystals, *189*(3-4), 253–267, doi:10.1016/S0012-821X(01)00356-9.

Karato, S., M. Paterson, and J. Fitzgerald (1986), Rheology of synthetic olivine aggregates: Influence of grain size and water, *J. Geophys. Res.*, *91*, 8151–76, doi: doi:10.1029/JB091iB08p08151.

Katayama, I., and S.-i. Karato (2008), Low-temperature, high-stress deformation of olivine under water-saturated conditions, *Physics of the Earth and Planetary Interiors*, *168*(3), 125–133.

Keefner, J. W., S. J. Mackwell, D. L. Kohlstedt, and F. Heidelbach (2011), Dependence of dislocation creep of dunite on oxygen fugacity: Implications for viscosity variations in Earth's mantle, *J. Geophys. Res.*, *116*(B5), B05201, doi:10.1029/2010JB007748.

Knoll, M., A. Tommasi, R. Logé, and J. Signorelli (2009), A multiscale approach to model the anisotropic deformation of lithospheric plates, *Geochem. Geophys. Geosyst.*, *10*, Q08,009, doi:10.1029/2009GC002423.

Kocks, U. (1976), Laws for work-hardening and low-temperature creep, *Journal of engineering materials and technology*, *98*(1), 76–85.

Kohlstedt, D. (2006), The role of water in high-temperature rock deformation, *Reviews in mineralogy and geochemistry*, *62*(1), 377.

Kohlstedt, D. (2007), Constitutive equations, rheological behavior, and viscosity of rocks, *Treatise on Geophysics*, *2*, 389–417.

Kohlstedt, D., and L. Hansen (2015), Constitutive equations, rheological behavior, and viscosity of rocks, *Treatise on Geophysics*, *2*, 441–472.

Kohlstedt, D., and P. Hornack (1981), Effect of oxygen partial pressure on the creep of olivine, *Anelasticity in the Earth*, pp. 101–107.

Kohlstedt, D. L., and C. Goetze (1974), Low-stress high-temperature creep in olivine single crystals, *J. Geophys. Res.*, *79*, 2045–2051, doi:doi:10.1029/JB079i014p02045.

Langdon, T. (1994), Unified approach to grain boundary sliding in creep and superplasticity, *42*, 2437–2443, doi:10.1016/0956-7151(94)90322-0.

Lebensohn, R., and C. Tomé (1993), A self-consistent anisotropic approach for the simulation of plastic deformation and texture development of polycrystals: application to zirconium alloys, *Acta Metallurgica et Materialia*, *41*(9), 2611–2624.

Lee, K.-H., Z. Jiang, and S.-i. Karato (2002), A scanning electron microscope study of the effects of dynamic recrystallization on lattice preferred orientation in olivine, *Tectonophysics*, *351*(4), 331–341.

Lloyd, G. E., A. B. Farmer, and D. Mainprice (1997), Misorientation analysis and the formation and orientation of subgrain and grain boundaries, *Tectonophysics*, *279*(1-4), 55–78, doi:10.1016/S0040-1951(97)00115-7.

Long, H., D. J. Weidner, L. Li, J. Chen, and L. Wang (2011), Deformation of olivine at subduction zone conditions determined from in situ measurements with synchrotron radiation, *Physics of the Earth and Planetary Interiors*, *186*(1), 23–35.

Mackwell, S., D. Kohlstedt, and M. Paterson (1985), The role of water in the deformation of olivine single crystals, *Journal of Geophysical Research*, *90*(B13), 11,319–11.

Mainprice, D., A. Tommasi, H. Couvy, P. Cordier, and D. J. Frost (2005), Pressure sensitivity of olivine slip systems and seismic anisotropy of earth's upper mantle, *Nature*, *433*(7027), 731–733.

McDonnell, R., C. Peach, and C. Spiers (1999), Flow behavior of fine-grained synthetic dunite in the presence of 0.5 wt% H2O, *J. Geophys. Res.*, *104*, 17,823–17,845.

Mehl, L., and G. Hirth (2008), Plagioclase preferred orientation in layered mylonites: evaluation of flow laws for the lower crust, *J. Geophys. Res.*, *113*(B5), B05202, doi: 10.1029/2007JB005075.

Mei, S., and D. L. Kohlstedt (2000a), Influence of water on plastic deformation of olivine aggregates 1. Diffusion creep regime, *J. Geophys. Res.*, *105*, 21,457–21,469.

Mei, S., and D. L. Kohlstedt (2000b), Influence of water on plastic deformation of olivine aggregates 2. Dislocation creep regime, *J. Geophys. Res.*, *105*, 21,471–21,481.

Mei, S., A. Suzuki, D. Kohlstedt, N. Dixon, and W. Durham (2010), Experimental constraints on the strength of the lithospheric mantle, *J. Geophys. Res*, *115*, B08204, doi: 10.1029/2009JB006873.

Miyazaki, T., K. Sueyoshi, and T. Hiraga (2013), Olivine crystals align during diffusion creep of earth's upper mantle, *Nature*, *502*(7471), 321–326.

Mott, N. (1951), The mechanical properties of metals, *Proceedings of the Physical Society. Section B*, *64*(9), 729.

Nabarro, F. (1948), Deformation of crystals by the motion of single ions, in *Report of a Conference on Strength of Solids*, pp. 75–90.

Nakamura, A., and H. Schmalzried (1983), On the nonstoichiometry and point defects of olivine, *Physics and Chemistry of Minerals*, *10*(1), 27–37.

Paterson, M. S. (1982), The determination of hydroxyl by infrared absorption in quartz, silicate glasses and similar materials, *Bull. Minéral.*, *105*(1), 20–29.

Paterson, M. S. (1990), Rock deformation experimentation, in *The Brittle Ductile Transition in Rocks, The Heard Volume*, vol. 56, pp. 187–194.

Phakey, P., G. Dollinger, and J. Christie (1972), Transmission electron microscopy of experimentally deformed olivine crystals, *Geophysical Monograph Series*, *16*, 117–138.

Platt, J., and W. Behr (2011), Grainsize evolution in ductile shear zones: Implications for strain localization and the strength of the lithosphere, *Journal of Structural Geology*, *33*(4), 537–550.

Poirier, J.-P. (1985), *Creep of crystals: High-temperature deformation processes in metals, ceramics and minerals*, Cambridge University Press, New York.

Pommier, A., K. Leinenweber, D. L. Kohlstedt, C. Qi, E. J. Garnero, S. J. Mackwell, and J. A. Tyburczy (2015), Experimental constraints on the electrical anisotropy of the lithosphere-asthenosphere system, *Nature*, *522*(7555), 202–206.

Poumellec, B., and O. Jaoul (1984), Influence of po2 and ph2o on the high temperature plasticity of olivine, in *Deformation of Ceramic Materials II*, pp. 281–305, Springer.

Précigout, J., and G. Hirth (2014), B-type olivine fabric induced by grain boundary sliding, *Earth and Planetary Science Letters*, *395*, 231–240.

Prior, D. J., J. Wheeler, L. Peruzzo, R. Spiess, and C. Storey (2002), Some garnet microstructures: an illustration of the potential of orientation maps and misorientation analysis in microstructural studies, *24*(6-7), 999–1011, doi:10.1016/S0191-8141(01)00087-6.

Raterron, P., Y. Wu, D. Weidner, and J. Chen (2004), Low-temperature olivine rheology at high pressure, *Phys. Earth Planet. In.*, *145*(1), 149–159, doi:10.1016/j.pepi.2004.03.007.

Raterron, P., J. Chen, L. Li, D. Weidner, and P. Cordier (2007), Pressure-induced slip-system transition in forsterite; single-crystal rheological properties at mantle pressure and temperature, *American Mineralogist*, *92*(8-9), 1436–1445.

Raterron, P., E. Amiguet, J. Chen, L. Li, and P. Cordier (2009), Experimental deformation of olivine single crystals at mantle pressures and temperatures, *Phys. Earth Planet. In.*, *172*(1-2), 74–83, doi:10.1016/j.pepi.2008.07.026.

Ricoult, D., and D. Kohlstedt (1985a), Experimental evidence for the effect of chemical environment upon the creep rate of olivine, *Point defects in minerals*, pp. 171–184.

Ricoult, D. L., and D. L. Kohlstedt (1985b), Creep of Fe_2SiO_4 and Co_2SiO_4 single crystals in controlled thermodynamic environments, *51*(1), 79–93, doi:10.1080/01418618508245271.

Sachs, G. (1928), Zur ableitung einer fliessbedingung, *Z. Ver. Dtsch. Ing.*, *72*, 734–736.

Schmid, S., J. Boland, and M. Paterson (1977), Superplastic flow in finegrained limestone, *Tectonophysics*, *43*(3-4), 257–291, doi:10.1016/0040-1951(77)90120-2.

Schneider, S. E. (2008), Deformation of olivine single crystals at intermediate temperatures: Application to deformation of the lithosphere, *M.S. Thesis, University of Minnesota*, p. 99.

Spingarn, J., D. Barnett, and W. Nix (1979), Theoretical descriptions of climb controlled steady state creep at high and intermediate temperatures, *Acta Metallurgica*, *27*(9), 1549–1561.

Sundberg, M., and R. F. Cooper (2008), Crystallographic preferred orientation produced by diffusional creep of harzburgite: Effects of chemical interactions among phases during plastic flow, *J. Geophys. Res.*, *113*(B12), B12208, doi:10.1029/2008JB005618.

Tielke, J., M. Zimmerman, and D. Kohlstedt (in prep), Hydrolytic weakening in olivine single crystals deforming by dislocation creep at lithospheric mantle temperatures, *Journal Geophysical Research*, *ii*(ii), ii.

Tommasi, A., D. Mainprice, G. Canova, and Y. Chastel (2000), Viscoplastic self-consistent and equilibrium-based modeling of olivine lattice preferred orientations: Implications for the upper mantle seismic anisotropy, *J. Geophys. Res.*, *105*, 7893–7908, doi:10.1029/1999JB900411.

Tommasi, A., M. Knoll, A. Vauchez, J. W. Signorelli, C. Thoraval, and R. Logé (2009), Structural reactivation in plate tectonics controlled by olivine crystal anisotropy, *Nat. Geosci.*, *2*(6), 423–427, doi:10.1038/ngeo528.

Toy, V. G., J. Newman, W. Lamb, and B. Tikoff (2010), The role of pyroxenites in formation of shear instabilities in the mantle: Evidence from an ultramafic ultramylonite, Twin Sisters Massif, Washington, *51*(1-2), 55, doi:10.1093/petrology/egp059.

Underwood, E. (1970), *Quantitative stereology*, Addison-Wesley, Reading, Massachusetts.

Walker, A., E. Rutter, and K. Brodie (1990), Experimental study of grain-size sensitive flow of synthetic, hot-pressed calcite rocks, *54*(1), 259, doi:10.1144/GSL.SP.1990.054.01.24.

Wang, Z., Y. Zhao, and D. L. Kohlstedt (2010), Dislocation creep accommodated by grain boundary sliding in dunite, *J. Earth Sci.*, *21*(5), 541–554, doi:10.1007/s12583-010-0113-1.

Warren, J. M., and G. Hirth (2006), Grain size sensitive deformation mechanisms in naturally deformed peridotites, *248*(1-2), 438–450, doi:10.1016/j.epsl.2006.06.006.

Weertman, J. (1955), Theory of steady-state creep based on dislocation climb, *Journal of Applied Physics*, *26*(10), 1213–1217.

Weertman, J. (1999), Microstructural mechanisms of creep, *Mechanics and materials: Fundamentals and linkages*, pp. 451–488.

Wheeler, J. (2009), The preservation of seismic anisotropy in the earth's mantle during diffusion creep, *178*(3), 1723–1732, doi:10.1111/j.1365-246X.2009.04241.x.

Young, C. (1969), Dislocations in the deformation of olivine, *American Journal of Science*, *267*(7), 841–852.

Zhang, S., and S. Karato (1995), Lattice preferred orientation of olivine aggregates deformed in simple shear, *Nature*, *375*(6534), 774–777.

Zhang, S., S. Karato, J. Fitzgerald, U. H. Faul, and Y. Zhou (2000), Simple shear deformation of olivine aggregates, *Tectonophysics*, *316*(1-2), 133–152, doi:10.1016/S0040-1951(99)00229-2.

Appendix A

Micromechanical model

A.1 Script for calculating the strain rate of an aggregate

This appendix provides an example of the MATLAB® script used to calculate the strain rate of experimentally deformed olivine aggregates from single crystals flow laws in Chapter 4. The input are the experimentally measured stress and EBSD measurements of crystallographic orientations. The example provided here is for an aggregate with a near uniform distribution of crystallographic orientations that is deformed in a stress state equivalent to a compression experiment. In the first part of this script, the stress and grain orientations are defined. These values of stress and grain orientation are used to calculate the strain rates of individual grains in the matlab function described in the second section. The final part of the script describes the calculations needed to plot the strain rates of individual grains as a function of the Schmid factors for all of the slip systems in each grain (i.e. Figure 4.2).

```
% This matlab script is used to calcuate the strain rate of an olivine
 aggregate using the single crystal flow laws from Bai et al. (1991).
% The file 1543.txt contains a numerically generated dataset of 2,604
 grains with "random" orientaitons.
% The script also calculates the strain rate due to the individual slip
```

```
systems for each grain, and plots these data as a function of
Schmid Factor on each slip system.
% The guidance and assistance of Lars Hansen was essential to
creating this code.
%_____ Define experimental Conditoins ___________
T=1523.15;% define the temperature in K
input_stress=440; %define the differential stress, in MPa
%_____ Input Grain Orientations ___________
data = dlmread('pf535.txt','\t',1,0);% for uniform fabric
euler= data(:,1:3);
%preallocate  data for computational efficiency
strain_rate_tensors=zeros(3,3,length(data));
%strain_rate_tensors_x_d=zeros(3,3,length(data));
for i=1:length(data);
    strain_rate_tensors(:,:,i)=strain_rate_from_constant_stress_random
    _fabric_compression(input_stress,T,euler(i,:));
end
total_strain_rate=mean(strain_rate_tensors,3);%./sum(grain_volume)
axial_strain_rate=total_strain_rate(2,2)

%%%%% Calculate strain rate from glide on (010)[100] only
strain_rate_a_on_b=zeros(3,3,length(data));
for i=1:length(data);
    strain_rate_a_on_b(:,:,i)=strain_rate_from_a_on_b_compression
     (input_stress,T,euler(i,:));
%    strain_rate_tensors_x_d(:,:,i) = strain_rate_tensors(:,:,i) *
grain_volume(i);
end
axial_strain_rate_a_on_b=strain_rate_a_on_b(2,2);

%%%%% Calculate strain rate from glide on (001)[100] only
strain_rate_a_on_c=zeros(3,3,length(data));

for i=1:length(data);
```

```
    strain_rate_a_on_c(:,:,i)=strain_rate_from_a_on_c_
     compression(input_stress,T,euler(i,:));
%    strain_rate_tensors_x_d(:,:,i) = strain_rate_tensors(:,:,i)
* grain_volume(i);
end
axial_strain_rate_a_on_c=strain_rate_a_on_c(2,2);

%%%%% Calculate strain rate from glide on (010)[001] only
strain_rate_c_on_b=zeros(3,3,length(data));
for i=1:length(data);
    strain_rate_c_on_b(:,:,i)=strain_rate_from_c_on_b_
    compression(input_stress,T,euler(i,:));
%    strain_rate_tensors_x_d(:,:,i) = strain_rate_tensors(:,:,i)
* grain_volume(i);
end
axial_strain_rate_c_on_b=strain_rate_c_on_b(2,2);

%%%%% Calculated Schmid factors for plotting
%Axes to plot -- miller indices
axs = [1 0 0; 0 1 0; 0 0 1];
%loading direction in xyz coordinates
L = [0 1 0];%for compression
%L = [-1 1 0];%for torsion
%lattice parameters - units don't matter as long as
they're consistent -- (a,b,c)
a = [4.762 10.225 5.994]; %olivine from Birle et al. (1968)
%a = [4.785 10.34 6.035]; %approx Fo50 from Deer,
Howie, and Zussman (1992)
%slip plane for (010)[100]- refers to the order of axes listed in axs
plane = [2];
%slip direction
direction = [1];
phi1 = data(:,1); PHI = data(:,2); phi2 = data(:,3);
axs_title = axs;
```

```
%scale axes by lattice parameters
for s = 1:size(axs,1)
    axs(s,:) = axs(s,:).*a;
end
%normalize starting vectors
for s = 1:size(axs,1)
    nrm(s,:) = ones(size(axs,2),1)*norm(axs(s,:));
en
axs = axs./nrm;
for i = 1:length(phi1);
R1 = [cosd(phi1(i)) -sind(phi1(i)) 0
      sind(phi1(i))  cosd(phi1(i)) 0
      0              0             1]; %rotation around z axis by phi1
R2 = [1 0             0
      0 cosd(PHI(i)) -sind(PHI(i))
      0 sind(PHI(i))  cosd(PHI(i))]; %rotation around x by PHI
R3  = [cosd(phi2(i)) -sind(phi2(i)) 0
      sind(phi2(i))  cosd(phi2(i)) 0
      0              0             1]; %rotation around z axis by phi2
R = R1*R2*R3;
for s = 1:size(axs,1)
   xyz_point(:,s) = R*axs(s,:)';
end
xyz(:,:,i) = xyz_point;
end
for j = 1:length(plane)
for i = 1:length(phi1)

L = L./norm(L);
P = xyz(plane(j),:,i);
P = P./norm(P);
D = xyz(direction(j),:,i);
D = D./norm(D);
S(i,j) = abs(dot(L,P)*dot(L,D));
```

```
end
end

%slip plane for (010)[001]- refers to the order of axes listed in axs
plane_b = [2];
%slip direction
direction_b = [3];
phi1 = data(:,1); PHI = data(:,2); phi2 = data(:,3);
axs_title = axs;
%scale axes by lattice parameters
for s = 1:size(axs,1)
    axs(s,:) = axs(s,:).*a;
end
%normalize starting vectors
for s = 1:size(axs,1)
    nrm(s,:) = ones(size(axs,2),1)*norm(axs(s,:));
end
axs = axs./nrm;
for i = 1:length(phi1);
R1 = [cosd(phi1(i)) -sind(phi1(i)) 0
      sind(phi1(i))  cosd(phi1(i)) 0
      0              0             1]; %rotation around z axis by phi1
R2 = [1 0             0
      0 cosd(PHI(i)) -sind(PHI(i))
      0 sind(PHI(i))  cosd(PHI(i))]; %rotation around x by PHI

R3  = [cosd(phi2(i)) -sind(phi2(i)) 0
      sind(phi2(i))  cosd(phi2(i)) 0
      0              0             1]; %rotation around z axis by phi2
R = R1*R2*R3;
for s = 1:size(axs,1)
   xyz_point(:,s) = R*axs(s,:)';
end
xyz(:,:,i) = xyz_point;
```

```
end
for j = 1:length(plane_b)
for i = 1:length(phi1)
L = L./norm(L);
P_b = xyz(plane_b(j),:,i);
P_b = P_b./norm(P_b);
D_b = xyz(direction_b(j),:,i);
D_b = D_b./norm(D_b);
S_b(i,j) = abs(dot(L,P_b)*dot(L,D_b));
end
end

%slip plane for (001)[100]- refers to the order of axes listed in axs
plane_e = [3];
%slip direction
direction_e = [1];
phi1 = data(:,1); PHI = data(:,2); phi2 = data(:,3);
axs_title = axs;
%scale axes by lattice parameters
for s = 1:size(axs,1)
    axs(s,:) = axs(s,:).*a;
end
%normalize starting vectors
for s = 1:size(axs,1)
    nrm(s,:) = ones(size(axs,2),1)*norm(axs(s,:));
end
axs = axs./nrm;
for i = 1:length(phi1);
R1 = [cosd(phi1(i)) -sind(phi1(i)) 0
      sind(phi1(i))  cosd(phi1(i)) 0
      0              0             1]; %rotation around z axis by phi1
R2 = [1 0             0
      0 cosd(PHI(i)) -sind(PHI(i))
      0 sind(PHI(i))  cosd(PHI(i))]; %rotation around x by PHI
```

```
R3  = [cosd(phi2(i)) -sind(phi2(i)) 0
      sind(phi2(i))  cosd(phi2(i)) 0
      0              0             1]; %rotation around z axis by phi2
R = R1*R2*R3;
for s = 1:size(axs,1)
   xyz_point(:,s) = R*axs(s,:)';
end
xyz(:,:,i) = xyz_point;
end
for j = 1:length(plane_e)
for i = 1:length(phi1)
L = L./norm(L);
P_e = xyz(plane_e(j),:,i);
P_e = P_e./norm(P_e);
D_e = xyz(direction_e(j),:,i);
D_e = D_e./norm(D_e);
S_e(i,j) = abs(dot(L,P_e)*dot(L,D_e));
end
end

%plot eq. strain rate for each grain as a funciton of grain size
%calculate strain rate
for k = 1: size(euler,1)
    r_eq_temp = 0;
    for j = 1:3
        for i = 1:3
            temp = strain_rate_tensors(i,j,k)*strain_rate_tensors(j,i,k);
            r_eq_temp = r_eq_temp + temp;
        end
    end
    r_eq_grain(k,1) = sqrt(2/3 * r_eq_temp); %equivalent
     strain rate in each grain
    shear_grain(k,1) = strain_rate_tensors(1,2,k); %shear strain
    rate in each grain
```

```
end

y_22p=strain_rate_tensors(2,2,:);%plot axial strain rate for
each grain as a funciton of grain size
y_22=squeeze(y_22p);
y_12p=strain_rate_tensors(1,2,:);%plot shear strain rate for
each grain as a funciton of grain size
y_12=squeeze((abs(y_12p)));
y_13p=strain_rate_tensors(1,3,:);
y_31p=strain_rate_tensors(3,1,:);
y_21p=strain_rate_tensors(2,1,:);
y_23p=strain_rate_tensors(2,3,:);
y_32p=strain_rate_tensors(3,2,:);
y_11p=strain_rate_tensors(1,1,:);
y_33p=strain_rate_tensors(3,2,:);
y_13=squeeze((abs(y_13p)));
y_31=squeeze((abs(y_31p)));
y_21=squeeze((abs(y_21p)));
y_23=squeeze((abs(y_23p)));
y_32=squeeze((abs(y_32p)));
y_11=squeeze(y_11p);
y_33=squeeze(y_33p);
y_shear_tot=y_12+y_13+y_32;
y_eff=((2./9).*((y_22-y_11).^(2)+(y_11-y_33).^(2)+(y_33-y_22).^(2)))
.^(1./2);

%Component of axial strain rate in sample coordinates due to glide on each
%slip system
y_22p_a_on_b=strain_rate_a_on_b(2,2,:);
y_22_a_on_b=squeeze(y_22p_a_on_b);
y_22p_a_on_c=strain_rate_a_on_c(2,2,:);
y_22_a_on_c=squeeze(y_22p_a_on_c);
y_22p_c_on_b=strain_rate_c_on_b(2,2,:);
y_22_c_on_b=squeeze(y_22p_c_on_b);
```

```
RSS=input_stress.*S;
%%%_____________________________________-
%%%FIT A LINE TO AXIAL STRAIN RATE FROM A ON B
%
x_fit=[0:0.01:max(RSS)];
y_fit=(2.014.*10.^(-14).*x_fit.^(4.5));

%calculate strain rate
for k = 1: size(euler,1)
    r_eq_temp = 0;
    for j = 1:3
        for i = 1:3
            temp = strain_rate_tensors(i,j,k)*strain_rate_tensors(j,i,k);
            r_eq_temp = r_eq_temp + temp;
        end
    end
    r_eq_grain(k,1) = sqrt(2/3 * r_eq_temp); %equivalent
     strain rate in each grain
    shear_grain(k,1) = strain_rate_tensors(1,2,k); %shear
     strain rate in each grain
end
```

A.2 Calculation of strain rate

In this section, a matlab function is described that is used to calculate the strain rate from the motion of dislocations using single crystals flow laws. The matlab code contains definitions of the appropriate stress tensor and conditions of oxygen fugacity needed for the calculation.

```
%mean value of equivallent strain rate for entire sample
r_eq_sample=mean(r_eq_grain)
function [epsilon_sample_ref,tau1,epsilon_climb_sample_ref] =
strain_rate_from_constant_stress_random_fabric_compression
(input_stress,T,euler)
```

```
R_constant=8.314;
P=300;
n=3.5;
%f = 10.^-11.5; %~Fe/FeO @ 1200C
%for Ni/NiO
f = 10.^(12.78 - 2.5073.*(10^4./T) - 1.1.*log10(T) + 0.450.*P./T +
0.025.*P./1000);% in atm

Vm=43.8.*10.^(-6);
G=78500;
adry=4.75.*10.^(-10);  %a axis
bdry=10.20.*10.^(-10); %b axis
cdry=5.99.*10.^(-10);  %c axis

% %input stress tensor for compression
 sigma=[P 0 0;
         0 input_stress+P 0;
         0 0 P];

%Normal way to call up Euler angles
phi1 = euler(1); PHI = euler(2); phi2 = euler(3);

% Build rotation matrix for a grain
R1 = [cosd(phi1) -sind(phi1) 0
      sind(phi1)  cosd(phi1) 0
      0              0             1]; %rotation around z axis by phi1

R2 = [1 0             0
      0 cosd(PHI) -sind(PHI)
      0 sind(PHI)  cosd(PHI)]; %rotation around x by PHI

R3  = [cosd(phi2) -sind(phi2) 0
      sind(phi2)  cosd(phi2) 0
```

```
      0              0              1]; %rotation around z axis by phi2

R = R1*R2*R3;

sigma_crystal=R*sigma*R';
%deviatoric stress tensor
sigma_m=trace(sigma)./3; %mean stress

S=sigma_crystal;
S(1,1)=S(1,1)-sigma_m;
S(2,2)=S(2,2)-sigma_m;
S(3,3)=S(3,3)-sigma_m;

%Define burgers vectors (b) and slip plane normal (n) for slip systems
%For (010)[100]
b1=[1 0 0]';
n1=[0 1 0]';

%For (001)[100]
b2=[1 0 0]';
n2=[0 0 1]';

%For (010)[001]
b3=[0 0 1]';
n3=[0 1 0]';

%Symetric schmid tensor for glide
%010)[100]
mu1=(1./2)*(b1*n1'+n1*b1');
mu2=(1./2)*(b2*n2'+n2*b2');
mu3=(1./2)*(b3*n3'+n3*b3');
%Antisyemtric schmid tensor for glide
mu1a=(1./2)*(b1*n1'-n1*b1');
mu2a=(1./2)*(b2*n2'-n2*b2');
```

```
mu3a=(1./2)*(b3*n3'-n3*b3');
%Shear stresses
tau1=trace(mu1*S);
tau2=trace(mu2*S);
tau3=trace(mu3*S);
%differential stress
ds1=abs(2*tau1);%(010)[100]
ds2=abs(2*tau2);%(100)[001] or (001)[100]
ds3=abs(2*tau3);%(010)[001]

%Bai Flow laws for OPX buffered experiments
Aa1 = 0.02;
Aa2 = 1.3.*10.^(22);
Aa3 = 1.2;
ra1=.36;
ra2=.1;
ra3=.15;
qa1=230*1000;
qa2=1000*1000;
qa3=290*1000;
ea1 = Aa1.*ds1.^n.*f.^ra1.*exp(-qa1./R_constant./T);
ea2 = Aa2.*ds1.^n.*f.^ra2.*exp(-qa2./R_constant./T);
ea3 = Aa3.*ds1.^n.*f.^ra3.*exp(-qa3./R_constant./T);
epsilon_axial_1 = (ea1+(1./ea2 + 1./ea3).^-1)*sign(tau1);
gamma1=2*epsilon_axial_1;

%Bai FLow Law for 101c opx buffered
Ae1 = 0.65;
Ae2 = 5.3.*10.^(11);
re1=0.33;
re2=0.06;
qe1=250*1000;
qe2=690*1000;
ee1 = Ae1.*ds2.^n.*f.^re1.*exp(-qe1./R_constant./T);
```

```
ee2 = Ae2.*ds2.^n.*f.^re2.*exp(-qe2./R_constant./T);
epsilon_axial_2 = ((1./ee1)+(1./ee2)).^(-1)*sign(tau2);
gamma2=2*epsilon_axial_2;

%Bai FLow Law for 011c opx buffered
Ab1 = 2.1.*10.^4;
Ab2 = 5.2.*10.^(5);
rb1=0.02;
rb2=0.23;
qb1=540*1000;
qb2=540*1000;
eb1 = Ab1.*ds3.^n.*f.^rb1.*exp(-qb1./R_constant./T);
eb2 = Ab2.*ds3.^n.*f.^rb2.*exp(-qb2./R_constant./T);
epsilon_axial_3 = (eb1+eb2)*sign(tau3);
gamma3=2*epsilon_axial_3;

%strain rate for glide of three slip sytems
epsilon_glide=mu1*gamma1+mu2*gamma2+mu3*gamma3;

%Adding climb component
%symmetric portion of climb tensor assuming only edge dislocations
C1=(1./2)*(b1*b1'+b1*b1');
C2=(1./2)*(b2*b2'+b2*b2');
C3=(1./2)*(b3*b3'+b3*b3');
C1m=1./3*trace(C1);
C2m=1./3*trace(C2);
C3m=1./3*trace(C3);
C1_dev=C1;
C1_dev(1,1)=C1_dev(1,1)-C1m;
C1_dev(2,2)=C1_dev(2,2)-C1m;
C1_dev(3,3)=C1_dev(3,3)-C1m;
C2_dev=C2;
C2_dev(1,1)=C2_dev(1,1)-C2m;
C2_dev(2,2)=C2_dev(2,2)-C2m;
```

```
C2_dev(3,3)=C2_dev(3,3)-C2m;
C3_dev=C3;
C3_dev(1,1)=C3_dev(1,1)-C3m;
C3_dev(2,2)=C3_dev(2,2)-C3m;
C3_dev(3,3)=C3_dev(3,3)-C3m;

%stress for climb
sigma_climb_1=trace(C1_dev*S);
sigma_climb_2=trace(C2_dev*S);
sigma_climb_3=trace(C3_dev*S);
%dry silicon diffusion equation from dohmen 2002
Dodry=10.^(-4.2);
Edry=530000;
Ddry=Dodry.*exp(-Edry./(R_constant.*T));
% calcuations from Fei et al 2012 @ 1000C
Dofei=10.^(-6.6);
Efei=410000;
Vfei=1.7;
P=0.3; %P in GPa?
Dfei=Dofei.*exp(-(Efei+P.*Vfei)./(R_constant.*T));
Ddry=Dfei%.*10.^8.;

%calculation of strain rate for climb using Nabarro 1967
%modified by Nix et al. (1971)
%from Kohlstedt (2007) Eq. 47
climb_rate_a_axis_1250C_Dohmen=2.*(G.*Vm)./(R_constant.*T)
.*(sigma_climb_1)./G.^(3).*(Ddry./(adry.^2)).*(1./(log((4.*G)
./(pi.*abs(sigma_climb_1))))).*sign(sigma_climb_1);
climb_rate_b_axis_1250C_Dohmen=2.*(G.*Vm)./(R_constant.*T)
.*(sigma_climb_2)./G.^(3).*(Ddry./(bdry.^2)).*(1./(log((4.*G)
./(pi.*abs(sigma_climb_2))))).*sign(sigma_climb_2);
climb_rate_c_axis_1250C_Dohmen=2.*(G.*Vm)./(R_constant.*T)
.*(sigma_climb_3)./G.^(3).*(Ddry./(cdry.^2)).*(1./(log((4.*G)
./(pi.*abs(sigma_climb_3))))).*sign(sigma_climb_3);
```

```
epsilon_climb=C1_dev*climb_rate_a_axis_1250C_Dohmen+C2_dev*
climb_rate_b_axis_1250C_Dohmen+C3_dev*climb_rate_c_axis_1250C_Dohmen;
epsilon_grain_glide_plus_climb=epsilon_glide+epsilon_climb;
epsilon_sample_ref=R'*epsilon_grain_glide_plus_climb*R;
```

Appendix B

Sensitivity of parameters for exponential creep

The values of parameters A_{e}, Q_{e}, σ_{e} resulting from fixing p and q at different values from the low temperature data for the (001)[100] slip system are reported in Table B.1. In these analyses, the data were fit to the flow law described in Equation 2.2. The results illustrate that values of A_{e} and Q_{e} are largely insensitive to the different values of p and q whereas values of σ_{e} vary significantly for the different values of p and q. An exploration of the sensitivity of the shape of the exponential function is presented in Figure B.1. The degree of upward curvature in the exponential function can be increased by either (1) decreasing the value of σ_{e}, (2) decreasing the value of *p*, or (3) increasing the value of *q*.

Table B.1: Sensitivity of parameters to values of p and q

p	q	A_{e}	Q_{e} (kJ/mol)	σ_{e} (GPa)
0.5	1	$10^{5.2\pm1.0}$	476 ± 37	8.4 ± 1.0
0.5	1.5	$10^{5.2\pm1.0}$	480 ± 38	16.0 ± 2.0
0.5	2	$10^{5.1\pm1.0}$	483 ± 38	25.9 ± 3.4
0.66	1	$10^{5.4\pm1.0}$	452 ± 34	5.9 ± 0.5
0.66	1.5	$10^{5.3\pm1.0}$	454 ± 35	9.9 ± 1.0
0.66	2	$10^{5.3\pm1.0}$	455 ± 35	14.4 ± 1.5

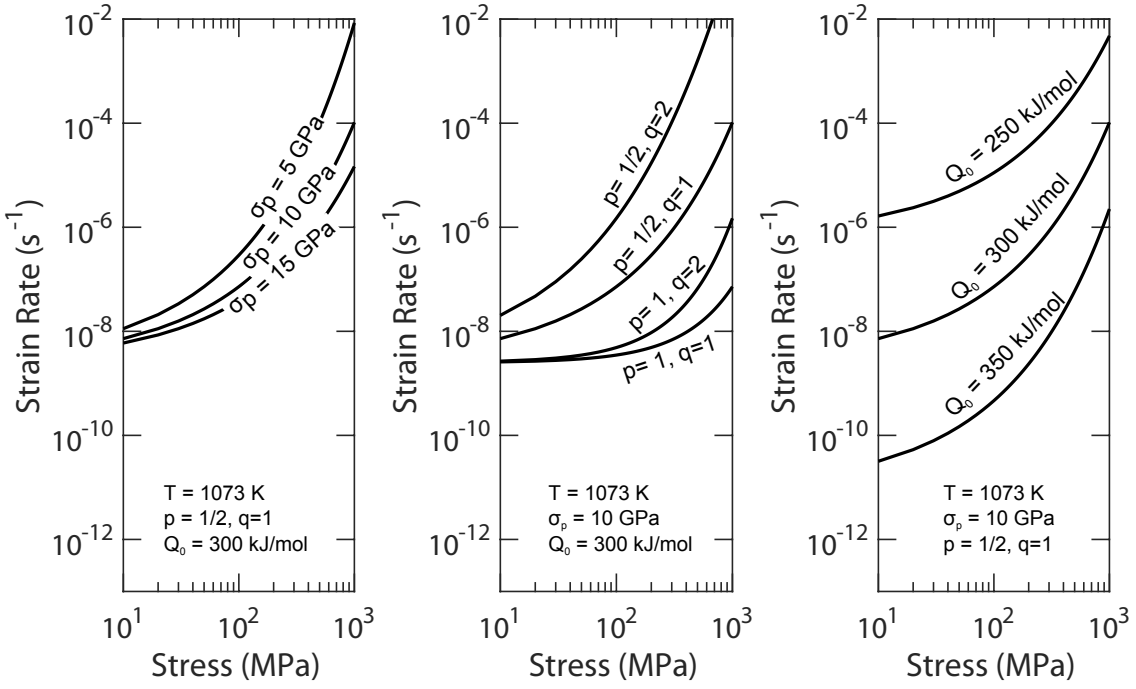

Figure B.1: Plots illustrating the influence of $\sigma_{\rm e}$ (left), p and q (middle), and Q (right) in Equation 2.2.

For comparison to the results from *Mei et al.* (2010), the data were fit using

$$\dot{\varepsilon}_{\rm exp} = A_{\rm e}\sigma^2 \exp\left[\left(\frac{-Q_{\rm e}}{{\rm R}T}\right)\left(1-\left(\frac{\sigma}{\sigma_{\rm p}}\right)^{0.5}\right)^1\right], \tag{B.1}$$

yielding $A_{\rm e} = 10^{3.5\pm1.0}$, $Q_{\rm e} = 359 \pm 37$ kJ/mol, and $\sigma_{\rm e} = 10.1 \pm 1.4$ GPa. For comparison to the results from *Demouchy et al.* (2013), the data were fit using

$$\dot{\varepsilon}_{\rm exp} = A_{\rm e} \exp\left[\left(\frac{-Q_{\rm e}}{{\rm R}T}\right)\left(1-\left(\frac{\sigma}{\sigma_{\rm p}}\right)^{0.5}\right)^2\right], \tag{B.2}$$

yielding $A_{\rm e} = 10^{9.1\pm1.0}$, $Q_{\rm e} = 526 \pm 37$ kJ/mol, and $\sigma_{\rm e} = 17.5 \pm 1.8$ GPa.